NAVAL POSTGRADUATE SCHOOL

MONTEREY, CALIFORNIA

THESIS

TYPHOON EFFECTS ON THE SOUTH CHINA SEA WAVE CHARACTERISTICS DURING WINTER MONSOON

by

CHENG, Kuo-Feng

March 2006

Thesis Advisor:	Peter C. Chu
Second Reader:	Timour Radko

Approved for public release; distribution is unlimited.

THIS PAGE INTENTIONALLY LEFT BLANK

REPORT DOCUMENTATION PAGE			*Form Approved OMB No. 0704-0188*
Public reporting burden for this collection of information is estimated to average 1 hour per response, including the time for reviewing instruction, searching existing data sources, gathering and maintaining the data needed, and completing and reviewing the collection of information. Send comments regarding this burden estimate or any other aspect of this collection of information, including suggestions for reducing this burden, to Washington headquarters Services, Directorate for Information Operations and Reports, 1215 Jefferson Davis Highway, Suite 1204, Arlington, VA 22202-4302, and to the Office of Management and Budget, Paperwork Reduction Project (0704-0188) Washington DC 20503.			
1. AGENCY USE ONLY *(Leave blank)*	**2. REPORT DATE** March 2006	**3. REPORT TYPE AND DATES COVERED** Master's Thesis	
4. TITLE AND SUBTITLE: Typhoon Effects on the South China Sea Wave Characteristics during Winter Monsoon			**5. FUNDING NUMBERS**
6. AUTHOR(S) Kuo-Feng Cheng			
7. PERFORMING ORGANIZATION NAME(S) AND ADDRESS(ES) Naval Postgraduate School Monterey, CA 93943-5000			**8. PERFORMING ORGANIZATION REPORT NUMBER**
9. SPONSORING /MONITORING AGENCY NAME(S) AND ADDRESS(ES) N/A			**10. SPONSORING/MONITORING AGENCY REPORT NUMBER**
11. SUPPLEMENTARY NOTES The views expressed in this thesis are those of the author and do not reflect the official policy or position of the Department of Defense or the U.S. Government.			
12a. DISTRIBUTION / AVAILABILITY STATEMENT Approved for public release; distribution is unlimited.			**12b. DISTRIBUTION CODE**

13. ABSTRACT (maximum 200 words)

Ocean wave characteristics in the western Atlantic Ocean (Hurricane Region) to tropical cyclones have been well identified, but not the regional seas in the western Pacific, e.g., the South China Sea (Typhoon Region). This is due to the lack of observational and modeling studies in the regional seas of the western Pacific. To fill this gap, Wavewatch-III (WW3) is used to study the response of the South China Sea (SCS) to Typhoon Muifa (2004). The major purposes are to find the similarity and dissimilarity of wave characteristics between the two regions, and to evaluate the WW3 capability to typhoon forcing. The WW3 model is integrated from the JONSWAP wave spectra with a tropical cyclone wind profile model, simulating Typhoon Muifa, from 16 to 25 November 2004. This study shows strong similarities in the responses between Hurricane and Typhoon Regions, including strong asymmetry in the significant wave height (H_s) along the typhoon translation track with the maximum H_s in the right-front quadrant of the typhoon center, and asymmetry in the directional wave spectra at different locations (frontward, backward, rightward, and leftward) around the typhoon center. The unique features of the SCS wave characteristics to Muifa are also discussed.

14. SUBJECT TERMS South China Sea, sea surface wave, numerical simulation, WAVEWATCH-III, Typhoon Muifa (2004), winter monsoon, Tropical Cyclone Wind Profile Model	**15. NUMBER OF PAGES** 115
	16. PRICE CODE

17. SECURITY CLASSIFICATION OF REPORT Unclassified	**18. SECURITY CLASSIFICATION OF THIS PAGE** Unclassified	**19. SECURITY CLASSIFICATION OF ABSTRACT** Unclassified	**20. LIMITATION OF ABSTRACT** UL

NSN 7540-01-280-5500

Standard Form 298 (Rev. 2-89)
Prescribed by ANSI Std. 239-18

THIS PAGE INTENTIONALLY LEFT BLANK

**TYPHOON EFFECTS ON THE SOUTH CHINA SEA WAVE
CHARACTERISTICS DURING WINTER MONSOON**

Kuo-Feng CHENG
Lieutenant, Taiwan Navy
B.S., National Cheng Kung University, 1999

Submitted in partial fulfillment of the
requirements for the degree of

MASTER OF SCIENCE IN PHYSICAL OCEANOGRAPHY

from the

**NAVAL POSTGRADUATE SCHOOL
March 2006**

Author: CHENG, Kuo-Feng

Approved by: Peter C. Chu
                    Thesis Advisor

                    Timour Radko
                    Second Reader

                    Mary L. Batteen
                    Chairperson, Department of Oceanography

                    Donald P. Brutzman
                    Chair, Undersea Warfare Academic Committee

THIS PAGE INTENTIONALLY LEFT BLANK

ABSTRACT

Ocean wave characteristics in the western Atlantic Ocean (Hurricane Region) to tropical cyclones have been well identified, but not the regional seas in the western Pacific such as the South China Sea (Typhoon Region). This is due to the lack of observational and modeling studies in the regional seas of the western Pacific. To fill this gap, Wavewatch-III (WW3) is used to study the response of the South China Sea (SCS) to Typhoon Muifa (2004). The major purposes are to find the similarity and dissimilarity of wave characteristics between the two regions, and to evaluate the WW3 capability to typhoon forcing. The WW3 model is integrated from the JONSWAP wave spectra with a tropical cyclone wind profile model, simulating Typhoon Muifa, from 0000UTC 16 November to 1200UTC 25 November 2004. Since TY Muifa entered the SCS as late as 19 November, the model computation of the first three days, from 16 November to 18 November, could be considered as the 'spin up' period of WW3 model. This study shows strong similarities in the responses between Hurricane and Typhoon Regions, including strong asymmetry in the significant wave height (H_s) along the typhoon translation track with the maximum H_s in the right-front quadrant of the typhoon center, and asymmetry in the directional wave spectra at different locations (frontward, backward, rightward, and leftward) around the typhoon center. The unique features of the SCS wave characteristics to Muifa are also discussed.

THIS PAGE INTENTIONALLY LEFT BLANK

TABLE OF CONTENTS

LIST OF FIGURES

THIS PAGE INTENTIONALLY LEFT BLANK

LIST OF TABLES

THIS PAGE INTENTIONALLY LEFT BLANK

ACKNOWLEDGMENTS

THIS PAGE INTENTIONALLY LEFT BLANK

I.   INTRODUCTION

A moving tropical cyclone is an intense source of surface wind stress that causes many significant changes in ocean wave characteristics such as significant wave height, directional wave spectra, and wave propagation. These features have been well identified in open oceans and the western Atlantic/eastern Pacific regional seas, that is, the Hurricane Region (hereafter referred to HR). The tropical cyclone forced complex wave field is very important to the wind-wave interaction. A hurricane with intense and fast-varying winds produces a severe and complex ocean wave field that can propagate for thousands of kilometers away from the storm center, resulting in dramatic variation of the wave field in space and time (Barber and Ursell 1948). To investigate the wave characteristics, the directional spectra of hurricane generated waves were measured using various instruments. For example, the fetch effect was detected in the Celtic Sea using the high-frequency radar. The wave characteristics were obtained for the northeastern Pacific during passage of storm using the synthetic aperture radar image from ERS-1 satellite (Holt et al. 1998). The spatial wave variation of hurricane directional wave spectra was identified for both open ocean and landfall cases using the US National Aeronautics and Space Administration (NASA) scanning radar altimeter (Wright et al. 2001; Walsh et al. 2002).

The ocean wave response identified in HR is a significant right-forward-quadrant bias in the significant wave height. During the passage of Hurricane Bonnie (1998) in the Atlantic Ocean, both observational (Wright et al. 2001) and modeling (Moon et al. 2003) studies show that the significant wave height reaches 14 m in the open ocean. The maximum wave heights appear in the right forward quadrant of the hurricane center and propagate in the same direction as the hurricane. Moon et al. (2003) simulated the wave characteristics successfully using the wave model WAVEWATCH-III (hereafter referred to WW3) and found that the hurricane-generated wave field is mostly determined by two factors: the distance from the hurricane center or radius of maximum wind and hurricane translation speed. For the case of a hurricane with low translation speed, the dominant wave direction is mainly determined by the distance from the hurricane center.

Most of the observational and modeling studies on ocean waves generated by tropical cyclones are concentrated in HR. Few observational and/or modeling studies have been done in the Typhoon Region (hereafter referred to TR), especially in the South China Sea (SCS). The SCS is one of the largest marginal seas of the Western Pacific Ocean, extending across both tropical and subtropical zones and encompasses a total surface area of $3.5 \times 10^6 \, km^2$ (Figure 1). Also due to its semi-enclosed nature, the SCS is subject to high spatial and temporal variability from external forcing factors. One significant source of the SCS variability is the tropical cyclones that routinely affect the region. The WW3 has been implemented and verified for the SCS using the TOPEX/Poseidon (T/P) satellite data (Chu et al. 2004). However, there is no modeling study on SCS waves to typhoon winds. Our goal in this research is to identify if those effects occurring in HR still exist in TR. More specifically, we study the SCS responses to Typhoon Muifa (2004) using WW3, which was forced by a high-resolution wind field computed by a Tropical Cyclone Wind Profile Model (TCWPM) proposed by Carr and Elsberry (1997).

The outline of this thesis is as follows. The geography and climatology of the SCS are described in Chapter II. The descriptions of the SCS tropical cyclones and Typhoon Muifa (2004) are in Chapter III. Chapter IV discusses the processing of high resolution typhoon winds. The model features of WW3 and its implementation are described in Chapter V. This study also reviews several important recent researches in Chapter VI. The numerical simulation and the wave characteristic of the SCS are analyzed and discussed in Chapter VII. The conclusion and some suggestions are provided in Chapter VIII.
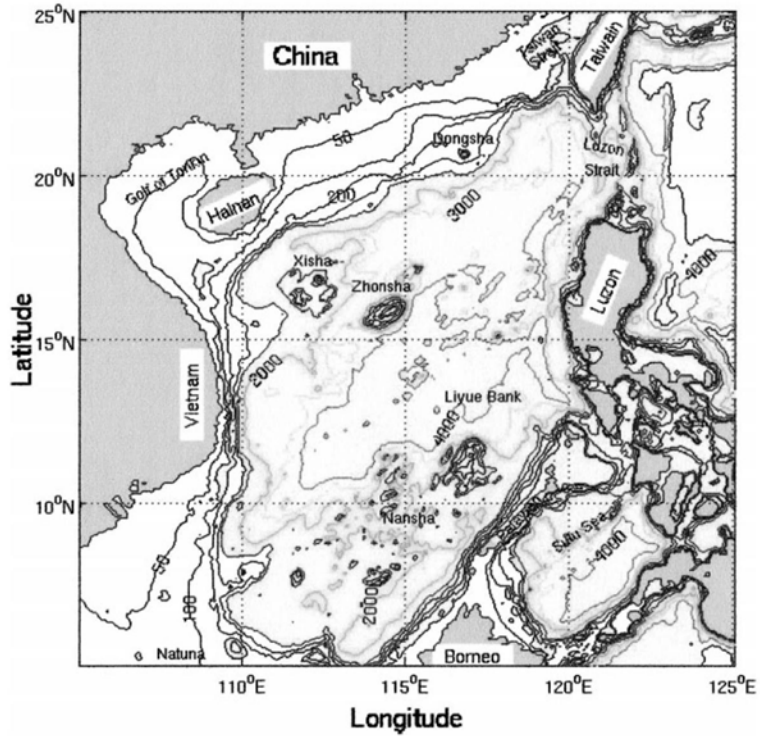
Figure 1   Geography of the South China Sea (from Chu et al. 2004).

THIS PAGE INTENTIONALLY LEFT BLANK

II. SOUTH CHINA SEA

The SCS is one of the most important marginal seas of the Western North Pacific Ocean. It is subjected to seasonal monsoon forcing with the northeasterly in the winter and the southwesterly in the summer. Tropical cyclones also invade the SCS in any month of a year.

A. GEOGRAPHY

The SCS is located among the Asian landmass to the west and to the north, Taiwan to the north-east, the Philippine Islands to the east, and Borneo to the south (Figure 1). The SCS region extends from the equator to $23°N$ and from $99°E$ to $121°E$ and the total surface area is about $3.5×10^6 km^2$. The SCS connects to the East China Sea through the Taiwan Strait, to the Pacific Ocean through the Luzon Strait, to the Sulu Sea through the Balabac Strait, to the Java Sea through the Karimata Strait, and to the Indian Ocean through the Strait of Malacca. All of these straits are shallow and narrow except the Luzon Strait with the maximum depth about 1800 m.

The SCS is a semi-enclosed tropical sea with a large abyssal basin, of which the maximum depth reaching as far as 5000 m at the geographic center (Su 1998). The ellipse-shaped basin is about 1900 km along its major axis (northeast–southwest) and approximately 1100 km along its minor axis. Wide continental shelves appear in the northwest and southwest of the basin and steep slopes in the central portion. Many reef islands and underwater plateaus are scattered throughout the SCS. From the Taiwan Strait to the Gulf of Tonkin, the continental shelves are about 70 m deep and 150 km wide. In the south end, the Sundra Shelf is the submerged connection between the Southeast Asia, Malaysia, Sumatra, Java, and Borneo, and is 100 m in depth around its center (Li 1994).

B. CLIMATOLOGY

In the winter season, winds are generally out of the northeast and relatively strong, while in the summer season, the winds completely reverse and become southwesterly and weak. Furthermore, synoptic systems often pass by the SCS and cause temporally and spatially varying wind field. Tropical cyclones can pass through and even generate within the SCS in any month of the year.

1. Monsoon Winds

The seasonal movement of the equatorial pressure trough, also known as the intertropical convergence zone (ITCZ), produces seasonal wind flow over the SCS (Gray 1968). A classic definition of the monsoon can be referred to Ramage (1971). The monsoon area is an encompassing region with January or July surface circulation, in which the prevailing wind direction shifts by at least $120°$ between January and July, the average frequency of prevailing wind directions in January and July exceeds 40 %, and the mean resultant winds in at least on of the months exceed 3 m/s.

The SCS satisfies all above features and experiences both winter and summer monsoons every year. The winter monsoon is known as the 'northeast monsoon' and the summer monsoon as the 'southwest monsoon'. These names are derived from the low-level prevailing winds of the two seasons (Figure 2). The winter monsoon onsets in around November and retreats in late March while the summer monsoon onsets in late May and retreats in late September. Between them are the brief transitional periods (Cheang 1987).

2. Summer Monsoon

In July and August, temperatures from the Asian landmass to the north of the SCS reach the annual maximums and produce a lower pressure over the continental region. In contrast, cooler air over the SCS and the southward oceanic region produces a higher pressure. An equatorial trough over the central Philippines extends northwestward to the low pressure over the Tibetan Plateau. The pressure gradient between the warm continental regions (north) and the cooler oceanic regions (south) causes air to flow northwestward south of the equator. The air flow then turns to flow northeastward as it crosses the equator and becomes the summer monsoon. The pressure gradient during the summer monsoon season is relatively weak, and produces southwest monsoon winds (about 3 m/s) over the SCS (Ramage 1971).

3. Winter Monsoon

The summer southwest monsoon begins to retreat in September, as the Asian landmass begins to cool down and a high pressure starts to build over this region. Air temperatures over the oceanic region remain warm and the pressure gradient begins to reverse. In October, the equatorial trough begins to move rapidly southward. By the

6

mid-October, the trough is along a line from the center of the Bay of Bengal to the north coast of New Guinea. North of the trough, northerly winds prevail as a high pressure centered over the central Asian landmass and continue to build, while in the south side of the trough, the southeast monsoon still dominates (Ramage 1971).

The winter northeast monsoon begins to set up in November when the equatorial trough moves south of the equator. The monsoon intensifies over the SCS, and monthly mean wind speed increases to 7 m/s. By December, the equatorial trough is located north of Australia ($5°S$). The high pressure is firmly established over the Asian landmass and intensifies the pressure gradient between the continental and the oceanic regions. The northeast monsoon reaches its strongest intensity over the SCS (8 to 10 m/s). The flow over the SCS is northerly to northeasterly winds north of the equator. South of the equator, the reversal in the sign of the Coriolis force causes the flow to turn eastward and becomes northwesterly to westerly (Ramage 1971).

The northeast monsoon continues over the region until April when the temperatures over the Asian continent start to increase, and when the equatorial trough begins to move to the north. Winds in the northern SCS remain northeasterly, but are weakened. In May, the northeast monsoon completely disappears, as the Asian continent continues to warm and the pressure gradient between the continental and oceanic regions reverses (Ramage 1971).

(a)

(b)
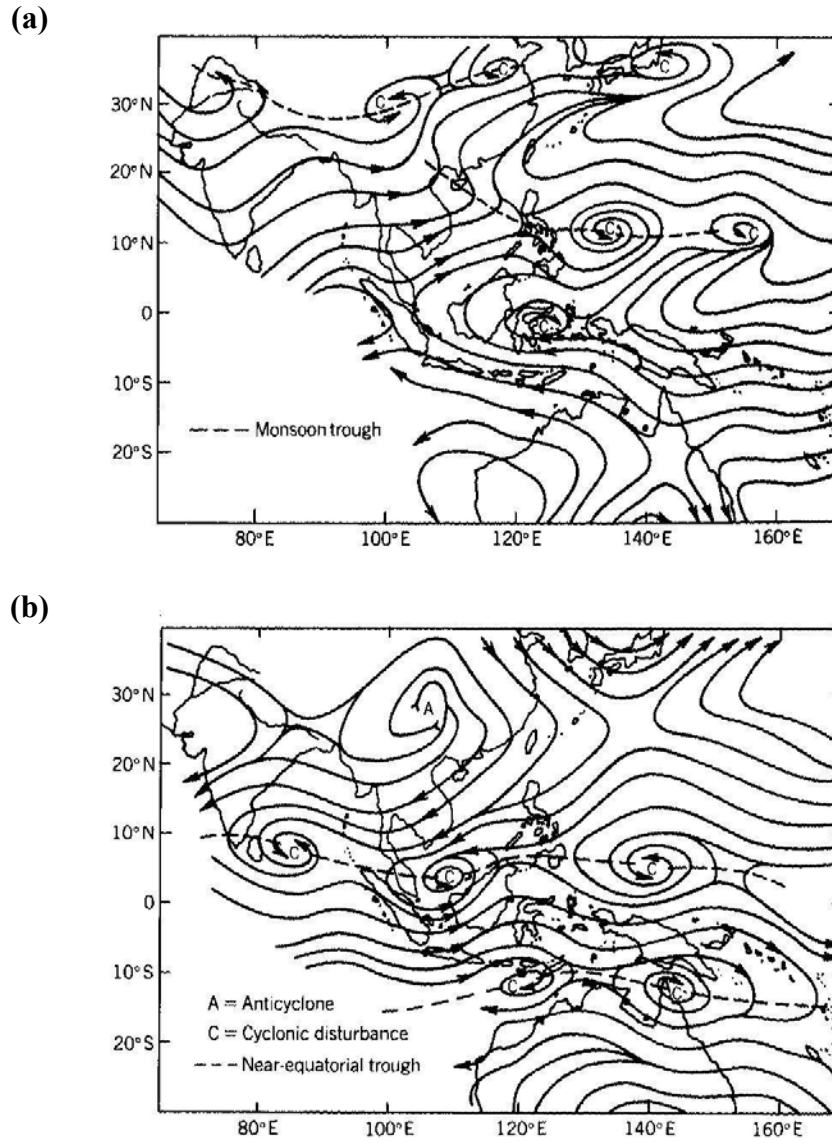
Figure 2　The SCS monsoon wind pattern.　(a) Summer southwest monsoon, and (b) winter northeast monsoon (from Cheang 1987).

III.   TROPICAL CYCLONES

A.   BACKGROUND

Figure 3 shows the spatial distribution of total number of tropical cyclones passing by from 1945 to 1988 (Neumann 1993). During that period, about 26 tropical cyclones are generated every year over the Western North Pacific Ocean. Among them, quite a few pass by the SCS. Besides, a tropical cyclone can pass by the SCS in all the months within a year (McGride 1995). The primary reason is the persistently warm sea surface temperature and the location of the intertropical convergence zone (ITCZ). Annual reports on tropical cyclone by the United States Navy Joint Typhoon Warning Center (JTWC) show that about 80 % of the tropical cyclones are initially generated in the monsoon trough (McGride 1995).

Figure 4 shows the frequency of tropical cyclone occurrence in the Western North Pacific Ocean from 1945 to 1988. The solid line indicates the tropical cyclones with the maximum wind speed higher than 17 m/s, while the shadow area is for the maximum wind speed higher than 33 m/s.

B.   TYPHOON MUIFA (2004)

Typhoon (TY) Muifa is one of the four tropical cyclones passing by the SCS in 2004. It was formed on 11 November and weakened over land on 26 November. The best track passage of TY Muifa (Figure 5) and best track record (Table 1) were provided by the JTWC (2005).

1.   Forming over the Western Pacific

TY Muifa was first originated as a tropical depression on 11 November 2004 in the Western North Pacific Ocean. It moved steadily northwestward passing north of Palau before entering the Philippine Sea. The disturbance was first mentioned by JTWC at 1600UTC 13 November, approximately 400 km north of Palau. The depression was developed into a tropical storm on 14 November. According to its strength, the Japan Meteorological Agency (JMA) first named it Muifa. However, the Philippine Atmospheric, Geophysical, and Astronomical Services Administration (PAGASA) assigned the name Unding at 0000UTC 14 November after the tropical cyclone had invaded their area of responsibility.

Tropical Storm (TS) Muifa was steadily upgraded and moving west-northwestward to the Philippines. It began the clockwise loop at 1200UTC 17 November and continued for several days. On 18 November, the intensity of TY Muifa reached the maximum intensity at 54.0 m/s (115 knots) at 1200UTC and then began a remarkable weakening phase.

The satellite image of TY Muifa (Figure 6) was obtained from the Tropical Rainfall Measuring Mission (TRMM) satellite. The TRMM is a joint mission between NASA and the Japan Aerospace Exploration Agency (JAXA) and capable with both passive and active sensor array. On the image, Muifa was a tropical storm near the central Philippines at 1611UTC 14 November. At this time, the maximum sustained wind was estimated as 18 m/s (35 knots) by JTWC. The cloud-band width of TY Muifa was about 1000 km.

2. Entering the SCS

TY Muifa was weakened further to 48.9 m/s (95 knots) at 0000UTC 19 November and slowly headed towards southwest. It moved south-southwestward slowly across Luzon and entered the SCS. Its intensity was weakened to 30.9 m/s (60 knots) and downgraded to a tropical storm at 0600UTC 20 November.

At 0000UTC 21 November, TS Muifa was intensified to 33.4 m/s (65 knots) and upgraded back to typhoon. Further strengthening occurred as TY Muifa went west-southwestwards across the warm waters of the SCS. The intensity of TY Muifa reached the second peak 46.3 m/s (90 knots) at 1800UTC at ($11.6^\circ N$, $114.4^\circ E$), approximately 800 km east of Vietnam. TY Muifa continued its journey to Vietnam from 22 to 23 November and was weakened again. The maximum velocity was further decreased to 23.2 m/s (45 knots) at 1200UTC 24 November.

3. Weakening

Muifa was weakened to 15.4 m/s (30 knots) and downgraded to tropical depression status at 1200UTC 25 November. At 0000UTC 26 November Muifa turned northward into an environment of increased wind shear and as the intensity had fallen to 12.9 m/s (25 knots), JTWC issued the final warning on TC Muifa. The final position was 250 km south-southwest of Bangkok, Thailand.
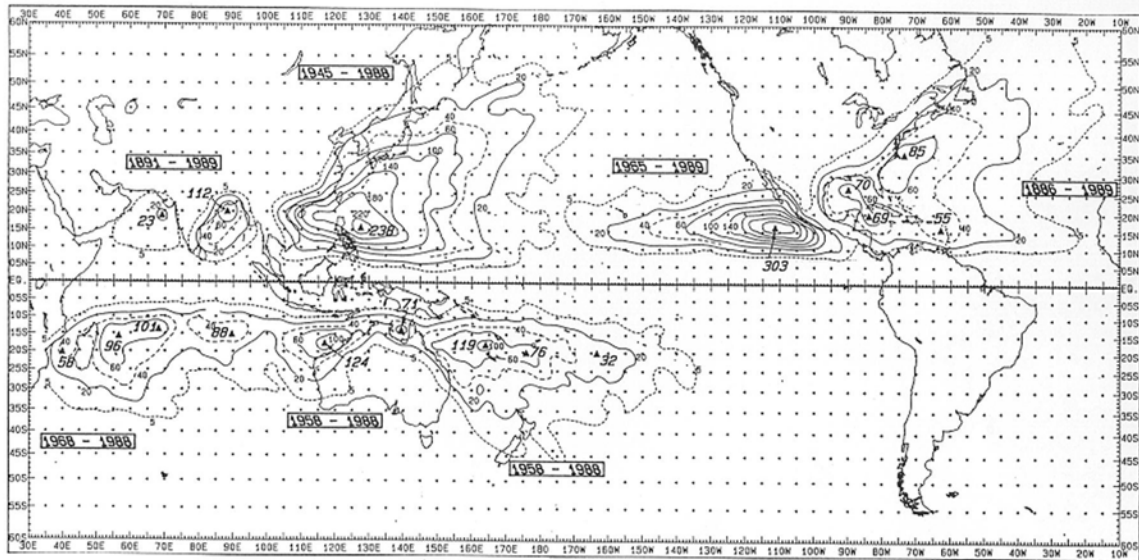
Figure 3   The number of tropical cyclone passages (from Neumann 1993).
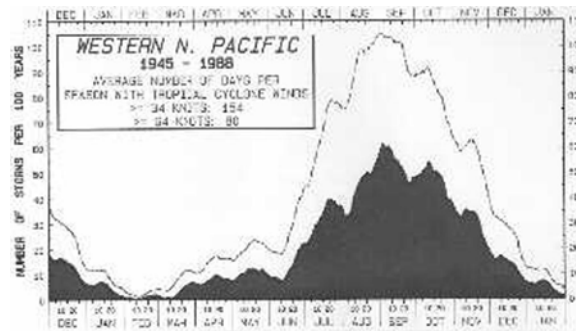
Figure 4   Monthly tropical cyclone frequency in the Western North Pacific Ocean. The upper line represents the maximum wind speed 17 m/sec, while the lower shadow is the maximum wind Speed 33 m/sec (from Neumann 1993).
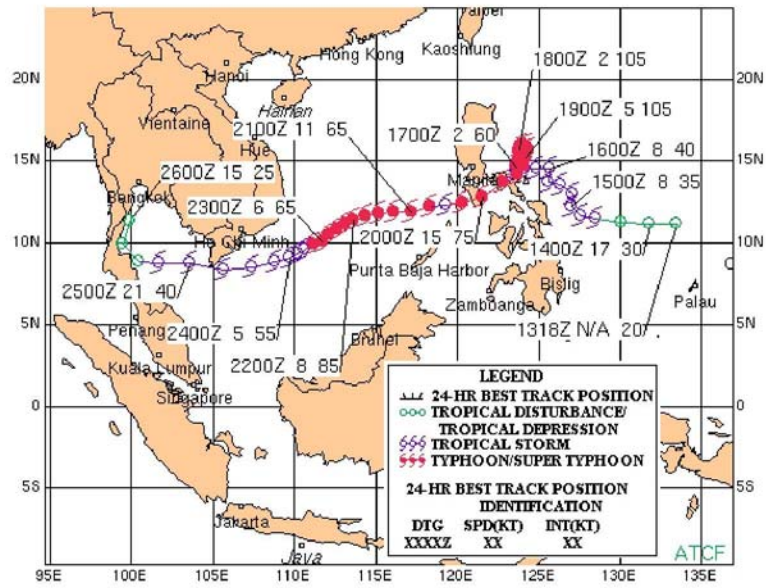
Figure 5   The best track passage of TY Muifa (2004) (from JTWC 2005).
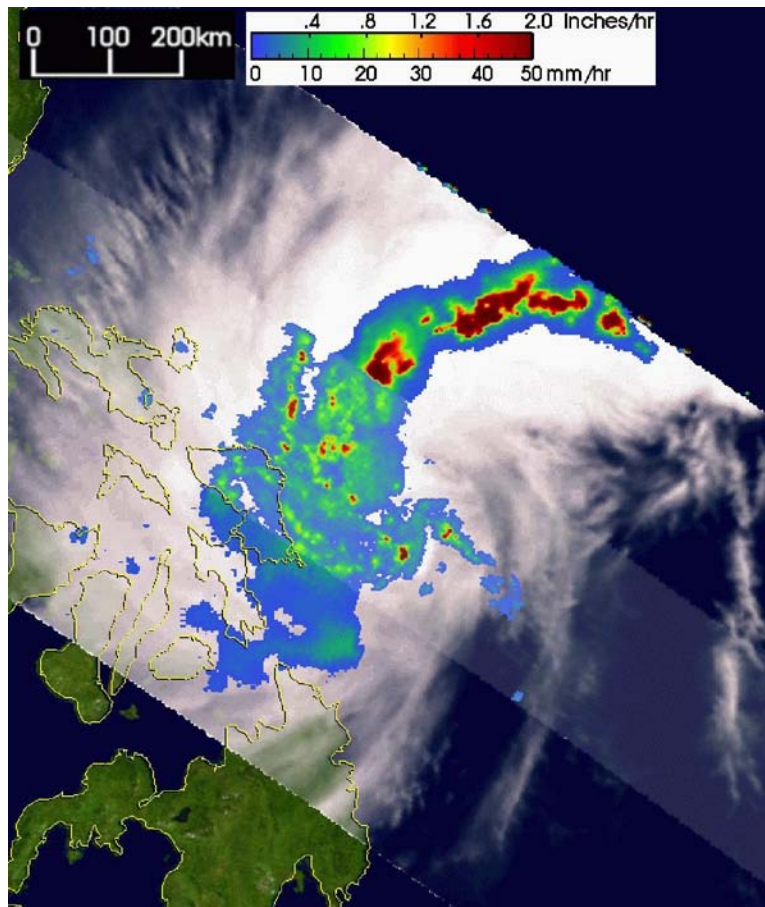
Figure 6   The TRMM microwave image of TS Muifa (2004) at 1611UTC 14 November
close to the central Philippines (from JTWC 2005).

Date	Time	Lat (N)	Long (E)	Type	Pressure (μPa)	V_{max} (m/sec)	R18 (km)	R26 (km)	R33 (km)
11/16/2004	00:00	14.5	125.7	TS	994	20.6	148	--	--
11/16/2004	06:00	14.5	124.9	TS	991	23.1	183	--	--
11/16/2004	12:00	14.5	124.2	TS	984	28.3	183	56	--
11/16/2004	18:00	14.4	123.6	TS	984	28.3	174	56	--
11/17/2004	00:00	14.6	123.6	TS	980	30.9	219	70	--
11/17/2004	06:00	14.8	123.6	TY	976	33.4	213	74	28
11/17/2004	12:00	15.2	123.8	TY	967	38.6	213	74	28
11/17/2004	18:00	15.5	123.8	TY	954	46.3	174	74	46
11/18/2004	00:00	15.7	123.8	TY	938	54	156	65	46
11/18/2004	06:00	15.9	123.9	TY	927	59.2	167	65	46
11/18/2004	12:00	15.9	124.2	TY	927	59.2	170	70	46
11/18/2004	18:00	15.7	124.4	TY	938	54	133	59	41
11/19/2004	00:00	15.2	124.2	TY	938	54	109	59	41
11/19/2004	06:00	14.7	124.1	TY	954	46.3	139	59	41
11/19/2004	12:00	14.2	123.7	TY	958	43.7	144	59	41
11/19/2004	18:00	13.7	122.8	TY	963	41.2	131	56	37
11/20/2004	00:00	12.8	121.6	TY	967	38.6	137	56	37
11/20/2004	06:00	12.5	120.3	TY	976	33.4	137	56	--
11/20/2004	12:00	12.3	119.3	TS	980	30.9	115	56	--
11/20/2004	18:00	12.2	118.3	TY	976	33.4	115	56	--
11/21/2004	00:00	11.9	117.2	TY	976	33.4	128	56	--
11/21/2004	06:00	11.9	116.1	TY	972	36	152	56	28
11/21/2004	12:00	11.8	115.2	TY	963	41.2	152	65	37
11/21/2004	18:00	11.6	114.4	TY	954	46.3	152	65	37
11/22/2004	00:00	11.4	113.6	TY	958	43.7	152	65	37
11/22/2004	06:00	11.1	113.1	TY	958	43.7	126	59	33
11/22/2004	12:00	10.8	112.6	TY	967	38.6	120	52	33
11/22/2004	18:00	10.5	112.1	TY	976	33.4	120	52	33
11/23/2004	00:00	10.1	111.7	TY	976	33.4	120	52	--
11/23/2004	06:00	9.9	111.1	TY	976	33.4	111	56	--
11/23/2004	12:00	9.6	110.6	TS	980	30.9	109	48	--
11/23/2004	18:00	9.3	110.2	TS	984	28.3	107	44	--
11/24/2004	00:00	9.1	109.7	TS	984	28.3	107	44	--
11/24/2004	06:00	8.8	108.8	TS	987	25.7	120	52	--
11/24/2004	12:00	8.5	107.4	TS	994	20.6	102	--	--
11/24/2004	18:00	8.3	105.7	TS	994	20.6	93	--	--
11/25/2004	00:00	8.7	103.6	TS	994	20.6	93	--	--
11/25/2004	06:00	8.7	101.7	TS	997	18	96	--	--

Table 1   The best track record of TY Muifa (2004) from 0000UTC 16 November to
0600UTC 25 November (from JTWC 2005).

THIS PAGE INTENTIONALLY LEFT BLANK

IV.   TYPHOON WINDS

During the typhoon seasons, the in-situ measurements are difficult to conduct. The remotely sensed data [e.g., QuikSCAT (QSCAT)] may provide surface winds. However, due to the spatial coverage, the strong rotational motion from TY Muifa may not be represented in the QSCAT data (Figure 7). To overcome this deficiency, a Tropical Cyclone Wind Profile Model (TCWPM) (Carr and Elsberry 1997) is used to produce the high resolution gridded surface wind field for TY Muifa.

A.   TROPICAL CYCLONE WIND PROFILE MODEL

TCWPM computes the wind field for a tropical cyclone (TC) using a weighted formula by averaging inside and outside of the tropical cyclone (Figure 8)

$$\mathbf{V} = (1-\varepsilon)(\mathbf{V}_c + \mathbf{V}_t) + \varepsilon \mathbf{V}_{bg}, \tag{4.1}$$

where $\mathbf{V}$ is the total wind field, $\mathbf{V}_c = (u,v)$ is the wind vector produced by the TC, $\mathbf{V}_t$ is the wind vector due to the TC translation, and $\mathbf{V}_{bg}$ is the background wind field. Here (u,v) are the TC's radial and tangential velocity components. The weight ε is defined as (Chu et al. 2000)

$$\varepsilon = \frac{c^4}{1+c^4}, \quad c = \frac{r}{0.9R_0}, \tag{4.2}$$

where r is the distance to the center of the TC center, and R_0 is the effective radius defined by

$$v(R_0) = 0. \tag{4.3}$$

1.   Tangential Wind Distribution

Using the angular momentum conservation, the absolute angular momentum (M_a) of a uniform circular vortex is given as

$$M_a(r,p,t) = rv + \frac{1}{2} f_0 r^2, \tag{4.4}$$

15

where f_0 is the Coriolis parameter with respect to the latitude of the TC center. In a symmetrical TC, the absolute angular momentum of an air parcel depends only on the frictional torque

$$\frac{dM_a}{dt} = rF_\theta,$$ (4.5)

where F_θ is the frictional effect in the tangential direction (θ). In the low-level inflow region of the TC, the effect of the frictional torque decreases the angular momentum over time while it spiraling inward to the center of the TC.

For slow temporal change of the TC circulation, M_a depends on r and pressure (p) only. Eq. (4.4) may be rewritten as

$$v(r,p) = \frac{M_a(r,p)}{r} - \frac{1}{2} f_0 r.$$ (4.6)

Since the low-level M_a decreases faster near the center and slower away from the center, M_a is approximately represented by

$$M_a(r,p) = M(p) r^{1-X},$$ (4.7)

where X is a positive constant, Carr and Elsberry (1997) proposed to use $X = 0.4$. Substituting (4.7) into (4.6) gives

$$v(r,p) = \frac{M(p)}{r^X} - \frac{1}{2} f_0 r.$$ (4.8)

To compute the tangential velocity $v(r,p)$, the value of $M(p)$ must be determined. Substituting $r = R_0$ into (4.8) and using (4.3), we have

$$M(p) = \frac{1}{2} f_0 (R_0)^{1+X}.$$ (4.9)

Substituting (4.9) into (4.8) and applying the adjustment factor a, the tangential wind is given by

$$v(r, R_0, R_s) = \frac{f_0}{2} \left[R_0 (\frac{R_0}{r^X})^X - r \right] \frac{a^4}{1-a^4}, \quad a = \frac{r}{R_s}, \tag{4.10}$$

where R_s is the scale radius from the center of the TC.

The radial wind of the TC is computed from the tangential wind

$$u(r) = \cot(\gamma)v(r), \tag{4.11}$$

where γ is the inflow angle of the wind as it spirals into the center of the cyclone (Figure 8). Schwerdt et al. (1979) suggested a relationship between the wind inflow angle γ and the ratio of the radius to the maximum wind radius (R_m) (Figure 9).

2.   Determination of Model Parameters

In the TCWPM, as described in (4.10), the tangential wind depends on the radial distance (r), the scale radius (R_s), and the effective radius (R_0). Carr and Elsberry (1997) determine R_0 from the satellite image according to the size of overall convective and outflow cloud pattern of the TC. On the other hand, Chu et al. (2000) fixed the values of radii for the whole typhoon passage. Since there is no available satellite image of TY Muifa in the SCS, the values of radii of TY Muifa are determined using the data from JTWC (Table 1). Near the typhoon center, the winds reported by JTWC can be approximately taken as the tangential winds. Let tangential winds at $(r_1, r_2, ..., r_k)$ be $(v_1, v_2, ..., v_k)$. Eq. (4.10) gives a set of nonlinear algebraic equations

$$\begin{aligned} v(r_1, R_0, R_s) &= v_1, \\ v(r_2, R_0, R_s) &= v_2, \\ &......, \\ v(r_k, R_0, R_s) &= v_k. \end{aligned} \tag{4.12}$$

An optimization scheme is used to determine the values of radii (R_s, R_0), and to further compute R_m. For example, (R_s, R_0) are estimated as (23.7 km, 795 km) at 0600UTC 24 November. Table 2 shows temporally varying (R_m, R_s, R_0). In this table, the translation speed of TY Muifa is also calculated from the distance between typhoon center positions reported by JTWC.

17

B.   TCWPM APPLICATION ON TY MUIFA (2004)

1.   QuikSCAT Satellite

The QSCAT satellite was launched on 19 June 1999 by NASA with the SeaWinds scatterometer onboard. QSCAT has a sun-synchronous orbit at an altitude of 803 km and a period of 101 minutes. The ascending equator crossing time of it is 0600UTC. SeaWinds consists of a 1 m long, 18 revolutions per minute rotating parabolic antenna, with two offset feeds that generate two 13.4-GHz pencil beams at different incidence angle. Its rotating dish antenna sends out a pair of scanned beams and ranges bins the return from each beam (Martin 2004). The detail description about the design and operation of QSCAT and SeaWinds could be referred to Spencer et al. (1997, 2000) and Liu (2002).

The QSCAT Level 3 dataset, which consists of grid values of scalar and componential wind velocity, is provided by the Jet Propulsion Laboratory (JPL). The Level 3 data is produced on an approximately $1/4° \times 1/4°$ global grid with both ascending and descending passes. Data is available online in Hierarchical Data Format (HDF) form 19 July 1999 to present. The QSCAT Level 3 data were downloaded during the period of TY Muifa (2004). The evolution of QSCAT wind field from 17 to 25 November 2004 (Figure 7) clearly shows that the typhoon strength agrees properly with the progressing of TY Muifa into SCS, but the structure of tropical cyclone winds is not presented well due to temporal limitation of satellite tracks and inaccuracy of scatterometer in high winds.

2.   Combination of QSCAT and TCWPM Winds

When the background wind vector term ($\mathbf{V}_{bg}$) in (4.10) is taken as the temporally averaged QSCAT Level 3 winds from both ascending and descending passes during 16-25 November 2004 (Figure 10). The winds blow from northeast to southwest with the spatial average of about 7.8 m/s. It represents the dominant winter monsoon during the period of TY Muifa passage in the SCS.

With the mean QSCAT wind data as $\mathbf{V}_{bg}$, the total wind field is computed from 0000UTC 16 November to 0600UTC 25 November for ($0°-25°N$, $105°E-122°E$) using (4.10) on a $1/4° \times 1/4°$ grid with the time interval of 6 hr. Such a wind field is referred to the QTCWPM winds. The daily evolution of the QTCWPM winds (Figure 11) shows

that the wind speed increases as TY Muifa enters the SCS, and decreases as Muifa approaches the land. The QTCWPM maximum wind speed is comparable to the maximum wind speed reported in the best track record (46.3 m/s). Furthermore, the QTCWPM wind field shows asymmetric with the higher wind speed in the right side.

The QTCWPM winds are compared to the QSCAT winds on $1/4° \times 1/4°$ as well as to the National Centers for Environmental Prediction (NCEP) surface winds on a $1° \times 1°$ grid (Figure 12). The root mean square error (RMSE) is 3.2 m/s between QTCWPM and NCEP winds and 3.4 m/s between QTCWPM and QSCAT winds (Table 3). During TY Muifa passage in the SCS, the averaged wind speed is around 35 m/s, the computed QTCWPM wind field is reasonably well.

3. Ideal Typhoon Winds without Monsoon

As mentioned above, the SCS background wind field during TY Muifa passage is the winter monsoon. In order to separate and compare typhoon and monsoon forcing for the ocean waves, a set of ideal typhoon winds is generated using (4.10) with zero background winds ($\mathbf{V}_{bg} = 0$). Figure 13 shows the daily evolution of the asymmetric ideal typhoon winds. The maximum wind speed is about 46.3 m/sec. Before arrival and after departure of TY Muifa, the wind speed is closed to zero. Besides, the wind speed is also zero far from the typhoon track.
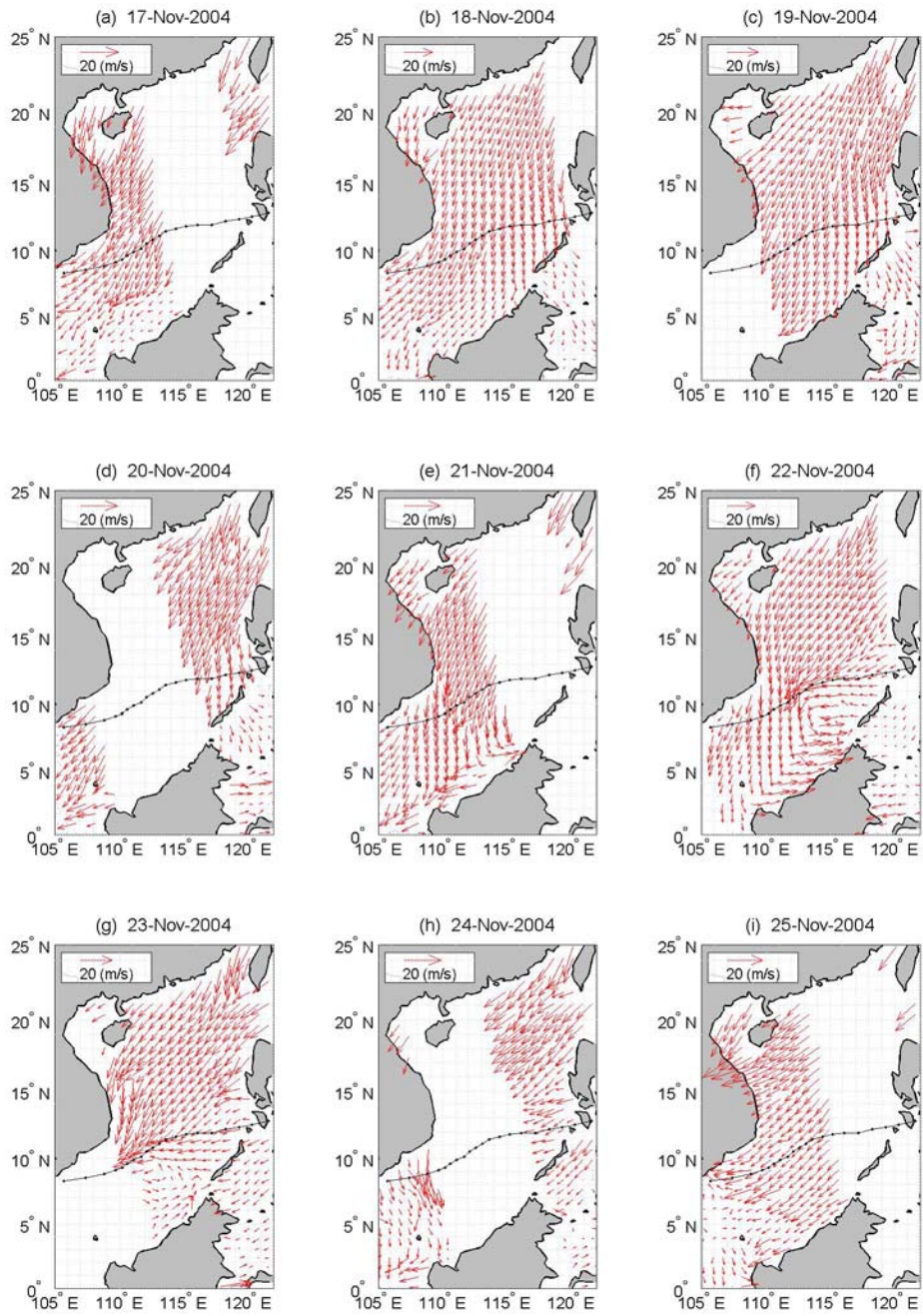
Figure 7   Daily wind field of QSCAT satellite observation on 17-25 November 2004.

$$V = (1-\varepsilon)(V_c + V_t) + \varepsilon V_{bg}$$
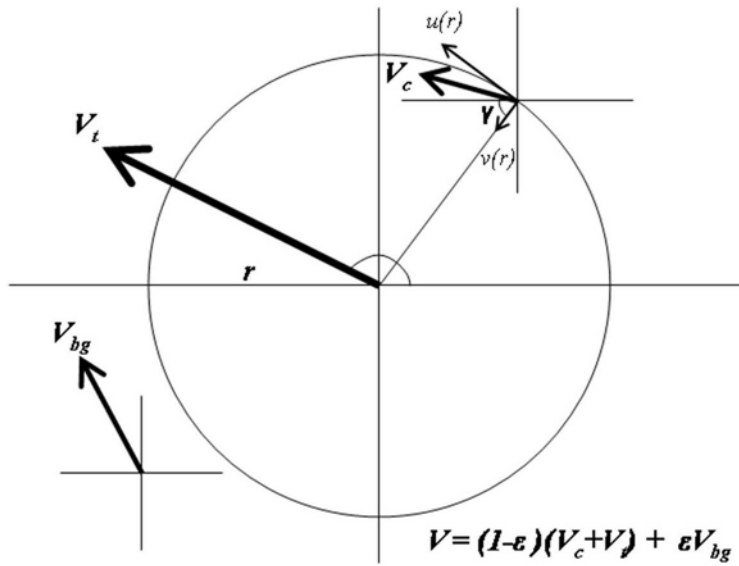
Figure 8   Wind field decomposition of the TCWPM model.
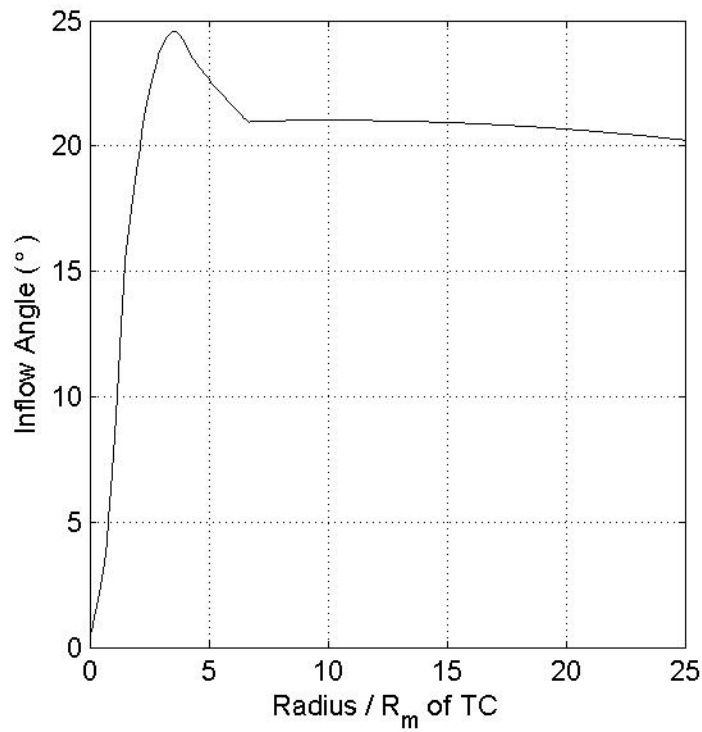
Figure 9   Relation between the wind inflow angle and the relative radius of tropical cyclone (after Schwerdt 1979).
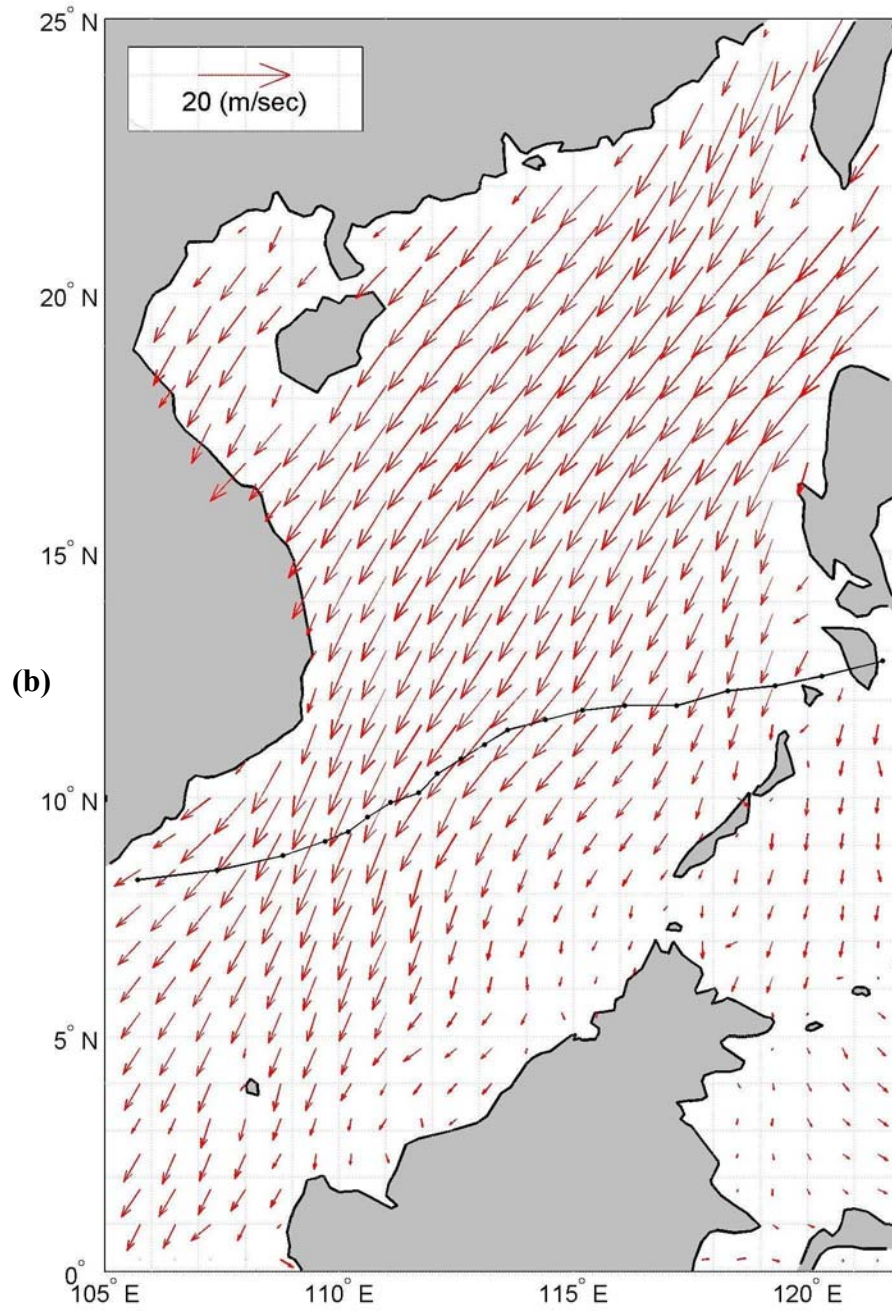
Figure 10   Mean wind field of QSCAT satellite observation from 0000UTC 16 November to
0600UTC 25 November 2004.
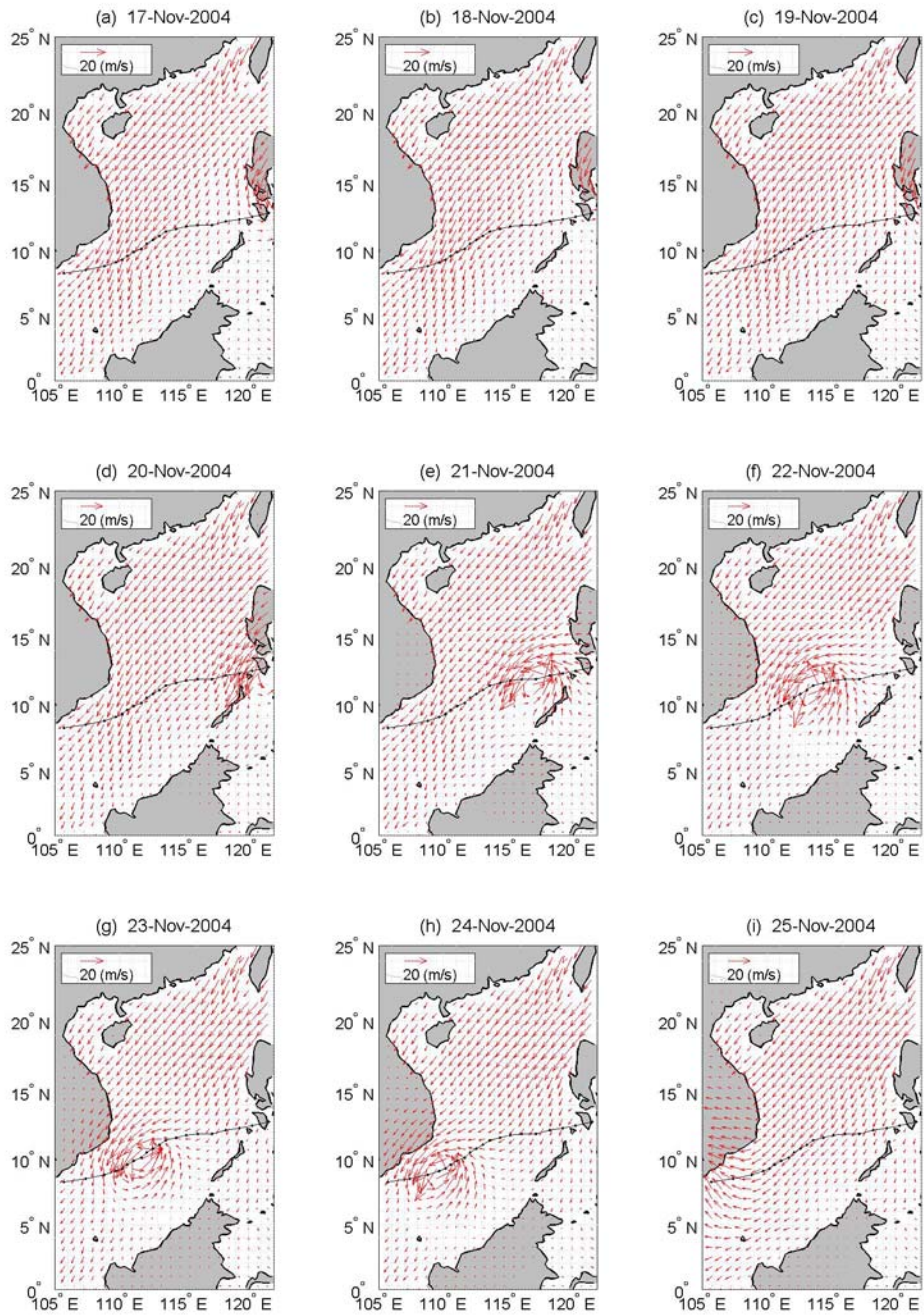
Figure 11   Daily wind field of QTCWPM calculation on 17-25 November 2004.
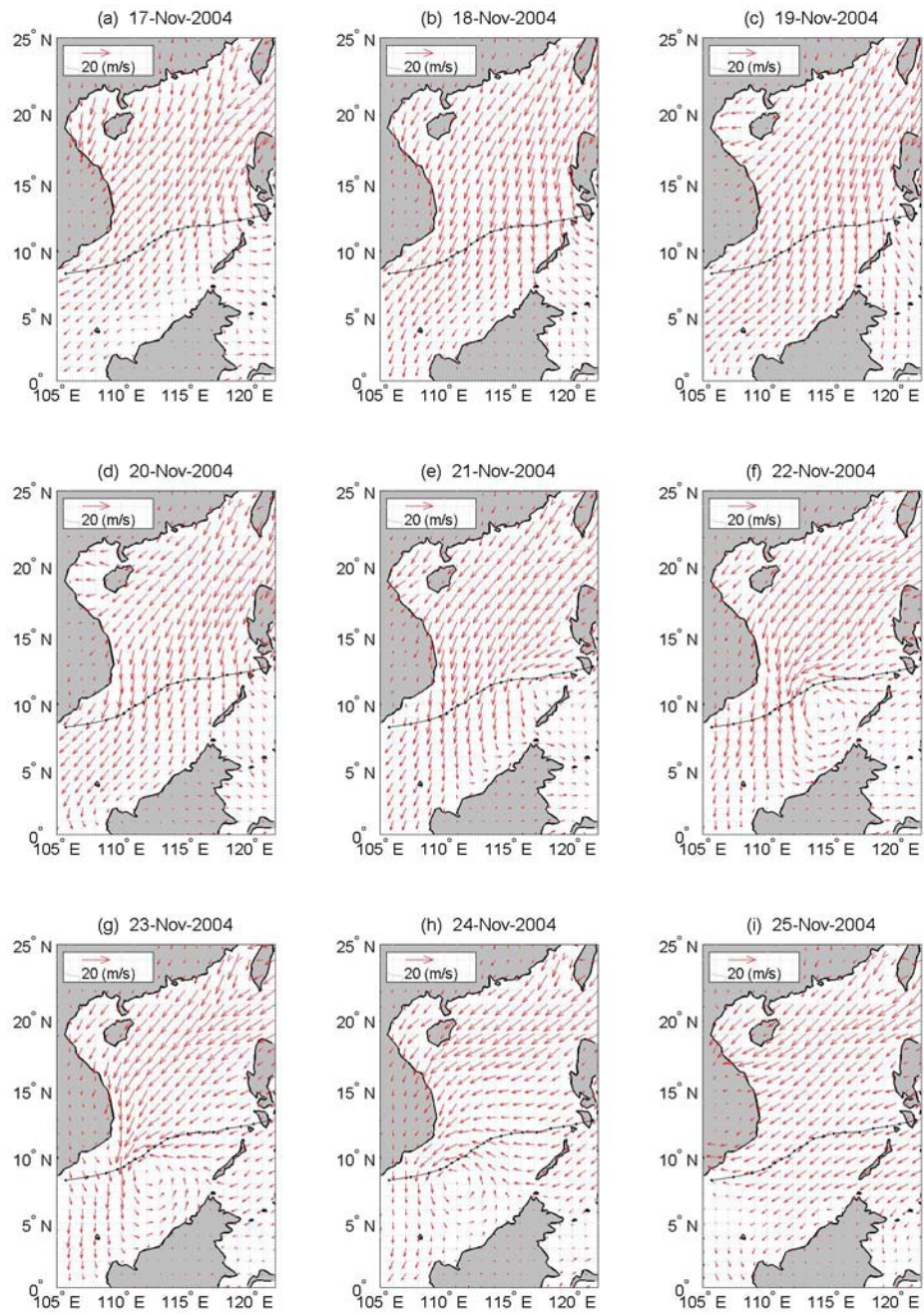
Figure 12   Daily wind field of NCEP Reanalysis dataset on 17-25 November 2004.
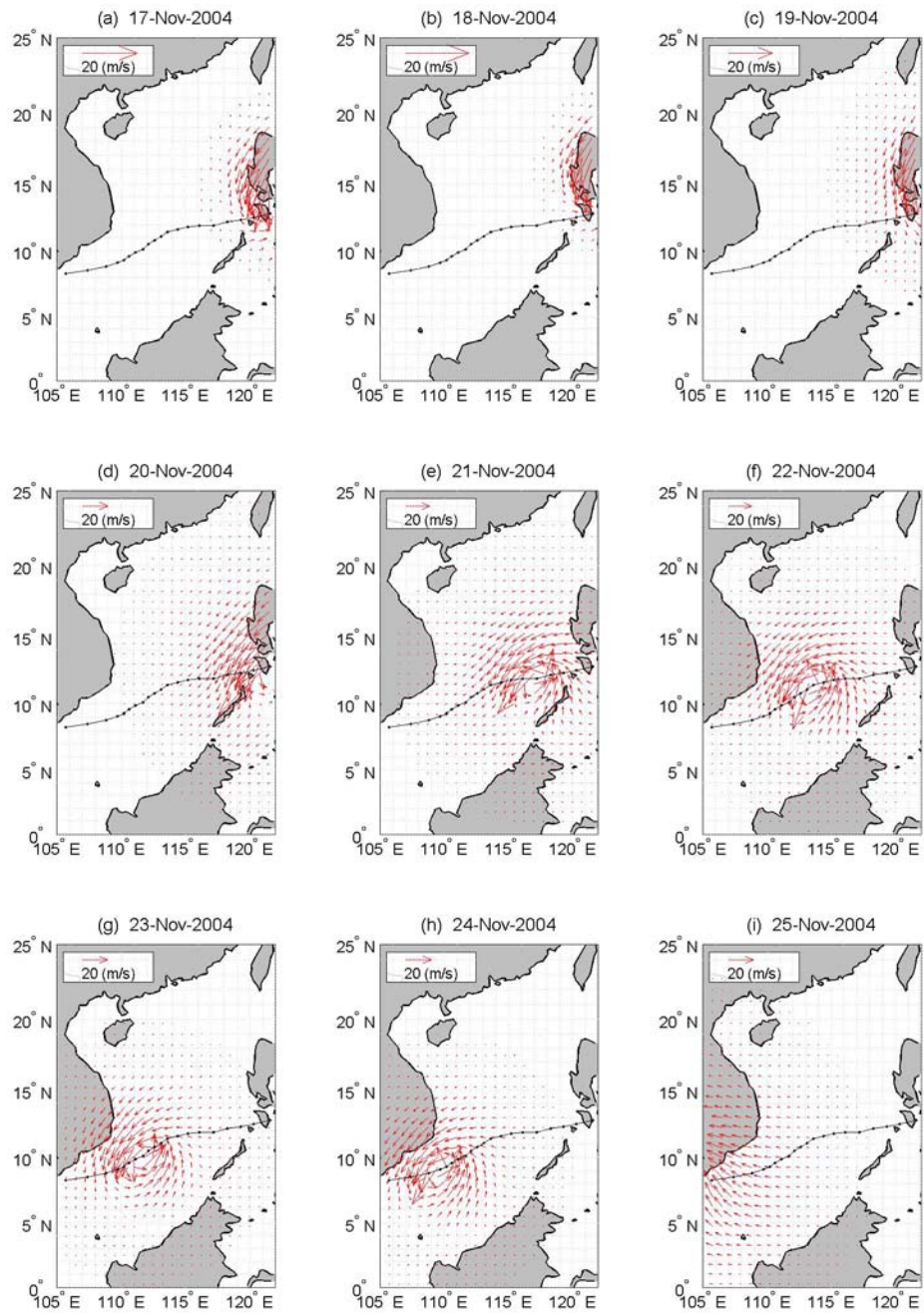
Figure 13   Daily wind field of ideal typhoon on 17-25 November 2004.

Date	Time	Position		TS (m/s)	V_{max} (m/s)	Wind Profile Radii			Estimated Radii		
		Lat (N)	Long (E)			R_{18} (km)	R_{26} (km)	R_{33} (km)	R_s (km)	R_{max} (km)	R_0 (km)
11/16	00:00	14.5	125.7	3.99	20.6	148	--	--	54.8	89.3	630
11/16	06:00	14.5	124.9	3.99	23.1	183	--	--	54.2	88.9	680
11/16	12:00	14.5	124.2	3.49	28.3	183	56	--	43.2	71.8	678
11/16	18:00	14.4	123.6	3.04	28.3	174	56	--	32.6	54.8	666
11/17	00:00	14.6	123.6	1.03	30.9	219	70	--	36.6	61.5	725
11/17	06:00	14.8	123.6	1.03	33.4	213	74	28	18.9	32.2	623
11/17	12:00	15.2	123.8	2.29	38.6	213	74	28	23.8	40.5	725
11/17	18:00	15.5	123.8	1.54	46.3	174	74	46	10.4	17.9	638
11/18	00:00	15.7	123.8	1.03	54.0	156	65	46	8.1	14.0	655
11/18	06:00	15.9	123.9	1.14	59.2	167	65	46	8.1	14.0	693
11/18	12:00	15.9	124.2	1.49	59.2	170	70	46	8.1	14.0	693
11/18	18:00	15.7	124.4	1.43	54.0	133	59	41	8.1	14.0	655
11/19	00:00	15.2	124.2	2.76	54.0	109	59	41	8.1	14.0	670
11/19	06:00	14.7	124.1	2.62	46.3	139	59	41	8.1	14.0	615
11/19	12:00	14.2	123.7	3.26	43.7	144	59	41	9.3	16.0	631
11/19	18:00	13.7	122.8	5.18	41.2	131	56	37	9.8	16.9	629
11/20	00:00	12.8	121.6	7.59	38.6	137	56	37	10.6	18.2	661
11/20	06:00	12.5	120.3	6.71	33.4	137	56	--	15.7	26.9	663
11/20	12:00	12.3	119.3	5.13	30.9	115	56	--	16.8	28.7	646
11/20	18:00	12.2	118.3	5.06	33.4	115	56	--	13.7	23.5	648
11/21	00:00	11.9	117.2	5.75	33.4	128	56	--	14.2	24.4	667
11/21	06:00	11.9	116.1	5.54	36.0	152	56	28	14.7	25.2	710
11/21	12:00	11.8	115.2	4.56	41.2	152	65	37	10.6	18.3	714
11/21	18:00	11.6	114.4	4.16	46.3	152	65	37	8.1	14.0	725
11/22	00:00	11.4	113.6	4.16	43.7	152	65	37	9.1	15.7	729
11/22	06:00	11.1	113.1	2.96	43.7	126	59	33	8.1	14.0	718
11/22	12:00	10.8	112.6	2.96	38.6	120	52	33	10.4	17.9	721
11/22	18:00	10.5	112.1	2.96	33.4	120	52	33	16.7	28.6	763
11/23	00:00	10.1	111.7	2.89	33.4	120	52	--	12.8	22.0	726
11/23	06:00	9.9	111.1	3.21	33.4	111	56	--	11.7	20.1	716
11/23	12:00	9.6	110.6	2.97	30.9	109	48	--	14.3	24.6	733
11/23	18:00	9.3	110.2	2.55	28.3	107	44	--	16.7	28.6	738
11/24	00:00	9.1	109.7	2.74	28.3	107	44	--	16.7	28.6	749
11/24	06:00	8.8	108.8	4.83	25.7	120	52	--	23.7	40.4	795
11/24	12:00	8.5	107.4	7.29	20.6	102	--	--	33.7	56.9	775
11/24	18:00	8.3	105.7	8.72	20.6	93	--	--	30.4	51.5	763
11/25	00:00	8.7	103.6	10.89	20.6	93	--	--	30.5	51.6	739
11/25	06:00	8.7	101.7	9.67	18.0	96	--	--	47.3	78.8	772

Table 2   The translation speed (derived from the best track record as Table 1) and the estimated radii of TY Muifa (2004).

26

Compared Datasets	Wind Speed		Wind Direction	
	Bias (m/sec)	RMSE (m/sec)	Bias (degree)	RMSE (degree)
QTCWPM / QSCAT	-1.902	3.417	-2.446	41.858
QTCWPM / NCEP	-0.190	3.228	-0.287	34.965

Table 3　　The statistics of QTCWPM wind field compared with QSCAT observation and NCEP Reanalysis dataset.

THIS PAGE INTENTIONALLY LEFT BLANK

V. WAVEWATCH-III MODEL

A. MODEL DESCRIPTION

WW3 is a fully spectral third-generation ocean wind-wave model. It has been developed at the Ocean Modeling Branch of the Environmental Modeling Center of NCEP for global and regional sea wave prediction. WW3 was built on the base of WAVEWATCH-I and WAVEWATCH-II, which were developed at the Delft University of Technology and NASA Goddard Space Flight Center, respectively (Tolman1999). The WW3 has been validated over global-scale (Wittmann 2001; Tolman et al. 2002) and regional wave forecasts (Chu et al., 2004).

B. MODEL EQUATIONS

The governing equations and numerical approaches used in WW3 are described here. Further detail can be referred to the WW3 user manual (Tolman 1999). All the notations used here are following the WW3 user manual. The basic assumptions in WW3 are slowly varying depths compared to an individual wave and absent of currents. The former assumption implies a large-scale bathymetry, for which wave diffraction can generally be ignored. The latter suggests the energy of a wave packet is conserved (Tolman 1999).

1. Governing Equation

Assuming incompressible and irrotational flow at the sea surface, the potential function $\Phi(x,z,t)$ is in a simplified relationship that

$$\nabla^2 \Phi(x,z,t) = 0, \tag{5.1}$$

which is also called the Laplace's equation. Furthermore, it has a plane wave solution that

$$\Phi(x,z,t) = \sin(kx - \sigma t) f(z), \tag{5.2}$$

$$f(z) = \eta \cosh\left[k(z+d)\right], \tag{5.3}$$

where k is the wavenumber, σ is the relative radian frequency, d is the mean water

depth, and η is a scale constant. The quasi-uniform wave theory can be applied locally. In a reference frame, the dispersion relation of the relative radian frequency ($\sigma = 2\pi f_r$) is given as

$$\sigma^2 = gk \tanh kd, \tag{5.4}$$

$$\omega = \sigma + \mathbf{k} \bullet \mathbf{U}, \tag{5.5}$$

where f_r is the reference frequency, ω is the absolute radian frequency, $\mathbf{k}$ is the wavenumber vector, and $\mathbf{U}$ is the averaged (in depth and time) current velocity vector.

The WW3 uses a wavenumber-direction spectrum $F(k,\theta)$ as a basic quantity, because of its invariance characteristics with respect to physics of wave growth and decay for variable water depths. In the output, however, the WW3 consists of the traditional frequency-direction spectrum $F(f_r,\theta)$. The transformation between two spectra is calculated by the Jacobean transformations (Tolman 1999).

Because of the wave action $A \equiv E/\sigma$ is conserved, the WW3 uses the wave action density spectrum $N(k,\theta) \equiv F(k,\theta)/\sigma$ within the model. The wave propagation then is described as

$$\frac{DN}{Dt} = \frac{S}{\sigma}, \tag{5.6}$$

where D/Dt represents the total derivative of wave action density spectrum, and S represents the net effect of source and sinks for the spectrum $N(k,\theta)$. This is called the balance equation.

2. Wave Propagation

In a large-scale application as the SCS, the balance equation is transferred to a spherical grid, defined by longitude λ and latitude ϕ as

$$\frac{\partial N}{\partial t} + \frac{1}{\cos\phi}\frac{\partial}{\partial\phi}\dot{\phi}N\cos\theta + \frac{\partial}{\partial\lambda}\dot{\lambda}N + \frac{\partial}{\partial k}\dot{k}N + \frac{\partial}{\partial\theta}\dot{\theta}_g N = \frac{S}{\sigma}, \tag{5.7}$$

$$\dot{\phi} = \frac{c_g\cos\theta + U_\phi}{R}, \tag{5.8}$$

$$\dot{\lambda} = \frac{c_g \sin\theta + U_\phi}{R\cos\phi}, \tag{5.9}$$

$$\dot{\theta}_g = \dot{\theta} - \frac{c_g \tan\phi\cos\theta}{R}, \tag{5.10}$$

where R is the radius of the earth, U_ϕ and U_λ are current components. Eq. (5.7) includes a correction term for propagation along great circles.

3.   Source Terms

The net source term S is considered to consist of four portions, a wind-wave interaction term S_{in}, a nonlinear wave-wave interaction term S_{nl}, a dissipation (or called white-capping) term S_{ds}, and a additional wave-bottom interaction term S_{bot} for shallow water. These terms used in WW3 are as

$$S = S_{in} + S_{nl} + S_{ds} + S_{bot}. \tag{5.11}$$

These source terms are defined for the energy spectra. Since in the WW3, most source terms are directly calculated for the action spectrum, they are denoted as $S \equiv S/\sigma$ in latter content. The source term packages used in this study are, the Tolman and Chalikov (1996) for both input and dissipation terms, the discrete interaction approximation (DIA) method for nonlinear interaction, and the Joint North Sea Wave Project (JONSWAP) formulation for bottom friction.

a.   Tolman and Chalikov (1996) Input Term

The source terms package of Tolman and Chalikov (1996) include input and dissipation terms. The input source term is given as

$$S_{in}(k,\theta) = \sigma\beta N(k,\theta), \tag{5.12}$$

where β is a nondimensional wind-wave interaction parameter, and can be computed as

$$10^4\beta = \begin{cases} -a_1\tilde{\sigma}_a{}^2 - a_2, & \tilde{\sigma}_a \le -1, \\ a_3\tilde{\sigma}_a(a_4\tilde{\sigma}_a - a_5) - a_6, & -1 < \tilde{\sigma}_a < \Omega_1/2, \\ (a_4\tilde{\sigma}_a - a_5)\tilde{\sigma}_a, & \Omega_1/2 < \tilde{\sigma}_a < \Omega_1, \\ a_7\tilde{\sigma}_a - a_8, & \Omega_1 < \tilde{\sigma}_a < \Omega_2, \\ a_9(\tilde{\sigma}_a - 1)^2 + a_{10}, & \Omega_2 < \tilde{\sigma}_a, \end{cases} \tag{5.13}$$

with

31

$$\tilde{\sigma}_a = \frac{\sigma u_\lambda}{g}\cos(\theta - \theta_w), \tag{5.14}$$

where $\tilde{\sigma}_a$ is the nondimensional frequency of a spectral component, θ_w is the wind direction, and u_λ is the wind velocity at a height equal to the apparent wave length

$$\lambda_a = \frac{2\pi}{k\left|\cos(\theta - \theta_w)\right|}. \tag{5.15}$$

The parameters a_1 to a_{10}, Ω_1 and Ω_2 in (5.13) depend on the drag coefficient C_λ at the height of apparent wave length λ_a

$$\begin{aligned}
&\Omega_1 = 1.075 + 75C_{\lambda,} & &\Omega_2 = 1.2 + 300C_\lambda, \\
&a_0 = 0.25a_5^2 / a_4, & &a_1 = 0.25 + 395C_\lambda, \\
&a_2 = 0.35 + 150C_\lambda, & &a_3 = (a_0 - a_2 - a_1)/(a_0 - a_4 + a_5), \\
&a_4 = 0.30 + 300C_\lambda, & &a_5 = a_4\Omega_1, \\
&a_6 = a_0(1 - a_3), & &a_7 = (a_9(\Omega_2 - 1)^2 + a_{10})/(\Omega_2 - \Omega_1), \\
&a_8 = a_7\Omega_1, & &a_9 = 0.35 + 240C_\lambda, \\
&a_{10} = -0.05 + 470C_\lambda.
\end{aligned} \tag{5.16}$$

The wave model take the wind u_r at a given reference height z_r (in this study uses 10 m) as its input, so that u_λ and C_λ need to be derived as part of the parameterization. Excluding a thin surface layer adjusting to the water surface the mean wind profile is close to logarithmic

$$u_r = \frac{u_*}{\kappa}\ln(\frac{z_r}{z_0}), \tag{5.17}$$

where $\kappa = 0.4$ is the *Von Karman* constant, and z_0 is the roughness parameter. This equation can be rewritten in terms of the drag coefficient C_r at the reference height z_r as

$$C_r = \kappa^2\left[R - \ln(C)\right]^2, \tag{5.18}$$

with

$$R = \ln\left(\frac{z_r g}{\chi\sqrt{\alpha}u_r^2}\right), \tag{5.19}$$

where $\chi = 0.2$ is a constant, and α is the conventional nondimensional energy level at high frequencies. An accurate explicit approximation to these implicit relations is given as

$$C_r = 10^{-3} \left(0.021 + \frac{10.4}{R^{1.23} + 1.85} \right). \tag{5.20}$$

The estimation of the drag coefficient thus requires an estimate of the high-frequency energy level α, which could be estimated directly from the wave model. However, the corresponding part of the spectrum is generally not well resolved, tends to noisy, and it tainted by errors in several source terms. Therefore, α is estimated parametrically as (Janssen 1989)

$$\alpha = 0.57 \left(\frac{u_*}{c_p} \right)^{3/2}. \tag{5.21}$$

Using the definition of drag coefficient and (5.20), the roughness parameter z_0 becomes

$$z_0 = z_r \exp\left(-\kappa C_r^{-1/2} \right), \tag{5.22}$$

and the wind velocity and drag coefficient at height λ_a become

$$u_\lambda = u_r \frac{\ln(\lambda_a / z_0)}{\ln(z_r / z_0)}, \tag{5.23}$$

$$C_\lambda = C_r \left(\frac{u_a}{u_\lambda} \right)^2. \tag{5.24}$$

Finally, (5.21) requires an estimate for the peak frequency f_p. To obtain a consistent estimate of the peak frequency of actively generated waves, even in complex multi-modal spectra, this frequency is estimated from the equivalent peak frequency of the positive part of the input source term

$$f_{p,i} = \frac{\iint f^{-2} c_g^{-1} \max\left[0, S_{in}(k,\theta) \right] df d\theta}{\iint f^{-3} c_g^{-1} \max\left[0, S_{in}(k,\theta) \right] df d\theta}, \tag{5.25}$$

from which the actual peak frequency is estimated as

$$\tilde{f}_p = 3.6 \times 10^{-4} + 0.92 \tilde{f}_{p,i} - 6.3 \times 10^{-10} \tilde{f}_{p,i}^{-3}. \tag{5.26}$$

Furthermore, to reduce the swell due to opposing or weak winds, a filtered input source term is defined as

$$S_{in} = \begin{cases} S_{in} & \text{for} \quad \beta \geq 0 \quad \text{or} \quad 0.8 f_p < f, \\ X_s S_{in} & \text{for} \quad \beta < 0 \quad \text{and} \quad 0.6 f_p < f < 0.8 f_p, \\ X_s S_{in} & \text{for} \quad \beta < 0 \quad \text{and} \quad f < 0.6 f_p, \end{cases} \tag{5.27}$$

where f is the frequency, f_p is the peak frequency of the wind sea as computed from the input source term, and $0 < X_s < 1$ is a reduction factor for S_{in}, which is applied to swell with negative β. X_s represents a linear reduction of X_s with f_p providing a smooth transition between the original and reduced input.

b. Tolman and Chalikov (1996) Dissipation Term

The dissipation source term consists of two constituents. The dominant low-frequency constituent is based on an analogy with energy dissipation due to turbulence,

$$S_{ds,l}(k,\theta) = -2u_* h k^2 \phi N(k,\theta),$$
$$h = 4 \left(\int_0^{2\pi} \int_{f_h}^{\infty} F(f,\theta) df d\theta \right)^{1/2}, \tag{5.28}$$
$$\phi = b_0 + b_1 \tilde{f}_{p,i} + b_2 \tilde{f}_{p,i}^{-b_3},$$

where h is a mixing scale determined from the high-frequency energy content of the wave field and where ϕ is an empirical function accounting for the development stage of the wave field. By defining a minimum value $\phi_{\min}$ for ϕ at minimum frequency $f_{p,i,\min}$, the nonlinear term has been added to allow for some control over fully grown conditions. If $\phi_{\min}$ is below the linear curve, b_2 and b_3 are given as

$$b_2 = \tilde{f}_{p,i,\min}^{-b_3} \left(\phi_{\min} - b_0 - b_1 \tilde{f}_{p,i,\min} \right),$$
$$b_3 = 8. \tag{5.29}$$

If $\phi_{\min}$ is above the linear curve, b_2 and b_3 are given as

34

$$\tilde{f}_a = \frac{\phi_{\min} - b_0}{b_1}, \tilde{f}_b = \max\left\{\tilde{f}_a - 0.0025, \tilde{f}_{p,i,\min}\right\},$$

$$b_2 = \tilde{f}_{p,i,\min}{}^{b_3}\left[\phi_{\min} - b_0 - b_1\tilde{f}_b\right], \tag{5.30}$$

$$b_3 = \frac{b_1\tilde{f}_b}{\phi_{\min} - b_0 - b_1\tilde{f}_b}.$$

The above estimate of b_3 results in $\partial\phi/\partial\tilde{f}_{p,i} = 0$ for $\tilde{f}_{p,i} = \tilde{f}_b$. For $\tilde{f}_{p,i} < \tilde{f}_b$, the ϕ is kept constant that $\phi = \phi_{\min}$.

The empirical high-frequency dissipation id defined as

$$S_{ds,h}(k,\theta) = -a_0\left(\frac{u_*}{g}\right)^2 f^3\alpha_n^B N(k,\theta),$$

$$B = a_1\left(\frac{fu_*}{g}\right)^{-a_2}, \tag{5.31}$$

$$\alpha_n = \frac{\sigma^6}{c_g g^2 a_r}\int_0^{2\pi} N(k,\theta)d\theta,$$

where α_n is Phillips'(1957) nondimensional high-frequency energy level normalized with α_r, and where a_0 through a_3 and α_r are empirical constant.

The two constituents of the dissipation source term are combined using a simple linear combination, defined by the frequencies f_1 and f_2.

$$S_{ds,h}(k,\theta) = \mathcal{A}S_{ds,l} + (1-\mathcal{A})S_{ds,h},$$

$$\mathcal{A} = \begin{cases} 1 & \text{for} \quad f < f_1 \quad , \\ \dfrac{f - f_2}{f_1 - f_2} & \text{for} \quad f_1 \leq f < f_2 \quad , \\ 0 & \text{for} \quad f_2 \leq f \quad . \end{cases} \tag{5.32}$$

To enhance the smoothness of the model behavior for frequencies near the parametric cut-off f_{hf}, the parametric high-frequency tail as

$$N(k_i,\theta) = (1-\mathcal{B})N(k_i,\theta) + \mathcal{B}N(k_{i-1},\theta)\left(\frac{f_i}{f_{i-1}}\right)^{-m-2}, \tag{5.33}$$

where i is a discrete wavenumber counter, m is set to 5, and where $\mathcal{B}$ is defined similarly to $\mathcal{A}$, ranging from 0 to 1 between f_2 and f_{hf}. The frequencies defining the transitions and the length scale h are predefined in the model as

$$\begin{cases} f_{hf} = 3.00 f_{p,i}, \\ f_1 = 1.75 f_{p,i}, \\ f_2 = 2.50 f_{p,i}, \\ f_h = 2.00 f_{p,i}. \end{cases} \tag{5.34}$$

c.   Nonlinear Interaction Term

Nonlinear wave-wave interactions are modeled using the DIA method (Hasselmann et al. 1985). This parameterization was originally developed for the spectrum $F(f_r, \theta)$. To assure the conservation nature of S_{nl} for this spectrum, this source term is calculated for $F(f_r, \theta)$ instead of $N(k, \theta)$.

Resonant nonlinear interactions occur between four wave components (quadruplets) with wavenumber vector $\mathbf{k}_1$ through $\mathbf{k}_4$. In the DIA, it is assumed that $\mathbf{k}_1 = \mathbf{k}_2$. Resonance conditions then require that

$$\begin{cases} \mathbf{k}_1 + \mathbf{k}_2 = \mathbf{k}_3 + \mathbf{k}_4, \\ \sigma_2 = \sigma_1, \\ \sigma_3 = (1 + \lambda_{nl})\sigma_1, \\ \sigma_4 = (1 - \lambda_{nl})\sigma_1, \end{cases} \tag{5.35}$$

where λ_{nl} is a constant. For these quadruplets, the contribution δS_{nl} to the interaction for each discrete (f_r, θ) combination of the spectrum corresponding to $\mathbf{k}_1$ is calculated as

$$\begin{pmatrix} \delta S_{nl,1} \\ \delta S_{nl,3} \\ \delta S_{nl,4} \end{pmatrix} = D \begin{pmatrix} 2 \\ -1 \\ -1 \end{pmatrix} C g^{-4} f_{r,1}^{11} \times \left[F_1^2 \left(\frac{F_3}{(1+\lambda_{nl})^4} + \frac{F_4}{(1-\lambda_{nl})^4} \right) - \frac{F_1 F_3 F_4}{(1-\lambda_{nl}^2)^4} \right], \tag{5.36}$$

where $F_1 = F(f_{r,1}, \theta_1)$ and $\delta S_{nl,1} = \delta S_{nl}(f_{r,1}, \theta_1)$, and so others, C is a proportionality constant. In this study the values suggested by Tolman and Chalikov (1996) is applied that $\lambda_{nl} = 0.25$ and $C = 1.00 \times 10^7$.

The water depth is scaled by the factor D as

$$D = 1 + \frac{c_1}{\overline{kd}}\left[1 - c_1 \overline{kd}\right]e^{-c_3 \overline{kd}}. \tag{5.37}$$

Recommended values for these constants are $c_1 = 5.5$, $c_2 = 5/6$, and $c_3 = 1.25$ (Hasselmann and Hasselmann 1985). The over-bar notation denotes straightforward averaging over the spectrum. For an arbitrary parameter z the spectral average is given as

$$\begin{aligned}
\overline{z} &= E^{-1}\int_0^{2\pi}\int_0^{\infty} zF(f_r, \theta)df_r d\theta, \\
E &= \int_0^{2\pi}\int_0^{\infty} F(f_r, \theta)df_r d\theta.
\end{aligned} \tag{5.38}$$

For numerical reasons, however, the mean relative depth is estimated as

$$\overline{kd} = 0.75\hat{k}d, \tag{5.39}$$

where $\hat{k}$ is defined as

$$\hat{k} = \left(\overline{1/\sqrt{k}}\right)^{-2}. \tag{5.40}$$

d.   JONSWAP Bottom Friction Term

The JONSWAP parameterization of bottom friction is simply represented by (Hasselmann et al. 1973)

$$S_{bot}(k, \theta) = 2\Gamma\frac{n - 0.5}{gd}N(k, \theta), \tag{5.41}$$

where Γ is an empirical constant, which is estimated and as $\Gamma = -0.067 m^2/s^3$ for wind sea (Bouws and Komen 1983).

C. MODEL VERIFICATION

The WW3 was integrated for the SCS from 3 January to 31 December 2000 using twice daily gridded QSCAT ocean winds, and verified (Chu et al. 2004) using the significant wave height (H_s) obtained from T/P satellite and the European Remote Sensing Satellites ERS-1/2 (Figure 14). The WW3 model errors stratify the Gaussian-type distribution with the RMSE of 0.48 m, which is comparable to the T/P altimeter accuracy 0.5 m. This shows the capability of WW3 for SCS wave simulation.
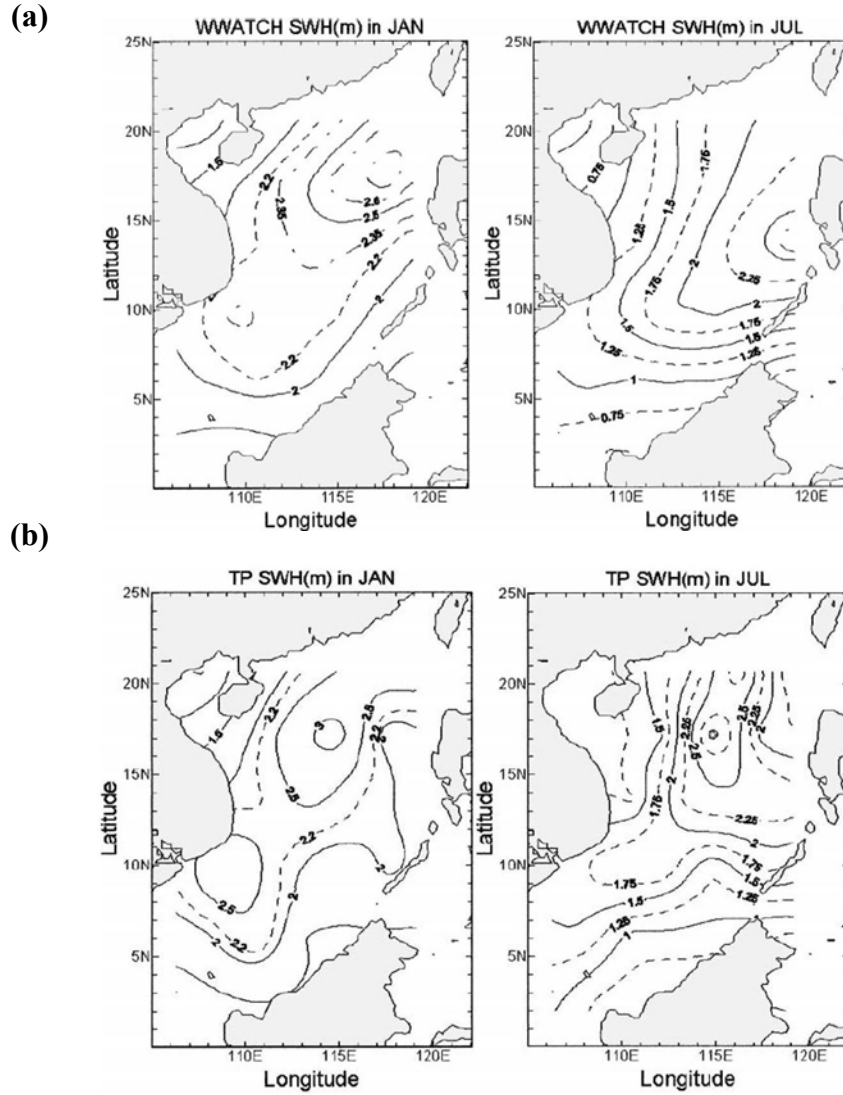
Figure 14   Monthly mean significant wave height (H_s) from (a) WW3 simulations, and (b) T/P observations (from Chu et al. 2004).

THIS PAGE INTENTIONALLY LEFT BLANK

VI.   RELATIONSHIPS BETWEEN WAVES AND WINDS

Surface winds have large variability in space and time. Different winds generate different wave patterns. For slowly varying winds, change of waves follows the change of winds (local equilibrium). For fast varying winds such as tropical cyclones, change of waves does not follow the change of winds (non-local equilibrium). Wave field must respond to the directional change as well as the magnitude variation of wind forcing (Jones and Toba 2001).

A.   GENERAL RESPONSES

1.   Wind Speed

While steady winds transfer momentum through the sea surface via waves, the wave field also plays an important role in this momentum transfer through motion and adjustment. As the adjustment is finished, the continuity between winds and momentum fluxes would be achieved in both air and sea boundary layers. Toba (1972) referred this balance condition as the "local equilibrium."

Toba et al. (1988) reanalyzed the dataset of Shirahama (also in Kawai et al. 1977) to investigate the response of one-dimensional wave frequency spectra to unsteady winds. Figure 15 shows the one-dimensional wave spectra under increasing wind (Figure 15a), steady wind (Figure 15b), and decreasing wind (Figure 15c). The tendency of the peak can be clearly seen in all three panels. For a rapid increase in wind speed (Figure 15a), the wave field becomes under-saturated. The energy decreases near the spectral peak. Higher wind speed also increases the amplitude of waves, and the higher frequency waves increase and remove momentum from the air. When the reduction in wind speed occurs (Figure 15c), the wave field is over-saturated. The peak energy increases and becomes steeper. The high-frequency waves decrease and tend to extract less momentum from the air.

A further study was conduced from the laboratory experiments of Waseda et al. (2001). The spectral development for a rapid change between low winds (4.6 m/s) and high winds (7.1 m/s) is shown in Figure 16. Two wave adjustment states exist for increasing and decreasing winds. During the rapid adjustment stage, changes of low-

frequency wave energy are not evident whereas the changes of high-frequency wave energy are evident. After the rapid adjustment period, the wave field evolves to a conventional growth and propagation stage. As the wind reduces, the peak frequency shifts toward the high frequency domain; the steepness and peak of the wave spectrum reduce. On the other hand, as the wind enhances, the peak frequency shifts toward the low frequency domain; the steepness and peak of the wave spectrum enhance.

2. Wind Direction

The properties of directional wave spectra under veering wind were investigated by several measurements (Hasselmann et al. 1980; Allender et al. 1983; Walsh et al. 1989; Masson 1990). The high-frequency waves respond more quickly to a directional wind shift than the low-frequency waves. Small wind shift gradually rotates the wave spectrum in accordance to the new wind direction. Large wind shift generates a second wave packet in the new wind direction with gradually decaying old wave packet. After the local equilibrium between the wave spectra and winds is established, the old wave energy still travels in the initial direction. This can be treated as swell at an angle to the younger wind-waves.

Figure 17 shows the directional evolution of five wave packets with inshore and offshore wind shifts in an open ocean. The wave response to the changing wind direction strongly depends on the frequency.

The misalignment of the atmospheric surface layer wind, stress vector, and dominant wave direction were also reported in field observations (Smith 1980; Geernaert 1988; Long et al. 1994). The directional wave spectra derived from Surface Contour Radar (SCR) (Figure 18) shows that the surface wind stress vector and the dominant wave direction do not always parallel the mean wind direction, and that the wave spectra are asymmetric left and right of the wind. Rapid change in wind direction causes initially non-local equilibrium between the wave spectra and winds (Jones and Toba 2001).

3. Strong Cyclonic Forcing

Observational studies were conducted on the wave characteristics under strong cyclonic forcing. Wyatt (1995) measured the directional spectra of storm waves and to examine the effect of wave fetch in the Celtic Sea using the high-frequency radar. Holt et al. (1998) determined the wave field from an intense storm using the synthetic aperture

radar (SAR) imagery from ERS-1 satellite. Wright et al. (2001) investigated the spatial variation of directional wave spectra during hurricane Bonnie using the NASA Scanning Radar Altimeter (SRA). They found that: (1) wind change may cause rapid change in short-wave direction but not in the mean direction of the long-waves; and (2) the highest and longest waves occur in the right forward quadrant of the hurricane (Figure 19).

B.   NUMERICAL MODELING

1.   Source Terms

As mentioned earlier, the source term package of Tolman and Chalikov (1996) is chosen for the WW3 modeling in this study. The chosen wind-input term (S_{in}) has several improved features,

- It becomes negative for waves traveling at large angle with the wind or faster than the wind.

- It results in a two to three times smaller integral input of energy for fully grown sea.

- At high frequencies it results in a larger energy input than previous relation, and the integral input for young waves is more consisted with previous relation.

Also, the wave dissipation term (S_{ds}) is divided into two constitutes according to different characteristics in the frequency domain. In low-frequency domain, S_{ds} is calculated using the wave energy dissipation due to oceanic turbulence. In high-frequency domain, S_{ds} is parameterized using the assumption of quasi-steady balance of source terms (Tolman and Chalikov 1996).

2.   WW3 Model Simulation

Recently, Moon et al. (2003, 2004a, 2004c) investigated the effect of hurricane wind forcing on surface waves and air-sea momentum exchange using WW3 with various wind fields. These wind fields are either idealized or computed from observational data (during hurricane Bonnie 1998).

Figure 21 shows the directional wave spectra at four points on the circle around the storm center with a radius of R_m. Three different hurricane translation speeds (HTS), 0 m/s, 5 m/s, and 10 m/s, were used in the calculation. As the storm moves faster, the

wave spectra in the east and the north locations show a unilateral shape due to resonance effect, while the spectra in the west and the south locations have a more complex structure.

The spatial distribution of H_s and dominant wave direction under various HTS is represented in Figure 22. As HTS increases, waves in the front-right quadrant of the storm track become higher and longer, while those in the rear-left quadrant become lower and shorter. That is to say the hurricane-generated wave field is mostly determined by two factors: the distance from the hurricane center and the HTS.

Figure 23 shows the relation of the drag coefficient (C_d) with the wave age and the driving wind speed. It is found that the drag coefficient depends on both the wind speed and the wave age; it decreases with the wave age at lower wind speed but increases with the wave age at very high wind speed (above 40 m/s) (Moon et al. 2004b).
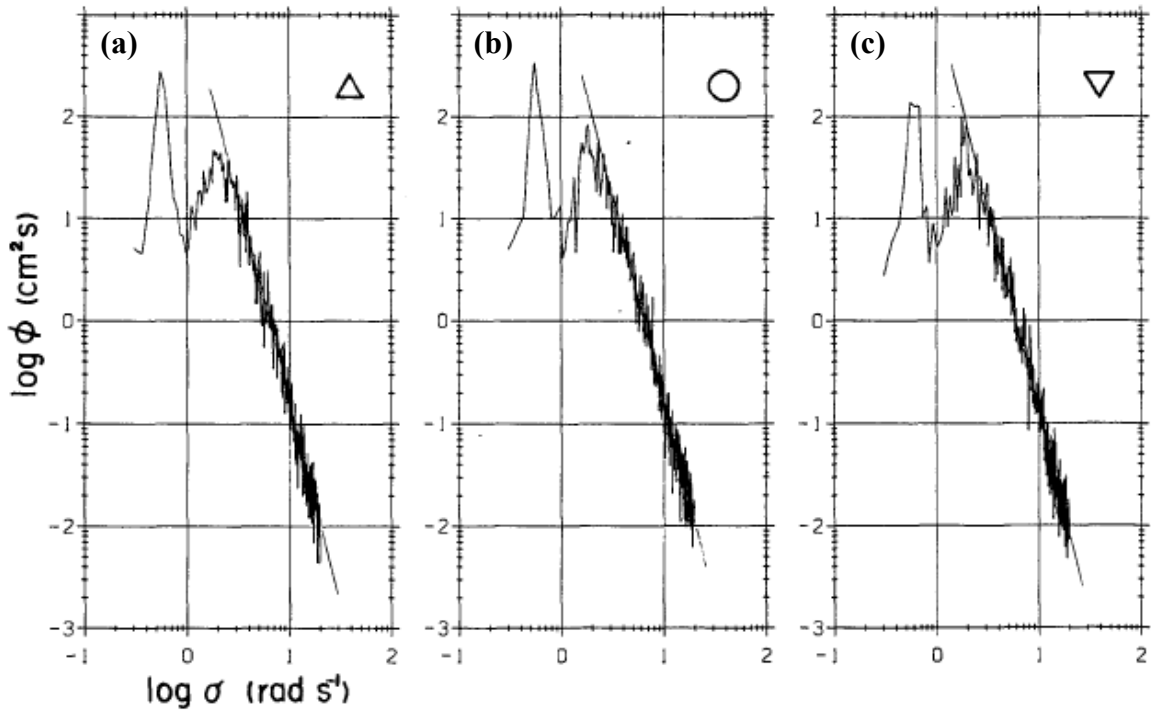
Figure 15   Ensemble means of ten raw spectra under (a) increasing wind (triangle), (b) steady wind (circle), and (c) decreasing wind (inverse triangle) (from Toba et al. 1988).
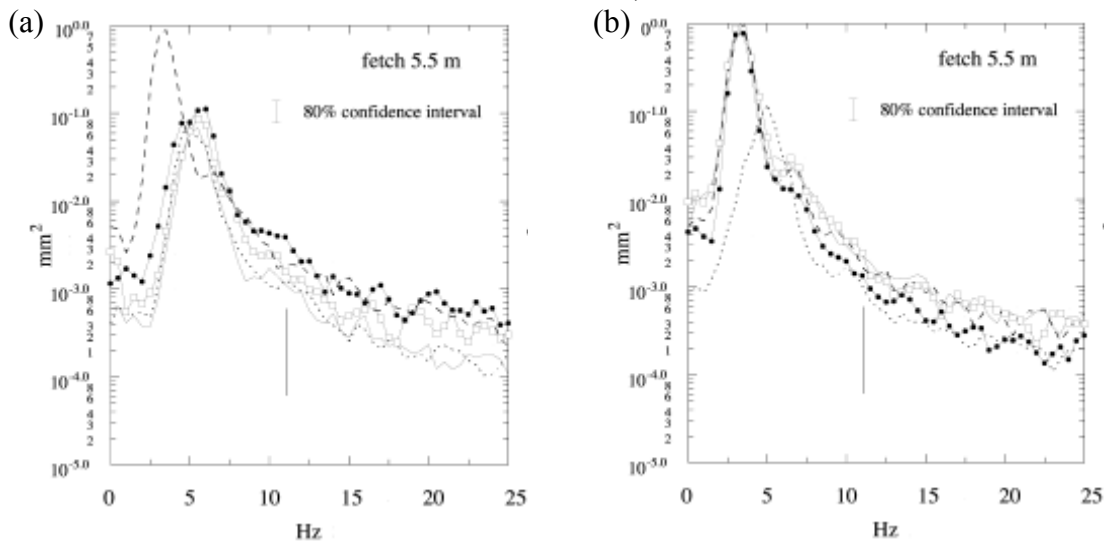
Figure 16   Spectral development for sudden change of wind Speed, (a) increasing wind case, and (b) decreasing wind case. Time steps are initial equilibrium (solid line), 1 second after change (square mark), 4 second after change (solid circle mark), and final equilibrium (dashed line), respectively (from Waseda et al. 2001).
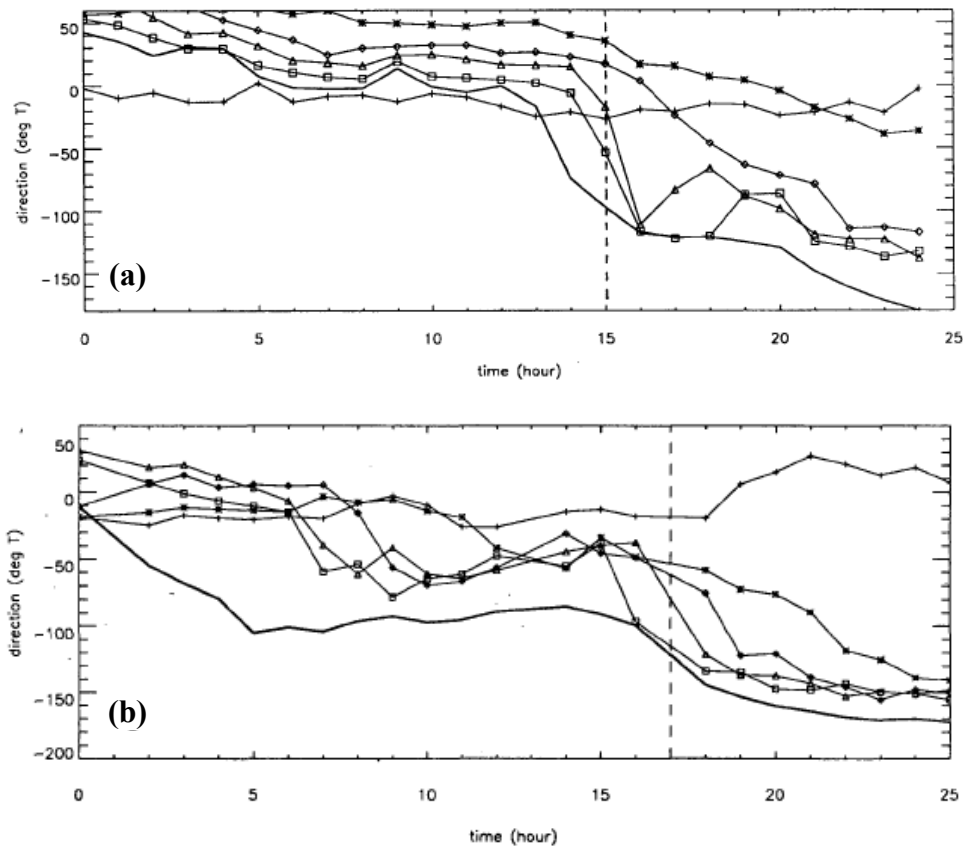
Figure 17   Wind direction (solid line no symbol) and mean wave direction at frequency of 0.10 (plus mark), 0.20 (star), 0.31 (diamond), and 0.54 (square) Hz, under (a) inshore wind, and (b) offshore wind (from Masson 1990).
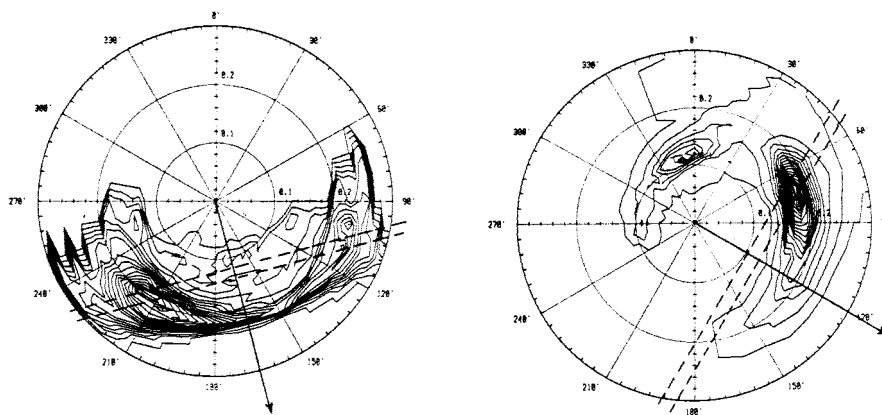
Figure 18   Contour plot of directional wave spectra. The radial coordinate is frequency in Hz, and the arrow indicates the wind direction (from Long et al. 1994).
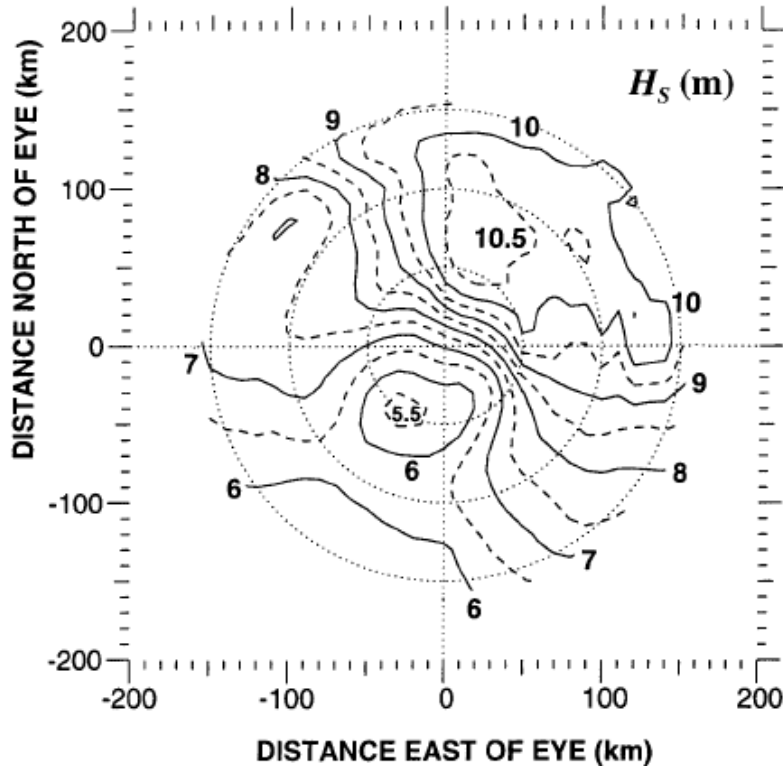
Figure 19   Spatial distribution of significant wave height (H_s) measured by the SRA during Hurricane Bonnie on 24 August 1998. At that time, Hurricane Bonnie is moving northward (from Wright et al. 2001).
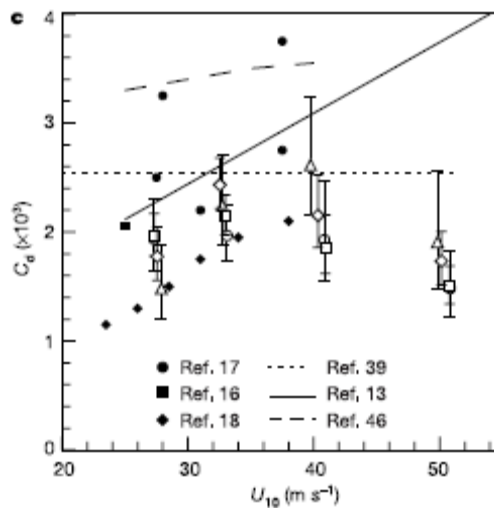
Figure 20   Relationship of drag coefficient (C_d) and sea surface wind speed (U_{10}) under extreme conditions. Different symbols indicated the C_d derived from different formulas (from Powell et al. 2003).
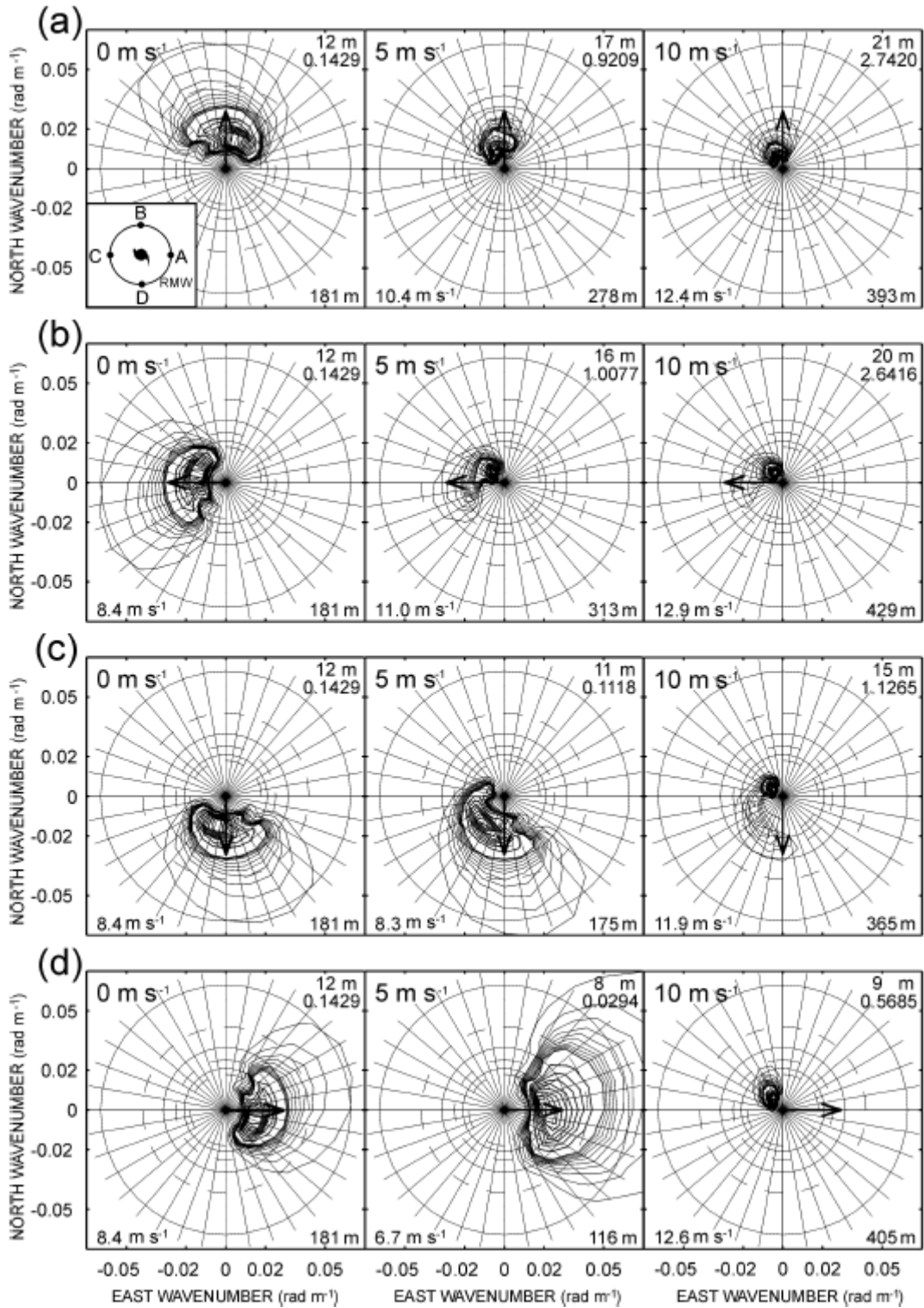
Figure 21　Directional wave spectra under idealized hurricanes case with different HTS. Locations are at R_m away from the storm center in directions, (a) East, (b) North, (c) West, and (d) South, respectively (from Moon et al. 2004a).
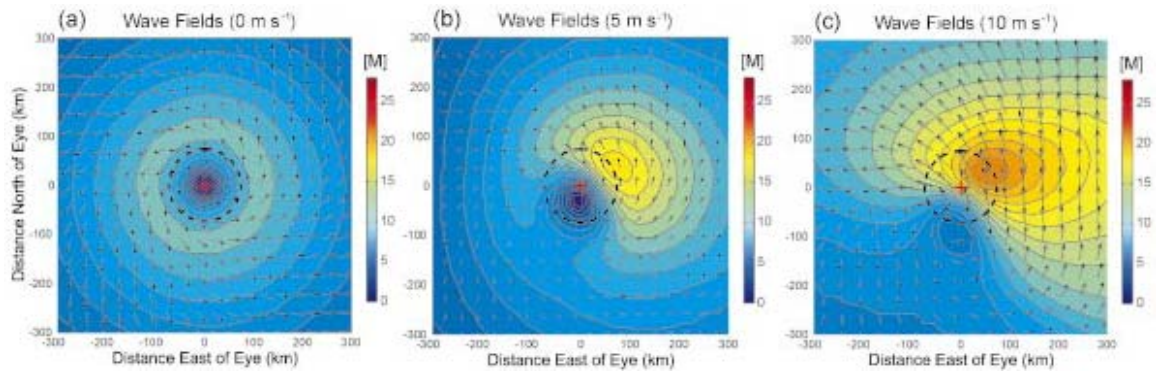
Figure 22   Spatial distributions of significant wave height (H_s) under various HTS. Arrows
indicate the local mean wave direction (from Moon et al. 2004a).
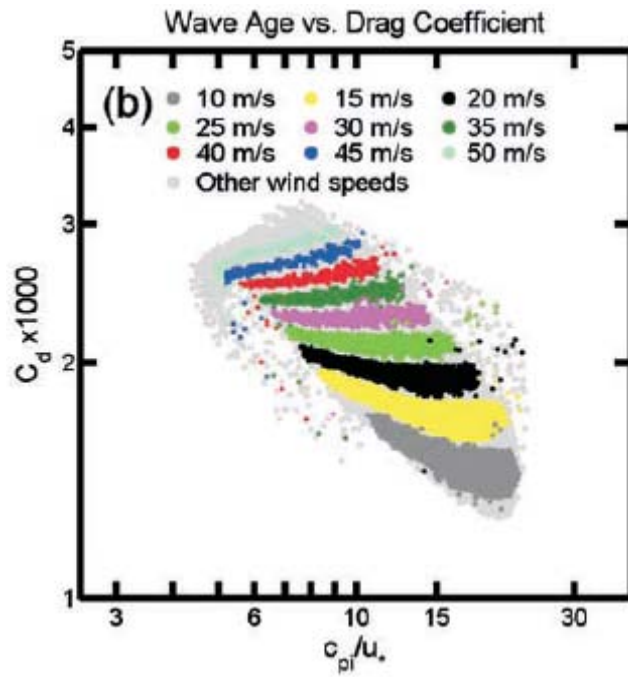
Figure 23   Scatter plot of C_d with various wave age and wind speed. C_d is plotted with
different colors according to wind speed intervals (from Moon et al. 2004b).

THIS PAGE INTENTIONALLY LEFT BLANK

VII. SCS WAVE CHARACTERISTICS DURING TY MUFIA

The WW3 model simulation of the SCS waves is performed under three scenarios. First, the QTCWPM wind field of Typhoon Muifa (2004), as mentioned earlier, is used to drive the WW3 model for the SCS. The WW3 result is evaluated with the significant wave height measured by the TOPEX/Poseidon satellite. Second, the ideal typhoon wind field is also applied to simulate the ideal typhoon-generated waves in the SCS. Third, the same ideal typhoon wind field with a uniform water depth is run in WW3 to examine the topography effect. The wave characteristics in the SCS is analyzed and discussed by the significant wave height and directional wave spectra.

A.   WW3 MODEL VALIFICATION DURING TY MUIFA

1.   Model Setting and Calculation

This study uses a relatively high resolution setting for the WW3 model (Wittmann 2001; Tolman et al. 2002). The spatial grid resolution is $1/4° \times 1/4°$ in the SCS of latitude from $0°$ to $25°N$, and longitude from $105°E$ to $122°E$. The discretization of energy spectra is in 24 directions with $15°$ grid spacing, and in 25 frequencies with logarithmic increment from 0.0418 to 0.3058 Hz. Two values are used in the WW3 time steps for computational efficiency. The global time step, the spatial time step, and the spectral time step are all set to 300 second, for entire solution propagation, spatial propagation, and intra-spectral propagation, respectively. The source time step for the source term integration is set to 100 second.

The QUICKEST with ULTIMATE propagation scheme is used here. As previously discussed, four source term components are Tolman and Chalikov (1996) wind-wave interaction term and dissipation term, the DIA nonlinear interaction term, and the JONSWAP bottom friction term, respectively. Other important model switch parameters are listed in Table 4. The WW3 model in this study is based on an available version, which has been implemented in the Naval Ocean Analysis and Prediction Laboratory (NOAP) (Chu et al. 2004).

The bathymetry data is from Terrain Base (Figure 24), which is the best available public domain global model of terrain and bathymetry on a $1/12° \times 1/12°$ grid. This

dataset, produced by the National Geophysical Data Center and World Data Center-A for Solid Earth Geophysics, is from twenty different sources, including the DCW-DEM and ETOPO5. The QTCWPM wind field is used as the input wind to run WW3 for the SCS. The WW3 model is run from 0000UTC 16 November to 1200UTC 25 November 2004. Since TY Muifa entered the SCS as late as 19 November, the model computation of the first three days, from 16 to 18 November, could be considered as the 'spin up' period of WW3 model.

2. TOPEX/Poseidon Satellite

Because of the lack of direct-measured platforms, such as vessels or buoys, during TY Muifa (2004) in the SCS, other sources of wind-wave measurement must be considered for evaluating WW3. Satellite remote sensing is an important field observation. For the remarkable performance of radar altimetry and for the data availability, the altimetry onboard the T/P satellite is applied in this study (Chu et al. 2004).

The T/P satellite, designed to map ocean surface topography, is jointly launched by NASA and the French Space Agency, *Centre National d'Etudes Spatiales* (CNES). The satellite first served in August 1992, and originally was planed for three-year prime mission, then expended for another six-year extension, totally for more than ten years. It carried a dual-frequency radar altimeter and was maneuvered in a circular orbit at an altitude of 1336 km with a 9.916-day repeat period (Martin 2004).

The T/P altimeter measurement data is also available online. The T/P dataset is provided by the Physical Oceanography Distributed Active Archive Center (PO.DAAC) of JPL. Data is in merged GDR format generation B, product number 068, and organized in on cycle header file with maximum 254 pass files. The T/P dataset includes altitude, altimeter range, and significant wave height (H_s) measurements from both Ku-band and C-band.

3. Result Evaluation

During the period of TY Muifa (2004), the temporal covered cycles are 448, which from 11 to 21 November, and 449, from 21 November and 01 December. There are 14 passes across the SCS area, which include 001, 012, 038, 051, 064, 077, 088, 114,

127, 140, 153, 164, 216, and 229. These passes have total 25 crossover points (see Figure 25) in the ocean region. On each point, the H_s from T/P measurement is accumulated to evaluate the H_s from WW3 computation.

The comparison between WW3 result and T/P observation is computed and performed as Figure 26. The total number of H_s pairs during the period of TY Muifa is 38. The scattering diagram (Figure 26a) shows the clustering of points approximately located around the equal line. The histogram of the differences between model and observation (Figure 26b) shows a Gaussian-type distribution. Examining the statistics, the bias of two datasets is 0.137 m with the root mean square error is 0.308 m, and the correlation coefficient is 0.895. The statistics suggests that the WW3 result and the T/P observation agreed well, and the numerical simulation during the period of TY Muifa is accurate and reasonable.

B.   NUMERICAL SIMULATION SCHEME

Previous studies has shown that the distance from the typhoon center, the hurricane (typhoon) intensity and the hurricane (typhoon) translation speed are the determinants of the typhoon-generated wave field (Walsh et al 1989; Wright et al. 2001; Moon et al. 2003). Several typhoon center locations are designed here to investigate the effects of typhoon intensity and of typhoon translation speed on the SCS wave characteristics. Furthermore, one set of ideal typhoon winds, and one set of uniform water depth are also used here to investigate the effects of winter monsoon and of the SCS topography.

1.   Typical Locations along the Typhoon Track

Since the intensity and the translation speed of TY Muifa are varied in time, four cases are designed here by fixed either variables. The typhoon passage could be reviewed in Chapter III (Figure 5). Figure 27 shows the translation speed and the intensity of TY Muifa (data from Table 2) along the typhoon passage. The water depth (data from Figure 24) of the typhoon center is also accompanied. The location of these designed typhoon centers is shown as Figure 28.

Along the track of the TY Muifa passage, the translation velocity, low pressure,

intensity, and bathymetry vary (Figure 27). Four locations along the TY passage are selected here for the discussions: Center-I (arriving the SCS), Center-II (strengthening and slowing), Center-III (weakening), and Center-IV (shelf breaking), respectively.

2. Designed Typhoon Centers

Center-I is chosen at ($11.9°N$, $117.2°E$). Just after TY entering the SCS for 24 hours, the typhoon center is located at Center-I at 0000UTC 21 November. The typhoon translation speed slightly decreased to 5.8 m/s. The typhoon low pressure was remained as low as 976 μPa with the maximum wind speed was 33.4 m/s. At this time, the estimated maximum wind radius (R_m) is 24.4 km. Center-I is for the typhoon arriving period.

Center-II is chosen at ($11.6°N$, $114.4°E$). TY Muifa reached the strongest intensity (i.e., the lowest central pressure, 954 μPa) at Center-II at 1800UTC 21 November. The maximum wind speed was 46.3 m/s, and R_m was 14.0 km. At that time, the typhoon translation speed slowed down to 4.2 m/s. Center-II is for the maximum typhoon intensity period.

Center-III is chosen at ($10.5°N$, $112.1°E$). TY Muifa had the same intensity at Center-III at 1800UTC 22 November as at Center-I at 0000UTC 21 November. The typhoon translation speed is notably slower at Center-III (3.0 m/s) than at Center-I (5.8 m/s). The maximum velocity radius is slightly larger at Center-III (R_m 28.6 km) than at Center-I (R_m 24.4 km). Other conditions are the same at Center-III (minimum pressure 976 μPa, maximum wind speed 33.4 m/s) as at Center-I. Center-III is for the typhoon weakening period. Comparison between Center-I and Center-III leads to the effect of the typhoon translation speed.

Center-IV is chosen at ($8.8°N$, $108.8°E$). TY Muifa was close to the Asian landmass at 0600UTC 24 November. The water depth is about 116 m. The low pressure was 987 μPa, and the maximum wind speed was 25.7 m/s with R_m 40.4 km. The typhoon intensity is much weaker at Center-IV than at Center-II. Center-IV is selected for the typhoon departure period.

C. EFFECTS OF TYPHOON WINDS

1. Significant Wave Height

Figure 29 shows the daily evolution of significant wave height (H_s) in the SCS during the passage of TY Muifa. The color scale symbolizes the value of H_s, from blue (0 m) to red (16 m). Here, the upper panels (Figure 29a-c) are for the period before TY Muifa entering the SCS; the middle panels (Figure 29d-f) are for the period during TY Muifa passing through the SCS; and the lower panels (Figure 29g-i)are for the period after TY moving out from the SCS.

Comparing to the evolution of QTCWPM wind field (Figure 11), it is found that the distribution of H_s follows the moving TY Muifa. High H_s is with high wind speed and high waves appear to the right of the typhoon passage. The maximum H_s (16 m) occurs as TY Muifa reaches its lowest pressure in the SCS on 21 November.

Another high H_s occurs in east of Luzon on 24 and 25 November (Figure 29h-i). Comparison between upper and lower panels of Figure 30 clearly shows the difference in monsoon-generated waves before TY Muifa arrival (Figure 29a-c) and after TY Muifa departure (Figure 29g-i). This indicates that the existing typhoon-generated wave field may affect the generation of new wind-wave field.

Figure 30a shows the horizontal distributions of WW3 generated maximum H_s and maximum wind speed during TY Muifa passage from 17 to 25 November. The core of the maximum wind speed is symmetric along the track of the TY Muifa passage (Figure 31b). However, the core of the maximum H_s is asymmetric in width and in value along the track of TY Muifa (Figure 30a) with higher H_s in the right side of the track than the left side.

TY Muifa has its lowest pressure at Center-II ($11.6°N$, $114.4°E$) at 1800UTC 21 November. Figure 31 shows the horizontal distribution of H_s at Center-II with the typhoon translation axis being rotated towards north. The radius of the maximum wind (R_m) is 14.0 km. The high values of H_s are in the right forward quadrant with the

maximum H_s of 16 m slightly outside of R_m from the typhoon center. This consists with earlier studies (Moon et al. 2003) that the wave generation on the typhoon center has an asymmetric distribution in four quadrants.

2.   Directional Wave Spectra at Center-II

Figure 32 shows the daily evolution of directional wave spectra at Center-II. The arrow indicates the wind speed and direction at each moment. The winds (7.8 m/s) blow from northeast (45° from the north) before 1800UTC 20 November and after 1800UTC 23 November, showing the winter monsoon dominates. In these two periods, a set of low-frequency waves exists and aligns with the wind in a slight angle leftward. Conversely, from 1800UTC 20 November to 1800UTC 23 November, rapid change of waves in both direction and frequency is found. Furthermore, after the departure of TY Muifa, evident wave packet still remains in the direction from 30° to 70°.

To investigate variation of the directional wave spectra during TY Muifa passage, the 6-hourly spectral evolution is presented (Figure 33) from 1800UTC 20 November to 1800UTC 22 November. It is seen that, while the wind is increasing and turning counterclockwise as TY Muifa passing by, the waves are generated along with the turning wind directions. As the typhoon located right on Center-II at 1800UTC 21 November, the wind speed significantly decreases and the wind vector shifts to the opposite direction. A wide range of waves are generated with monsoon dominated swell in the southwestward direction, and that, as typhoon wind changes rapidly in speed and direction, a pair of wave packets are generated at the time of typhoon arrival (Figure 33e). These typhoon-generated waves, especially in the opposite direction to monsoon winds (i.e., the northeastward direction) decay fast but still exist four days after the typhoon departure.

Four-way locations are selected around each center with the maximum wind radius (R_m) away to investigate the effect of translation speed on the directional wave spectra,: (1) forward location (F), (2) backward location (B), (3) rightward location (R), and (4) leftward location (L) (see up-left panel of Figure 35 to Figure 38). The typhoon center is indicated by 'C'. The dashed curves are circles with radius R_m from the typhoon centers. The hollow arrow indicates the typhoon's translation velocity vector.

The solid arrow is the wind vector at each location. Consistent with the previous study (Moon et al. 2003), the wave spectra in the forward and rightward directions show that high-frequency waves are generated aligning the wind direction due to resonant effects. But the wave spectra in the leftward and backward directions have a complicated structure.

3.   Effect of Typhoon Translation Speed

Figure 34 shows the 6-hour evolutions of H_s at the typhoon center for all four points. In order to investigate the effect of typhoon translation speed, all the H_s fields have bee rotated with the typhoon translation axis pointing toward north. Comparison of the H_s fields between Center-I and Center-III leads to the effects of typhoon translation on the wave characteristics. The maximum H_s is moving faster at Center-I than at Center-III. The value of maximum H_s at Center-I increases as the typhoon low pressure decreases. It is found that the highest H_s is located slightly outside R_m away from the typhoon center in the right forward quadrant, and that, the higher typhoon translation speed the larger angle between the highest H_s and the eastward direction is.

For the same typhoon intensity (Center-I and Center-III), the directional wave spectra at the typhoon center (location-C) is more asymmetrical for the faster translation speed (Figure 35C) than for the slower translation speed (Figure 37C). High wave energy centers occur in both frontward and backward directions for the slower translation speed.

4.   Effect of Typhoon Intensity

Typhoon has the same translation speed but different intensity at Center-II and Center-IV. Comparison of H_s and directional wave spectra between Center-II and Center-IV leads to the effect of typhoon intensity. Figure 34 shows that the maximum H_s is at least 5 m larger and located closer to the typhoon center at Center-II than at Center-IV. This is because the typhoon is stronger with smaller R_m at Center-II than at Center-IV. As the typhoon translation speed increases significantly at Center-IV (7.29 m/s), the shape of H_s contours becomes elliptic.

The directional wave spectra at the typhoon center clearly show the following features. The waves are generated in both frontward and backward directions for higher typhoon intensity (Center-II, Figure 36C), but only in the frontward direction for lower typhoon intensity (Center-IV, Figure 38C). Among the four locations around the typhoon center, the directional wave spectra are very different at locations (F, R, and L) but less different at location B between Center-II and Center-IV. At locations (F, R, and L), two wave packets are generated in both upwind and downwind directions for high typhoon intensity (Figure 36), but only one wave packet is generated in downwind direction for low typhoon intensity (Figure 38). The difference between Center-II and Center-IV (comparing Figure 36 with Figure 38) is much larger than the difference between Center-I and Center-III (comparing Figure 35 with Figure 37). This indicates that the effect of typhoon intensity is much larger than the effect of typhoon translation speed on the SCS wave characteristics.

D.   EFFECTS OF MONSOON WINDS

When the ideal typhoon winds during TY Muifa passage through the SCS are used as the wind input for WW3, the effect of background winds (winter monsoon) is not included. Difference between two simulations described in this and previous sections is considered the effect due to the monsoon forcing.

1.   Significant Wave Height

Figure 39 shows the daily evolution of significant wave height (H_s) in the SCS during the passage of TY Muifa. Similar to Figure 29, Figure 39a-c are for the period before TY Muifa entering the SCS; Figure 39d-f are for the period during TY Muifa passing through the SCS; and Figure 39g-i are for the period after TY moving out from the SCS.

Comparing Figure 39 to Figure 29, it is found that the horizontal distribution of H_s is quite similar between using the ideal typhoon winds (Figure 39) and the QTCWPM winds (Figure 29) near the typhoon center. But the maximum H_s using the ideal typhoon winds is 15 m and less than that (16 m) using QTCWPM winds. Using the ideal typhoon winds, the wave energy is generated near the typhoon center along the typhoon passage. After the departures of TY Muifa, the wave energy remains for one to

two days and then disperses along the typhoon passage. Wave energy propagates to the forward, the right-frontward, and the left-rearward directions. There is no high H_s area occurring east of Luzon from 24 to 25 November.

Figure 40 shows the horizontal distributions of WW3 generated maximum H_s (Figure 40a) and maximum wind speed (Figure 40b) during TY Muifa passage using the ideal winds from 17 to 25 November. Similar to the simulation using the QTCWPM winds (Figure 30), the core of the maximum wind speed is symmetric along the track of TY Muifa (Figure 40b). However, the core of the maximum H_s is asymmetric in width and in value along the track of TY Muifa (compared to Figure 40a) with higher H_s in the right side of the track than the left side.

Comparing Figure 40 with Figure 30, it is found that the monsoon wind does not affect H_s near the typhoon passage, but does affect H_s far from the typhoon track, especially in the northern SCS. In the maximum wave field, the maximum H_s field is generally higher with monsoon present, and significant difference is found in the west of Luzon.

Figure 41 shows mean differences of H_s and wind fields between the two simulations. The difference in wind fields is relatively small along the typhoon passage and relatively large away from the typhoon passage. It is close to the background mean wind (Figure 10). The maximum difference in H_s is located in the deep water area away from the coast. It indicates a fetch-limited case, which the higher waves produced farther from the coast by steady monsoon. The obstruction of shoreline and small islands is also seen on the wave propagation along the monsoon direction.

2. Directional Wave Spectra

Figure 42 shows the daily evolution of directional wave spectra at Center-II. The arrow indicates the wind speed and direction at each moment. Distinction between Figure 42 and Figure 32 is the swell generation (no swell generation) in the southwestward direction with QTCWPM (ideal typhoon) winds. This difference is due to the background monsoon winds.

To investigate the difference of the directional wave spectra between using QTCWPM and ideal typhoon winds during TY Muifa passage, a 6-hour spectral evolution is presented (Figure 43) from 1800UTC 20 November to 1800UTC 22 November. Comparing Figure 43 to Figure 33, it is found that the two directional wave spectra are almost the same during 0600UTC 21 November to 1200UTC 22 November when TY Muifa is around Center-II, but quite different for other time periods. Before TY Muifa arriving Center-II (1800UTC 21 November), there is high wave energy in the southwestward direction using the QTCWPM winds (Figure 33a) but none using the ideal typhoon winds (Figure 43a). One day after the typhoon moving out of Center-II, the typhoon-generated waves in swell direction dispersed, and the swell energy appeared again (see Figure 33). This suggests that the monsoon-generated swell does not decay and remain through the typhoon period.

Figure 44 shows the H_s distribution and directional wave spectra using the ideal typhoon winds on the typhoon position at Center-IV (water depth: 116 m). Figure 44 is almost the same as Figure 38, which indicates that even when the typhoon winds weaken, the typhoon generated waves still dominate.

E.   EFFECTS OF BOTTOM TOPOGRAPHY

A third WW3 simulation is conducted for the SCS with everything the same as Section 6 but the uniform water depth (2000 m, Figure 45). The surrounding islands, Taiwan, the Philippians Islands, Palawan, Borneo, and the Indonesia Islands, have been removed. Difference between the third and the second simulations leads to the effects of island obstruction and bottom topography on the wave characteristics.

1.   Significant Wave Height

Figure 46 shows the daily evolution of H_s simulated by WW3 with the ideal typhoon winds with uniform water depth. The effects of topography are examined by comparing Figure 46 to Figure 40 (realistic topography). The maximum H_s is about 15.5 m, a little larger than using the realistic topography (15 m). Similar feature is also found in the right-frontward direction of the typhoon center, expect the right-front quadrant has higher H_s value and wider distribution. As TY Muifa enters the SCS on 20 November, the typhoon-generated waves are well-developed due to no island obstruction.

The wave propagations in the right-rearward direction of the typhoon passage are similar, but in the uniform water depth simulation, it is much clear that the wave does propagate forward, and faster than the typhoon translation. Although there is no island blockage in the left-rearward direction, the wave propagations are still limited.

It is evident that along the typhoon passage, the typhoon generated waves more like to propagate in the right-backward and left-forward directions, and the right-forward and left-backward directions are restricted. This may be due to the momentum flux into the typhoon passage in the right-forward and left-backward quadrants.

Figure 47 shows the maximum values of the simulated waves, and the mean difference between normal water depth and the uniform water depth. Compared Figure 47a with Figure 40a, it is found that higher H_s appears from $119\degree E$ to $122\degree E$, and that, as TY Muifa close to the Asian landmass, the wave energy does not disperse due to no change in water depth, and disappear only when the waves contact coastline. The depth of the nearshore dispersion area is between 20 to 50 m.

This feature is exhibited better in the mean H_s difference between normal depth and uniform depth (Figure 47b). The color scale is from 0 m (blue) to 1.5 m (red). It shows that H_s from the uniform depth is developed better than from the real SCS topography, and the maximum difference is within 1.5 m. Large difference is seen along the typhoon passage while close to coastline. The notable difference is also seen in the Gulf of Thailand, around Palawan, and in the west water of Borneo. In the east water of Borneo, previous simulation suggests that no wave propagation into it, but in this uniform water simulation, the wave propagation is observed.

It is observed that the SCS wave does not propagate into the Sulu Sea due to the obstruction of Palawan and Borneo. Therefore, the Sulu Sea may be considered as a different wave system from the SCS, and the wave simulation of the Sulu Sea in this study may be underestimated. Compared the difference in the south-west SCS with the bathymetry contour of the SCS (Figure 24),the difference of 0.5 m does follow 100 m water depth properly.

2. Directional Wave Spectra

Figure 48 shows the daily evolution of directional wave spectra with the idealized typhoon winds and uniform water depth on the same location as Figure 32. Compared Figure 48 with Figure 32, it is seen that few wave energy reaches before the typhoon arrival, but after the typhoon departure, the wave spectra are identical. It may due to the wave energy does not disperse by the Philippians islands and propagate here before TY Muifa arrived.

Figure 49 shows the H_s distribution and directional wave spectra using the ideal typhoon winds and uniform water depth on the typhoon position at Center-IV. Comparing Figure 49 (uniform water depth) to Figure 44 (realistic topography, water depth: 116 m), it is found that the directional wave spectra and H_s are almost the same, which indicates that the topographic effect on the wave characteristics is not important when the local typhoon winds dominates with the water depth deeper than 100 m.
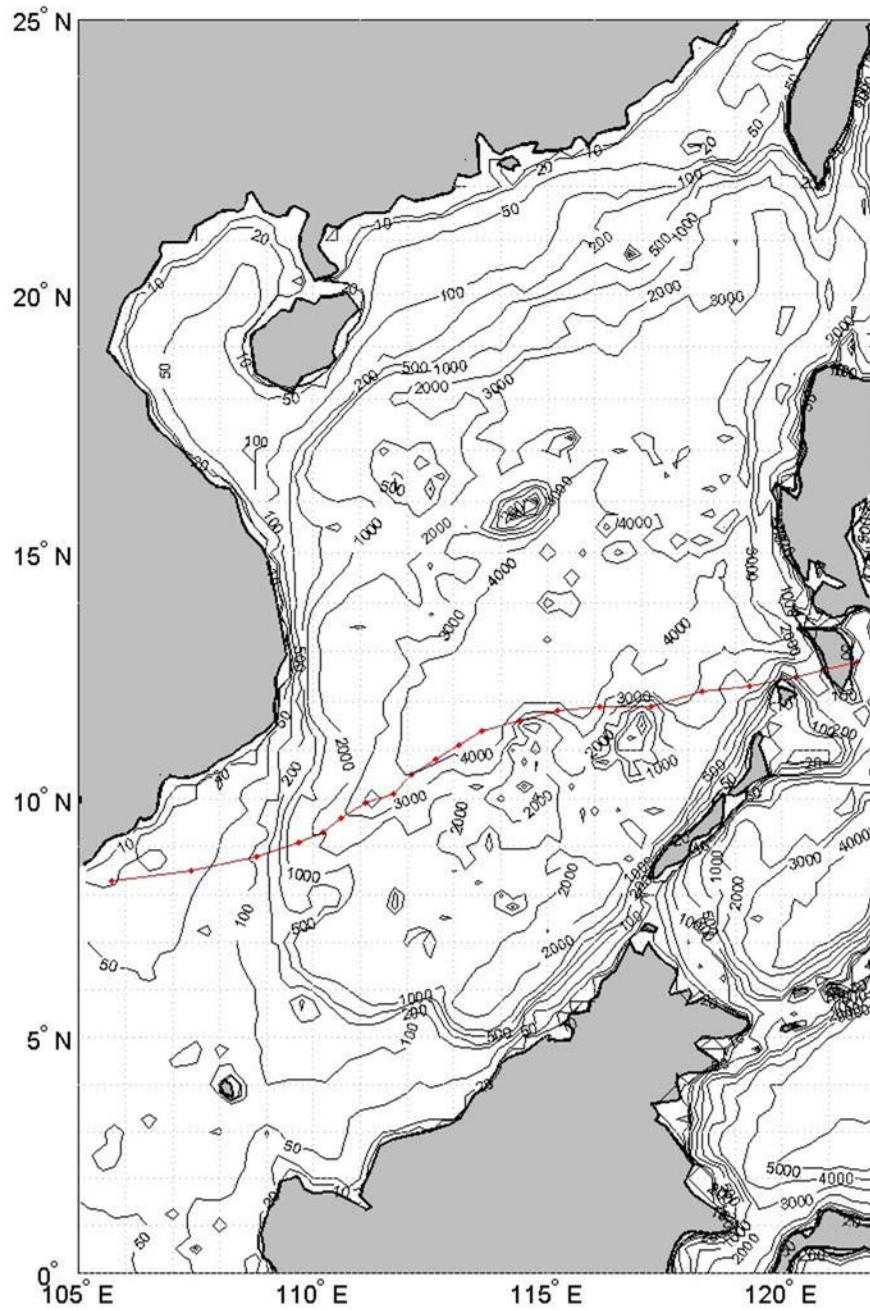
Figure 24   The SCS bathymetry from the TerrainBase dataset. Red line and points indicate the passage of TY Muifa (2004).
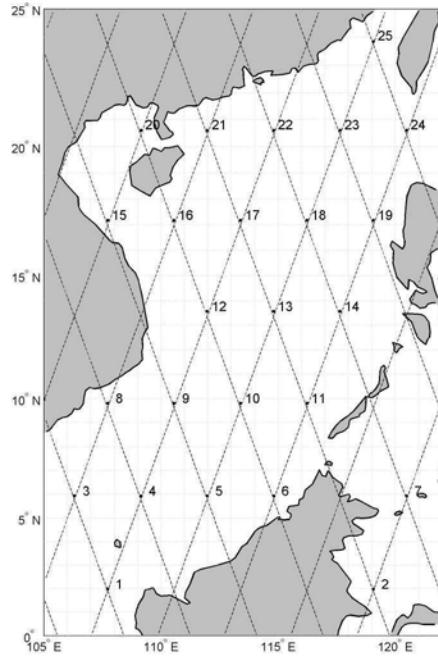
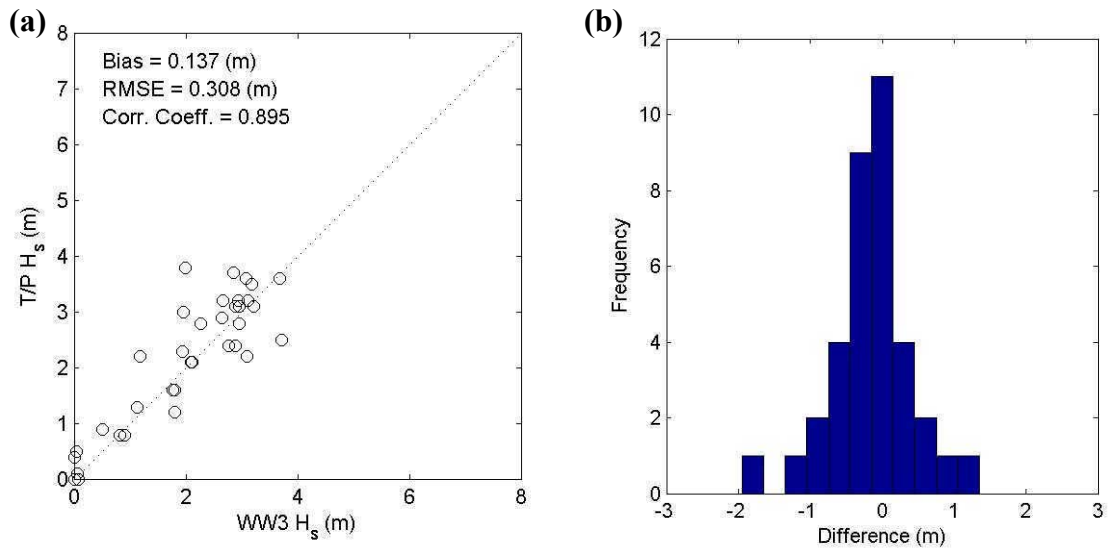Figure 25   TOPEX/Poseidon crossover points in the SCS.

Figure 26   WW3 result compared with TOPEX/Poseidon observations on all crossover
points during the period of TY Muifa (2004). (a) The paired data distribution, and
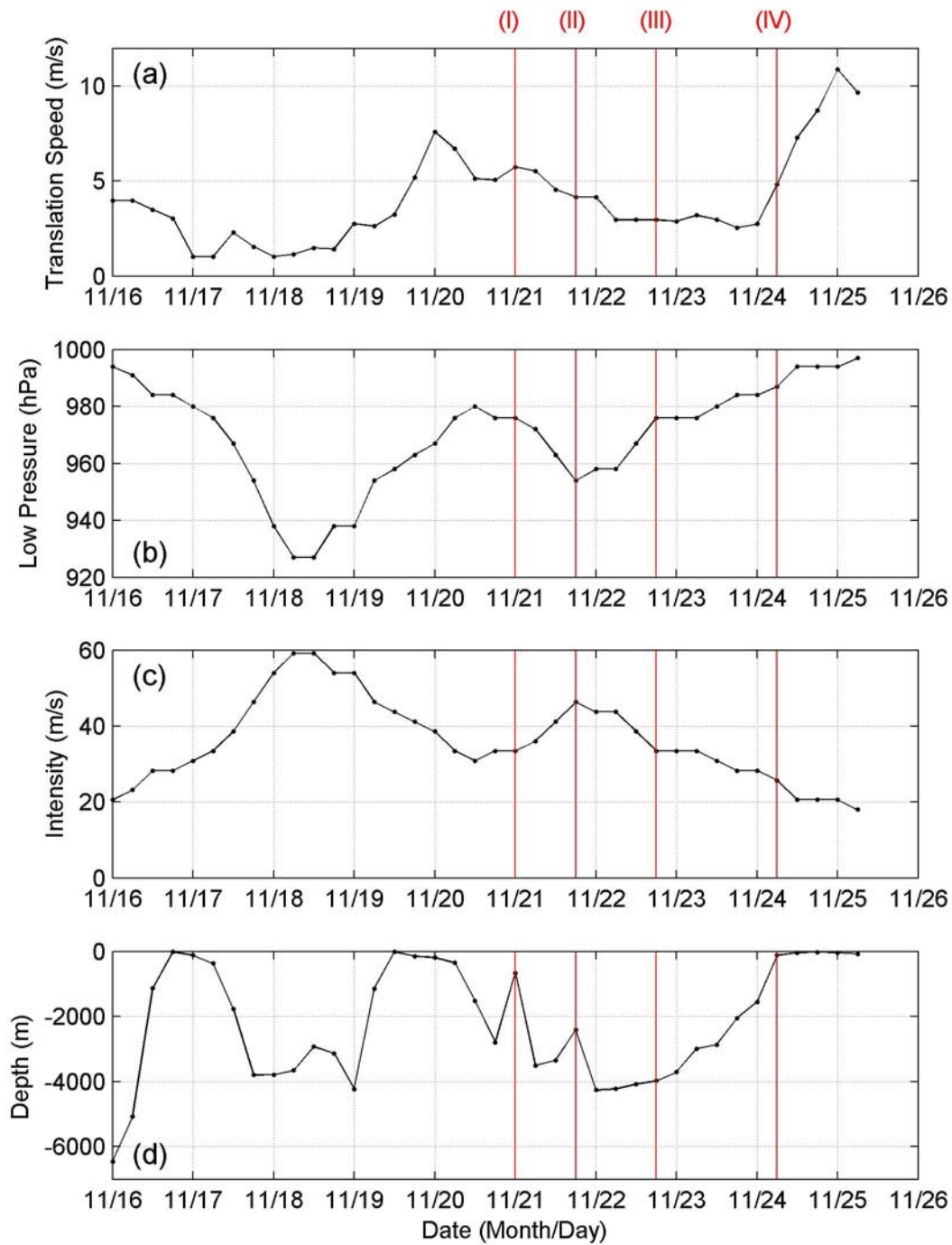(b) the histogram distribution of difference.

Figure 27　(a) The translation speed, (b) the lowest pressure, and (c) the maximum wind speed of TY Muifa (2004) with (d) the water depth along the typhoon passage. Red lines indicate four designed typhoon centers.
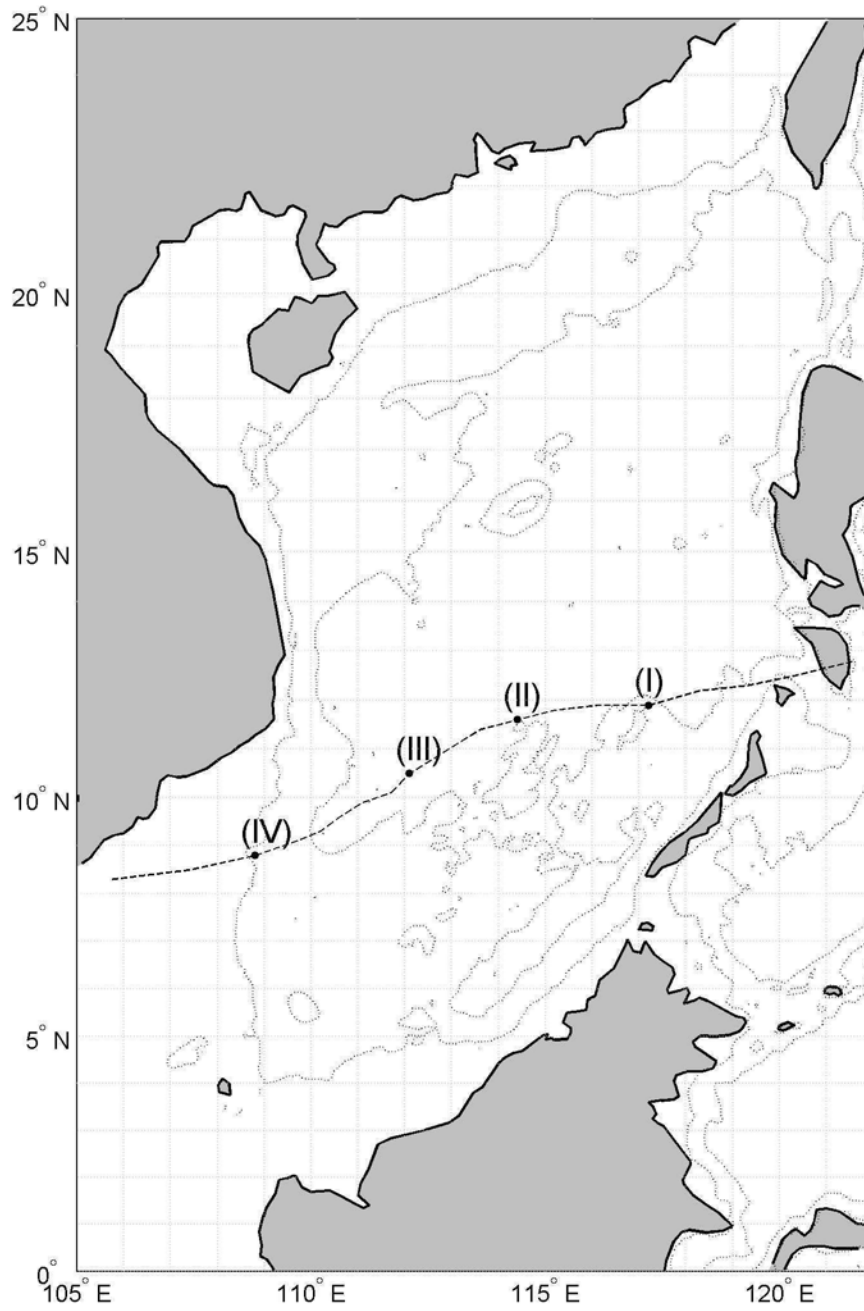
Figure 28   The locations of 4 designed typhoon centers. Dotted line indicates the water
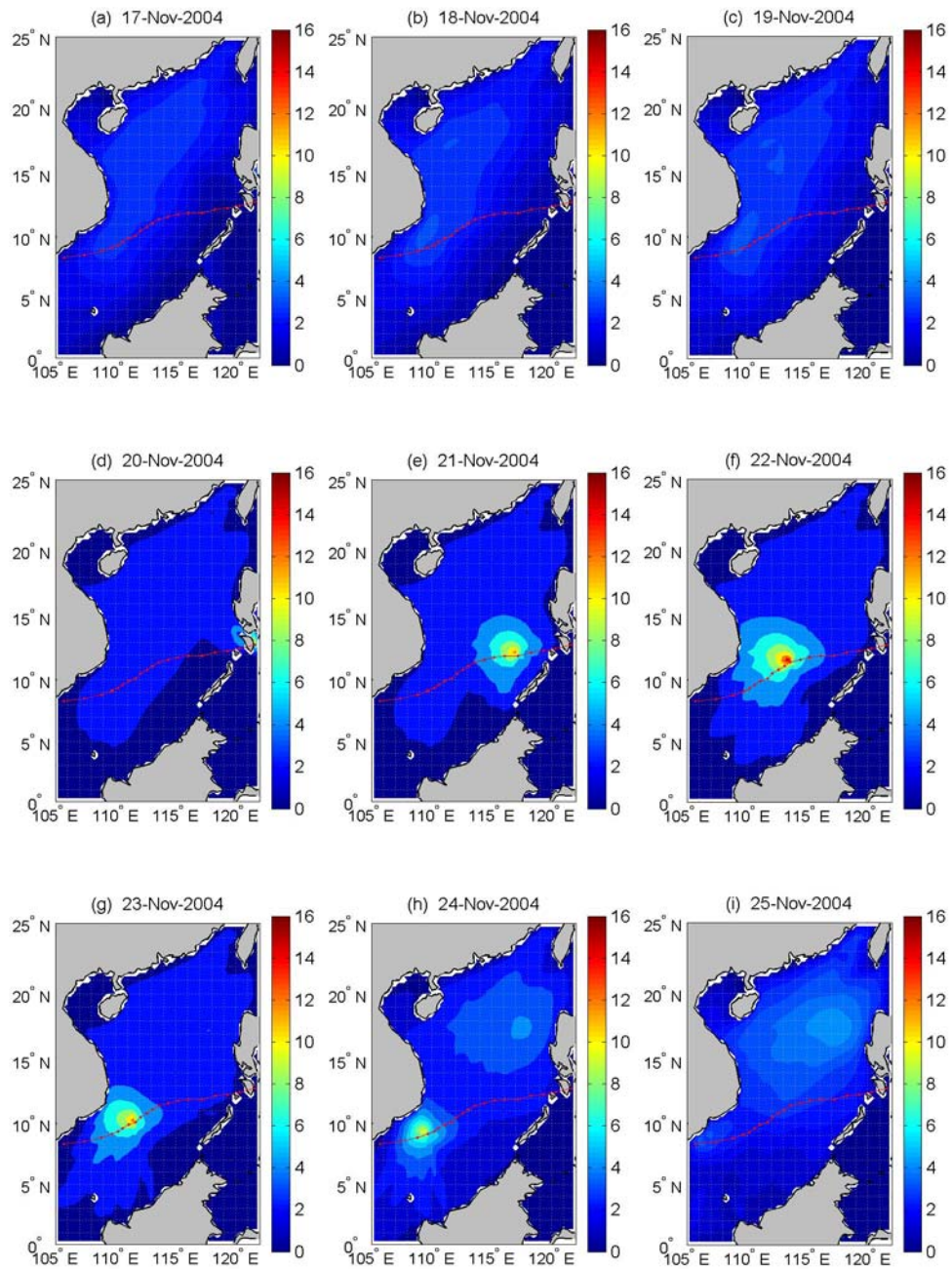depth of 100 m (near shore) and 2000 m (open ocean).

Figure 29   Daily evolution of H_s in the SCS during the period of TY Muifa (2004).
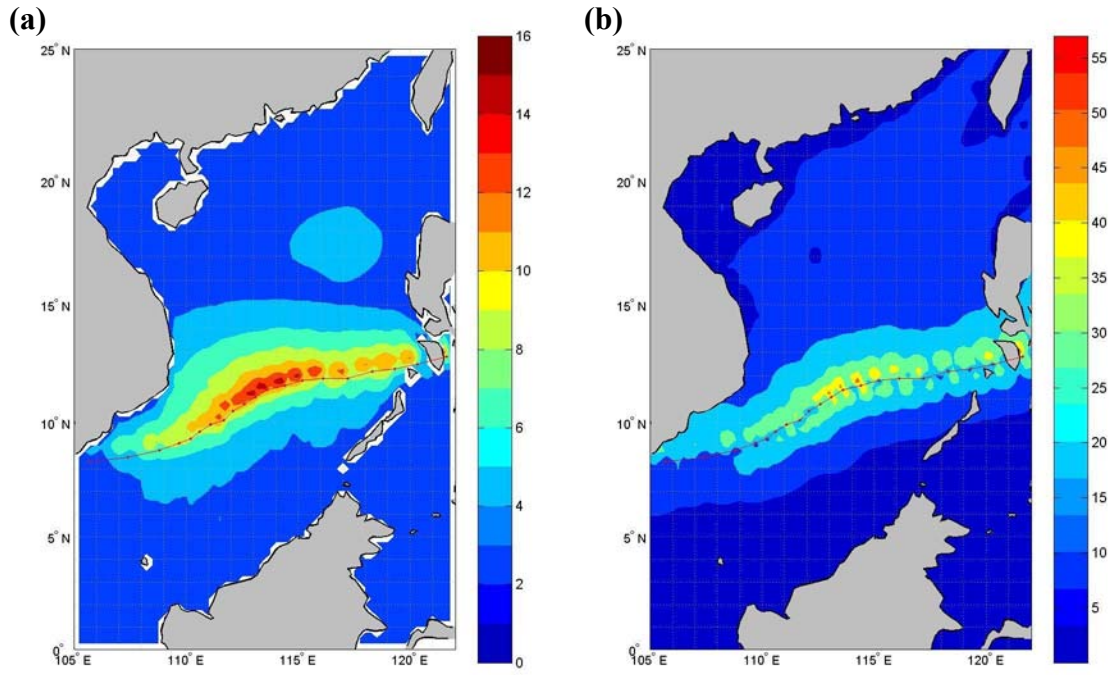
Figure 30   Total distribution of (a) the maximum H_s from WW3, and (b) the maximum QTCWPM wind speed during the passage of TY Muifa (2004).
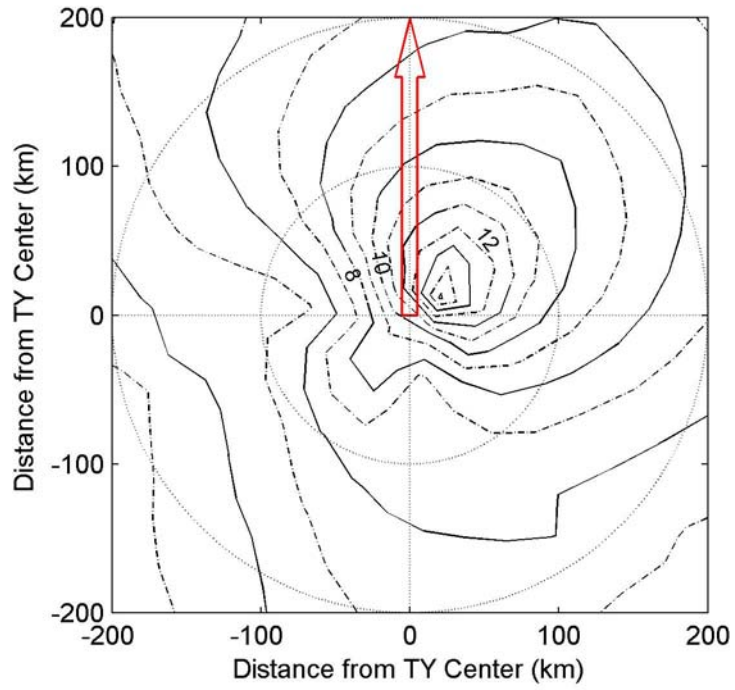
Figure 31 H_s of the lowest pressure center of TY Muifa in the SCS on $(11.6^\circ N, 114.4^\circ E)$
at 1800UT 21 November. The estimated maximum wind radius is about 14.0 km.
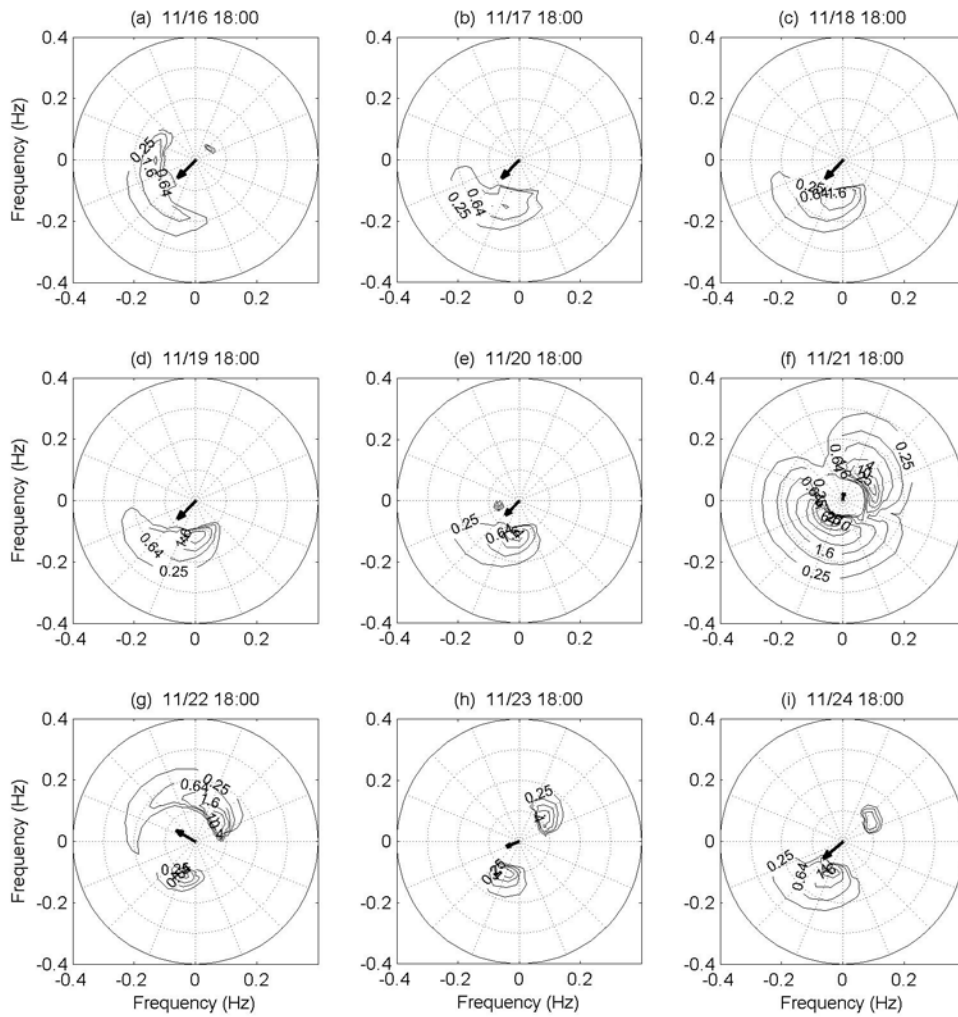The translation direction (hollow arrow) is rotated to northward.

Figure 32   Daily evolution of directional wave spectra with QTCWPM winds on designed
Center-II ($11.6\,^\circ N$ and $114.4\,^\circ E$). TY Muifa arrived this point at 1800UTC 21
November. The arrow presents QTCWPM wind speed and direction. The wind
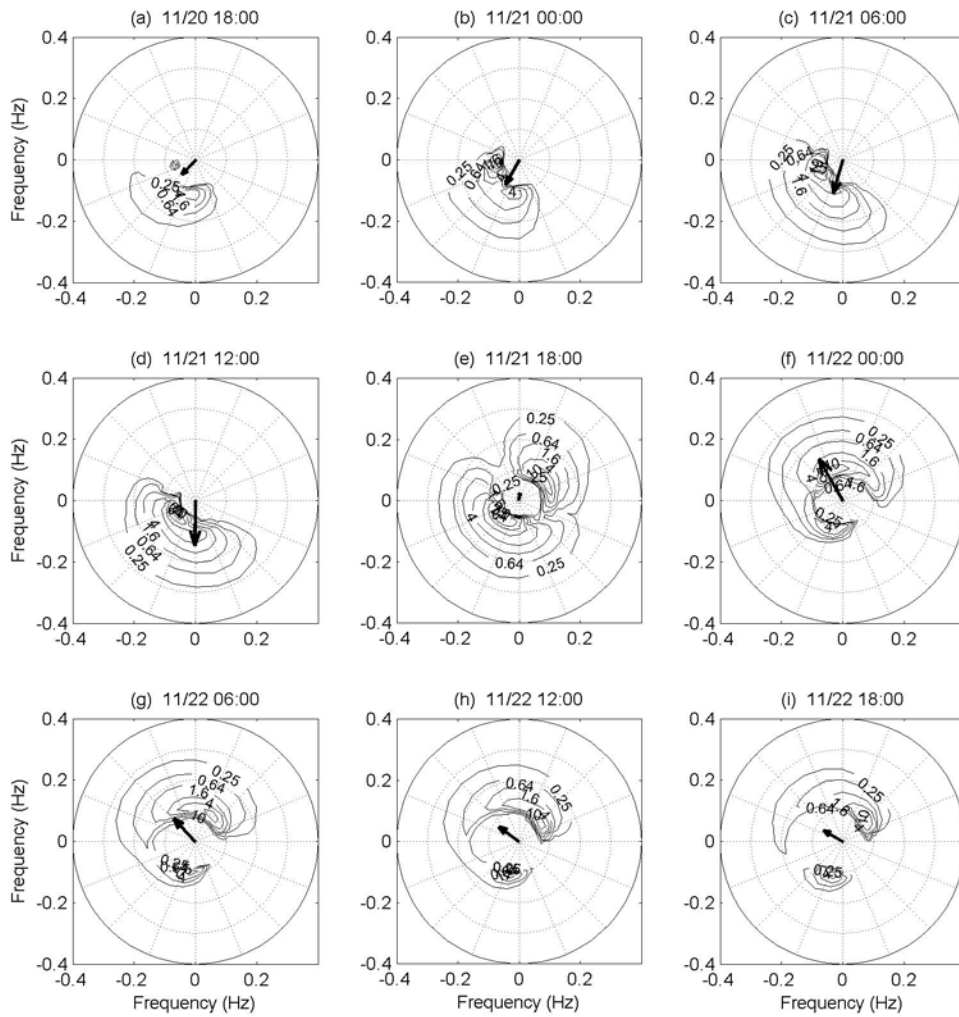speed value is 100 times of the axis scale.

Figure 33   Detail evolution of Figure 32 with time step 6 hours from 1800UTC 20 November to 1800UTC 21 November.
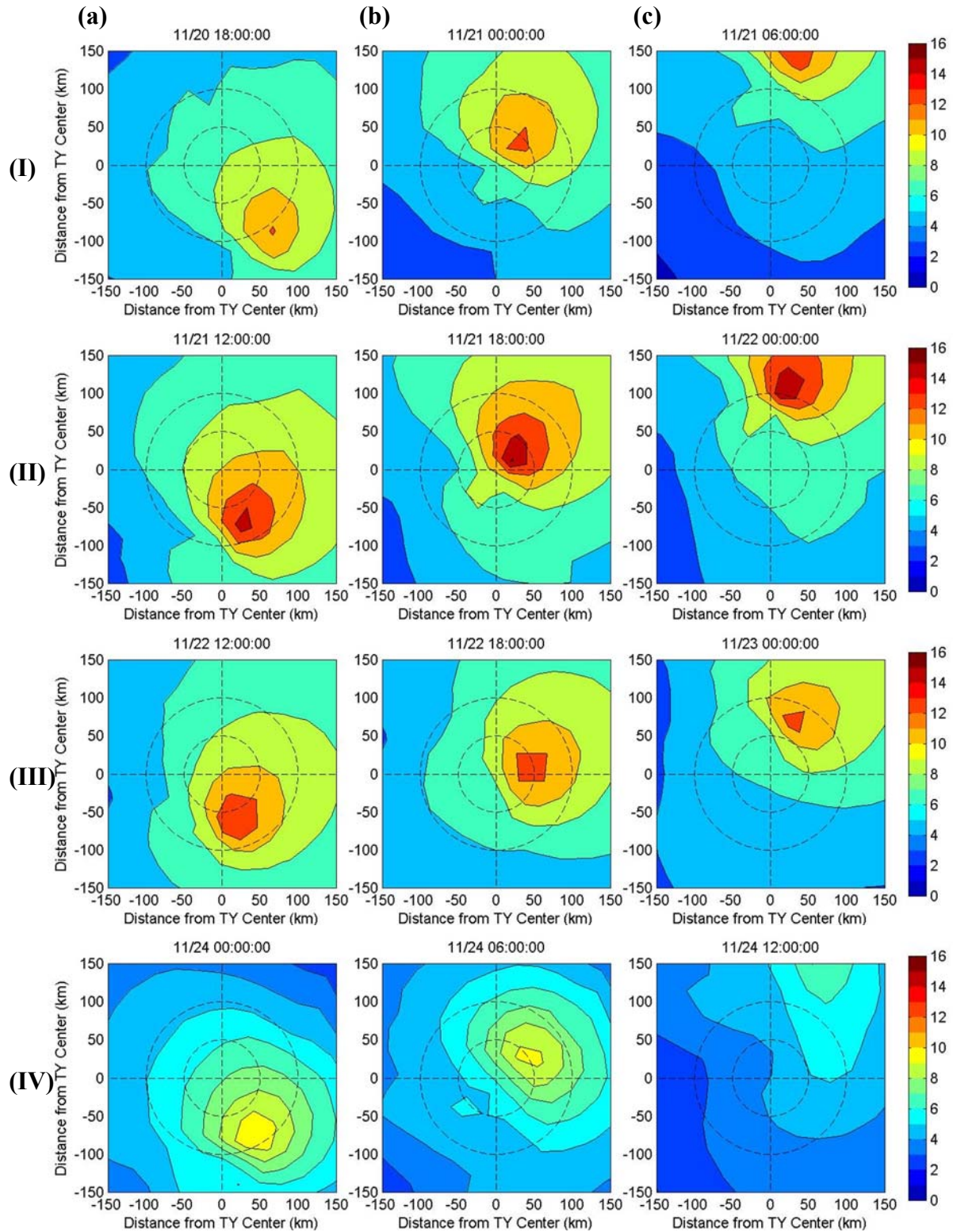
Figure 34   6-hour evolutions of H_s on four designed typhoon centers (a) before typhoon arrivals (left column), (b) typhoon right on centers (central), and (c) after typhoon departures (right). The translation directions are rotated to northward.

72

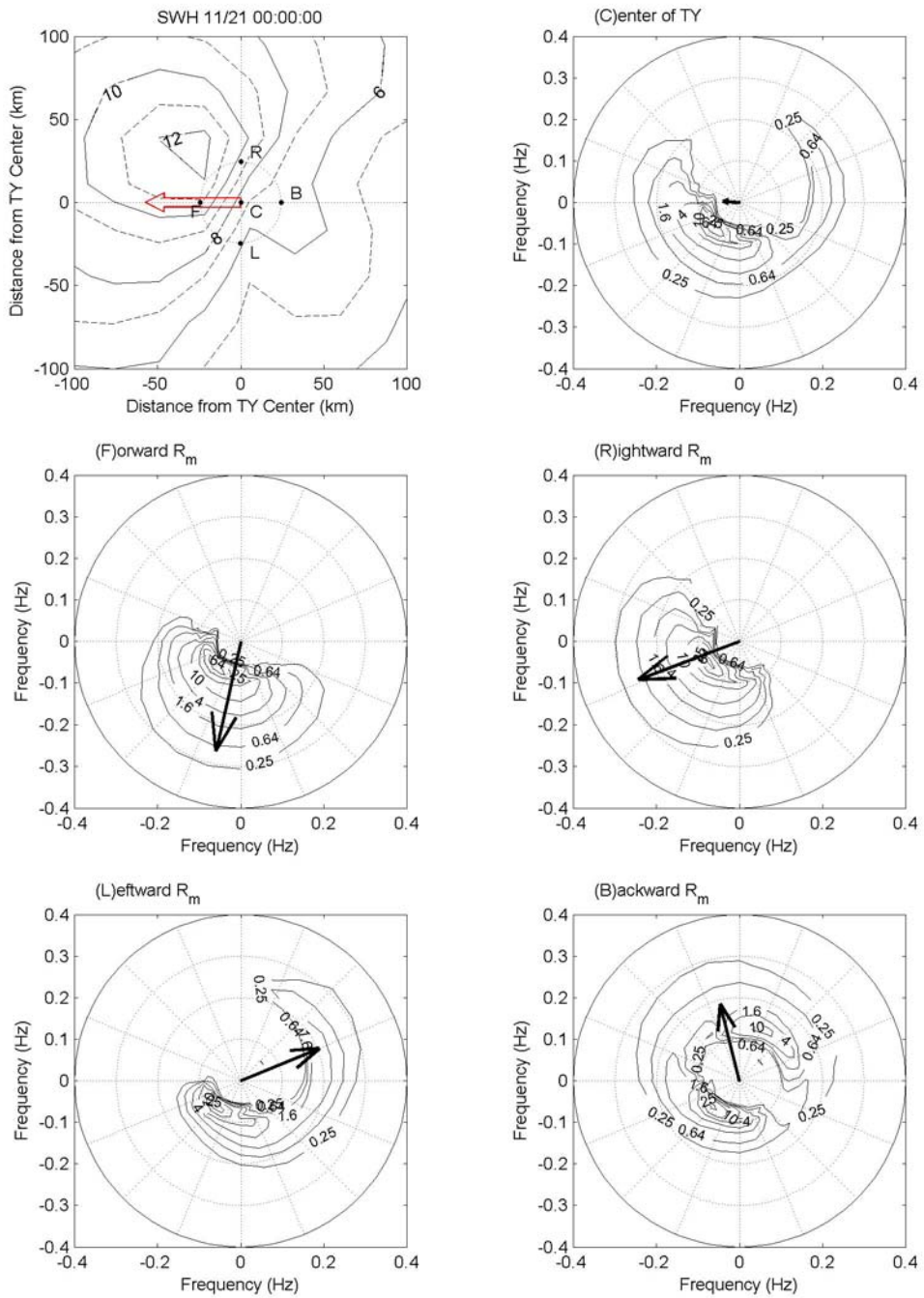Figure 35 H_s of Center-I (0000UTC 21 November, $11.9°N$ and $117.2°E$), and its central (C) and four-way (F, R, L, and B) directional wave spectra. The hollow arrow is the translation direction. The format of wave spectra is similar to Figure 32.
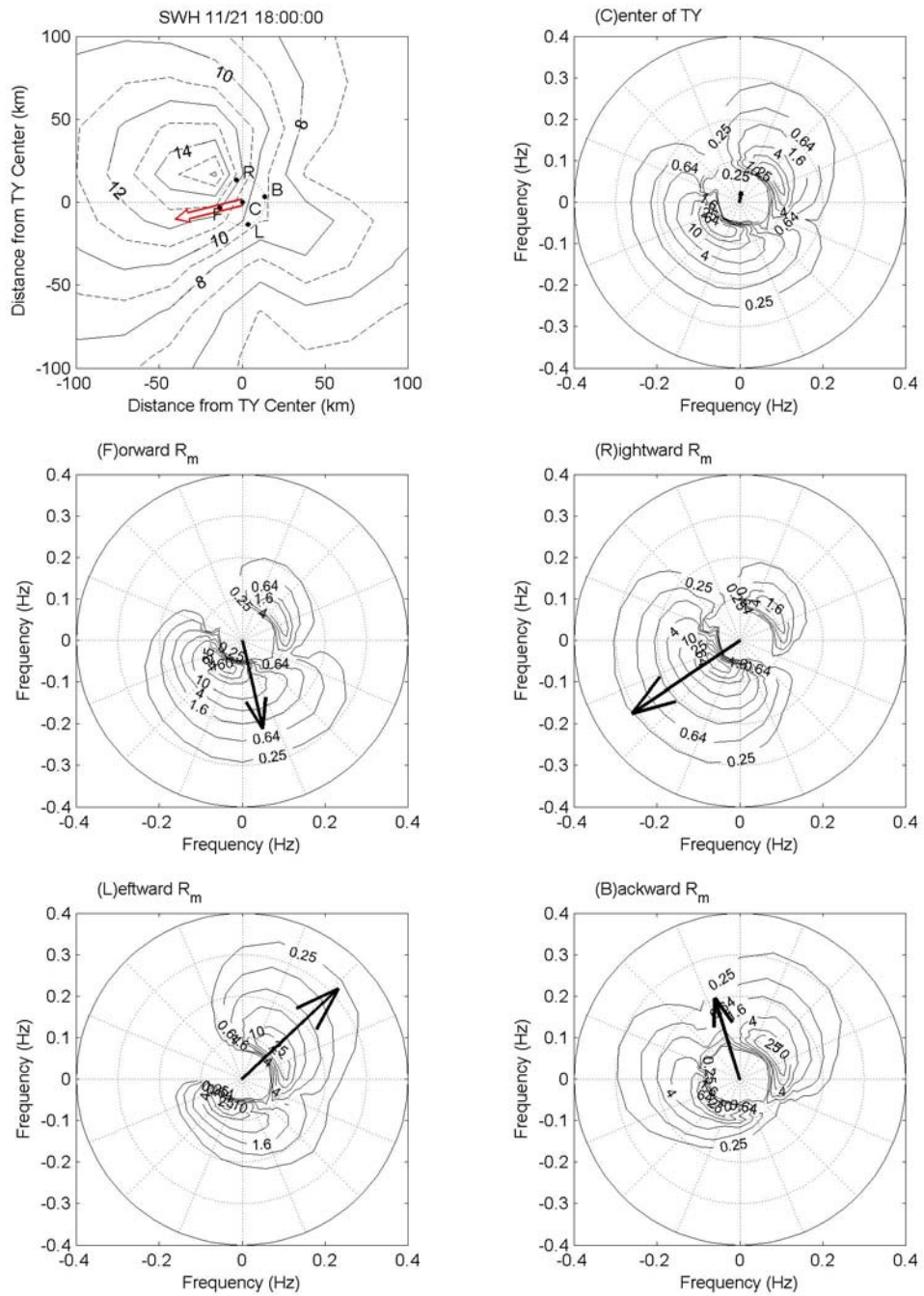
Figure 36 H_s, and central (C) and four-way (F, R, L, and B) directional wave spectra of Center-II (1800UTC 21 November, $11.6°N$ and $114.4°E$). Similar format as Figure 35.

Figure 37 H_s, and central (C) and four-way (F, R, L, and B) directional wave spectra of

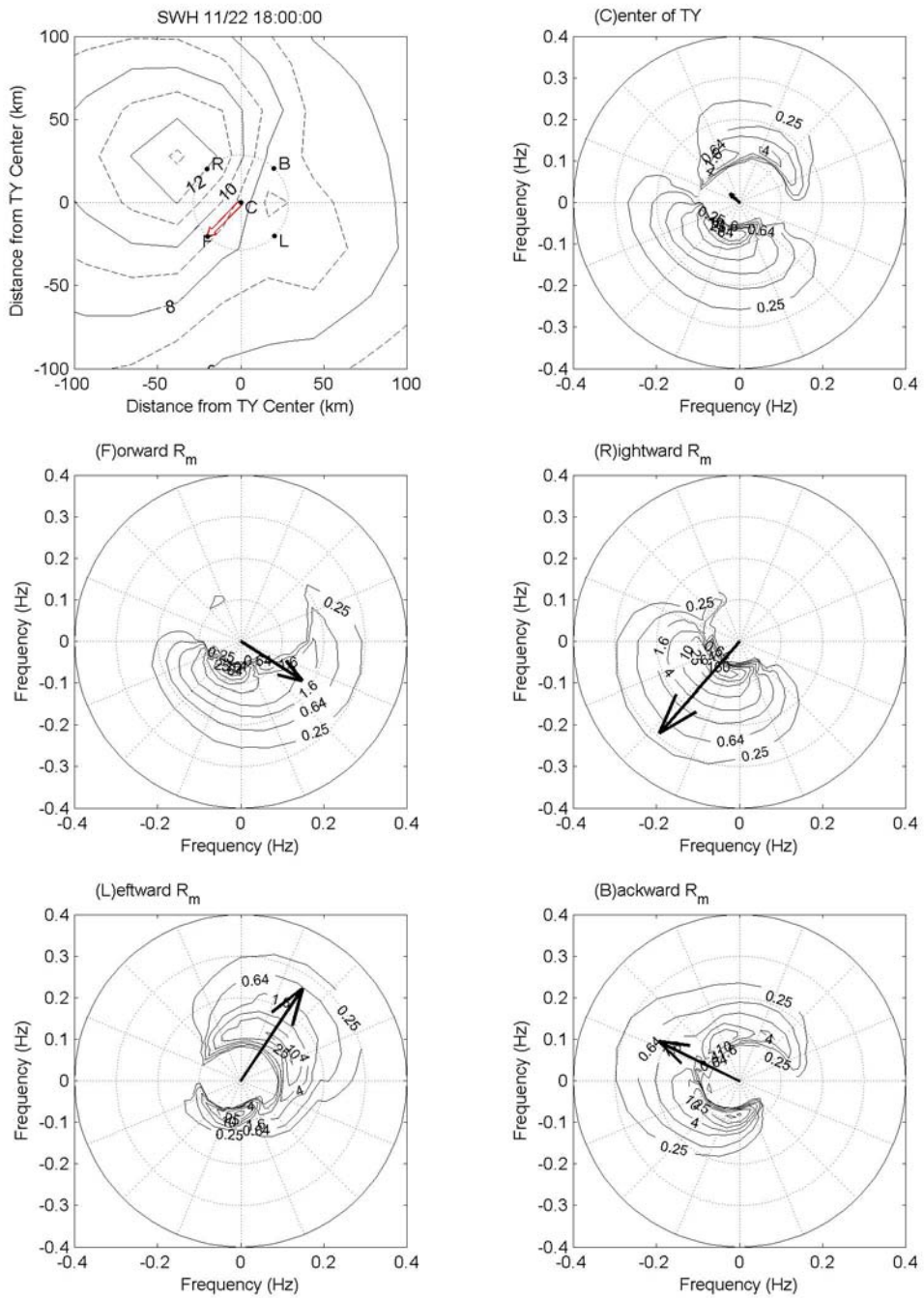Center-III (1800UTC 22 November, $10.5°N$ and $112.1°E$). Similar format as
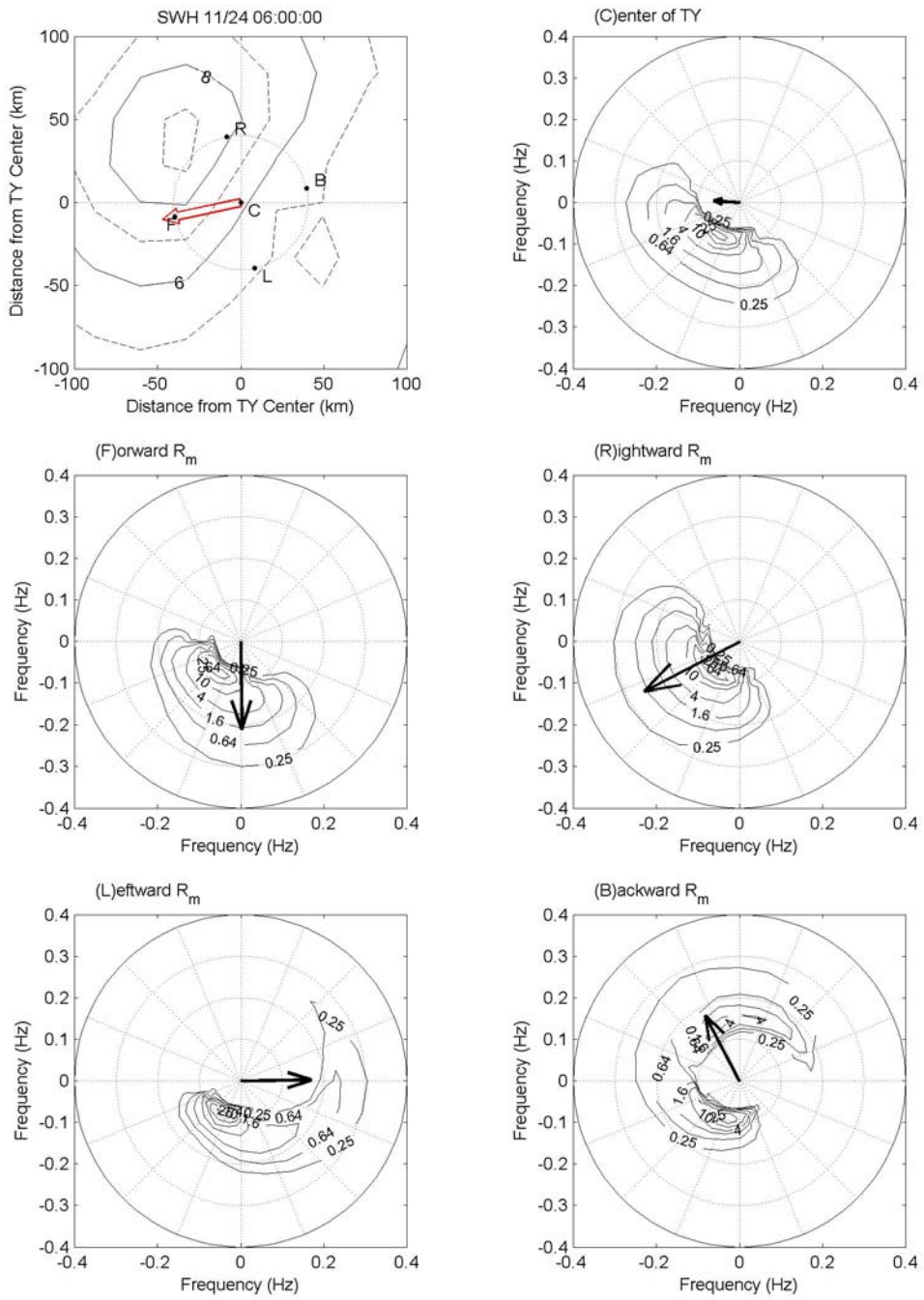
Figure 35.

Figure 38 H_s, and central (C) and four-way (F, R, L, and B) directional wave spectra of Center-IV (0600UTC 24 November, $8.8°N$ and $108.8°E$). Similar format as Figure 35.

76
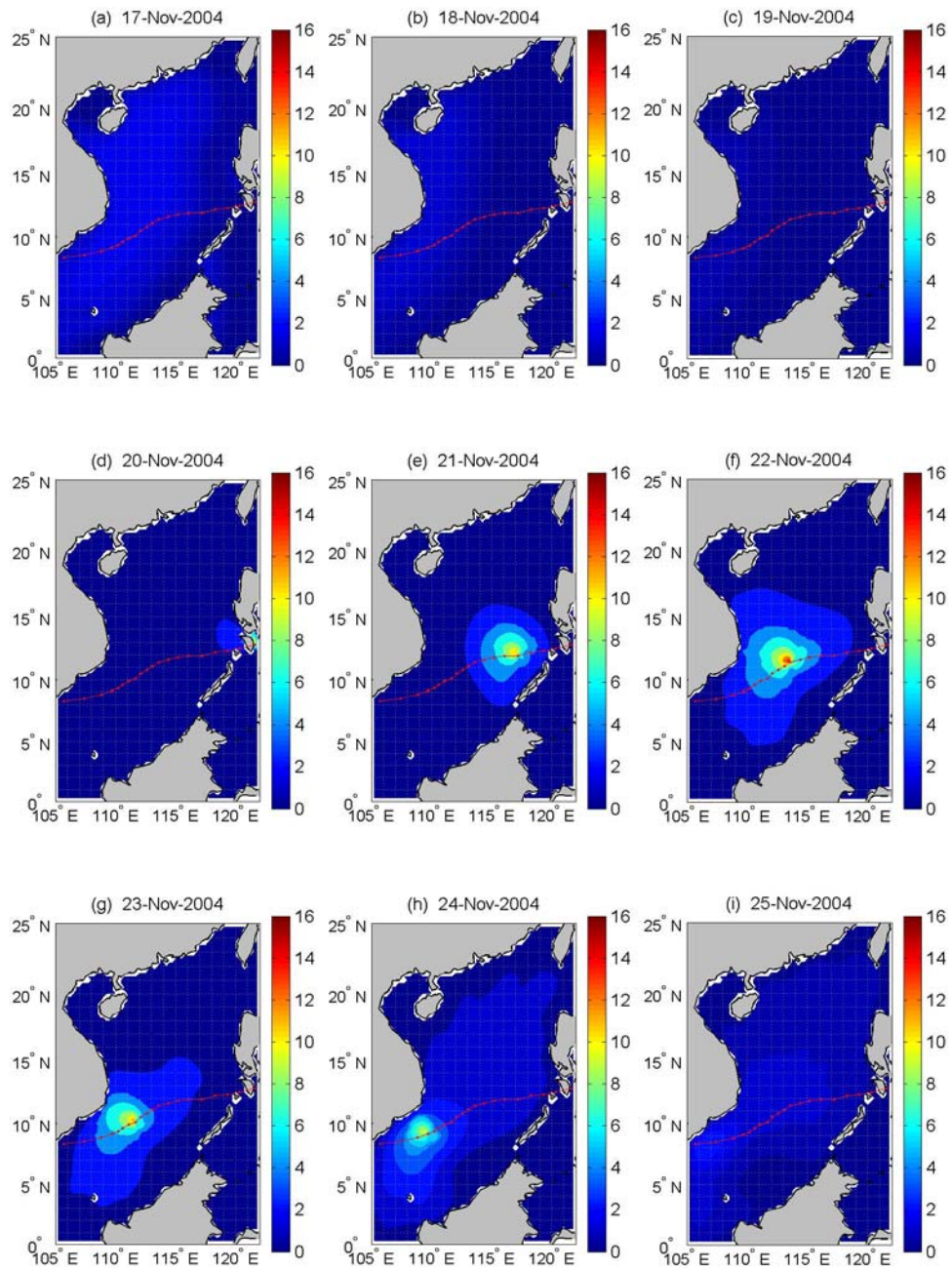
Figure 39   Daily evolution of H_s from ideal typhoon winds in the SCS during the period of TY Muifa (2004).
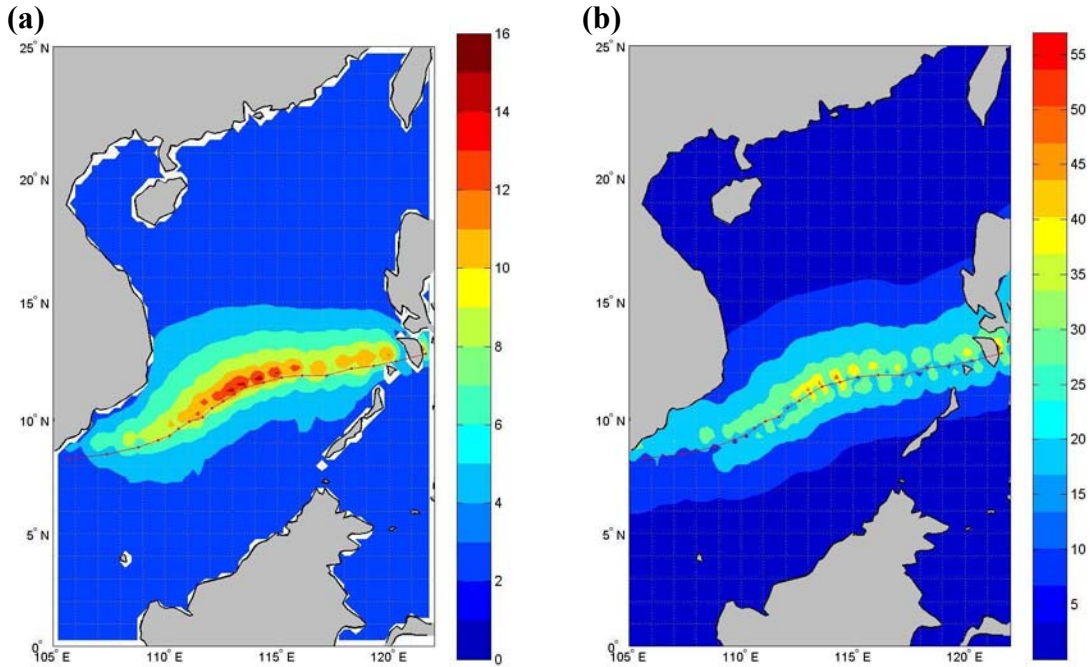
Figure 40   Total distribution of (a) the maximum H_s and (b) the maximum wind speed from ideal typhoon winds. Similar format as Figure 30.
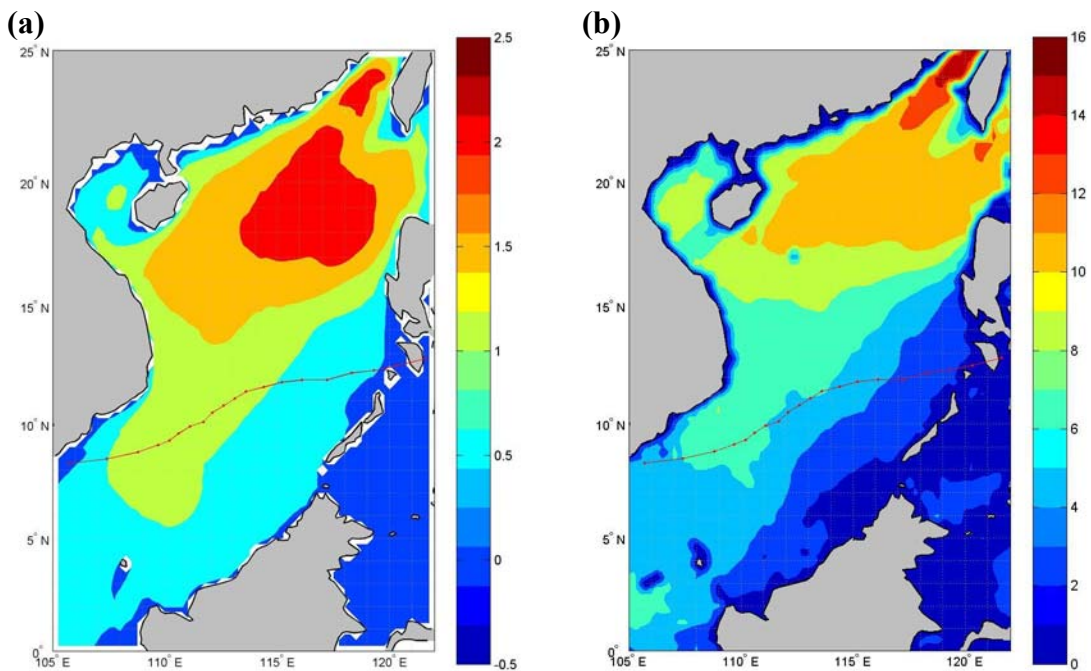
Figure 41   (a) The mean difference of H_s between Figure 29 and Figure 39, and (b) the mean difference of wind speed between Figure 11 and Figure 13.
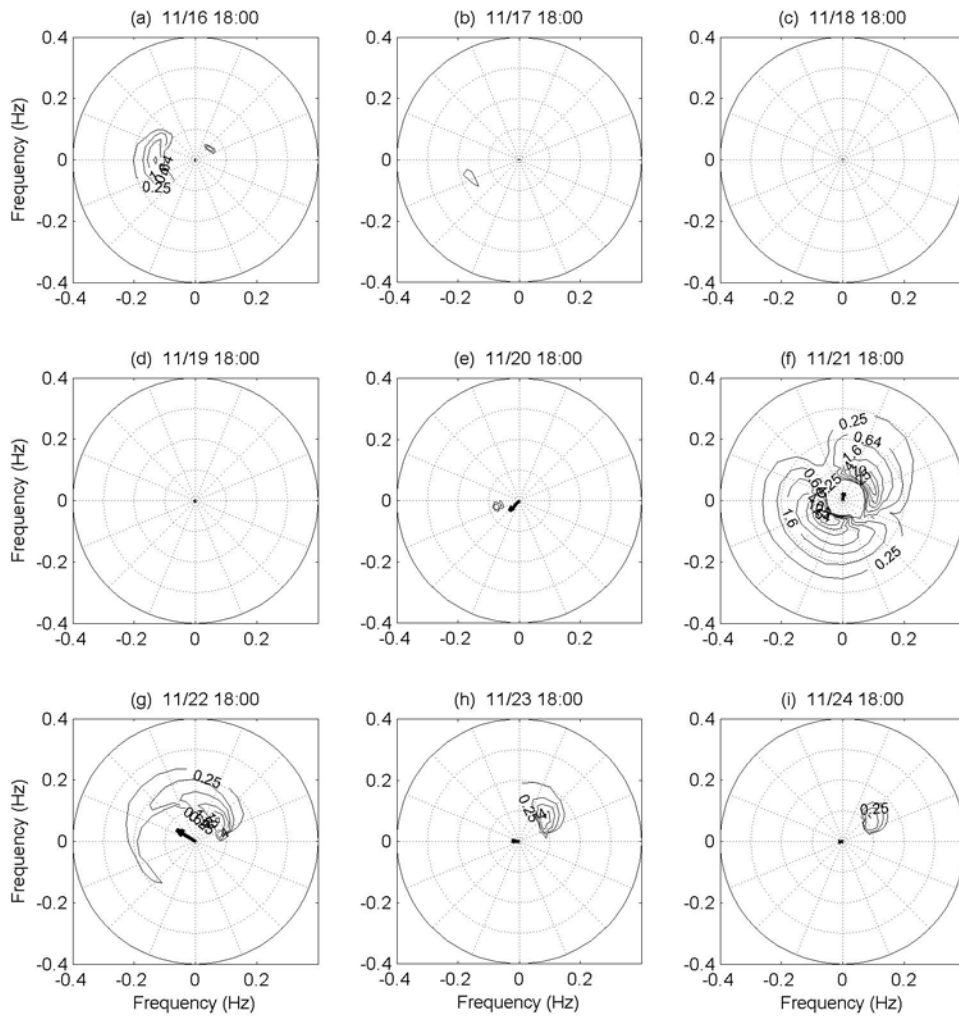
Figure 42   Similar format as Figure 32 on the same location ($11.6°N$ and $114.4°E$) with ideal typhoon winds. The time step is 24 hours from 1800UTC 16 November to 1800UTC 24 November.
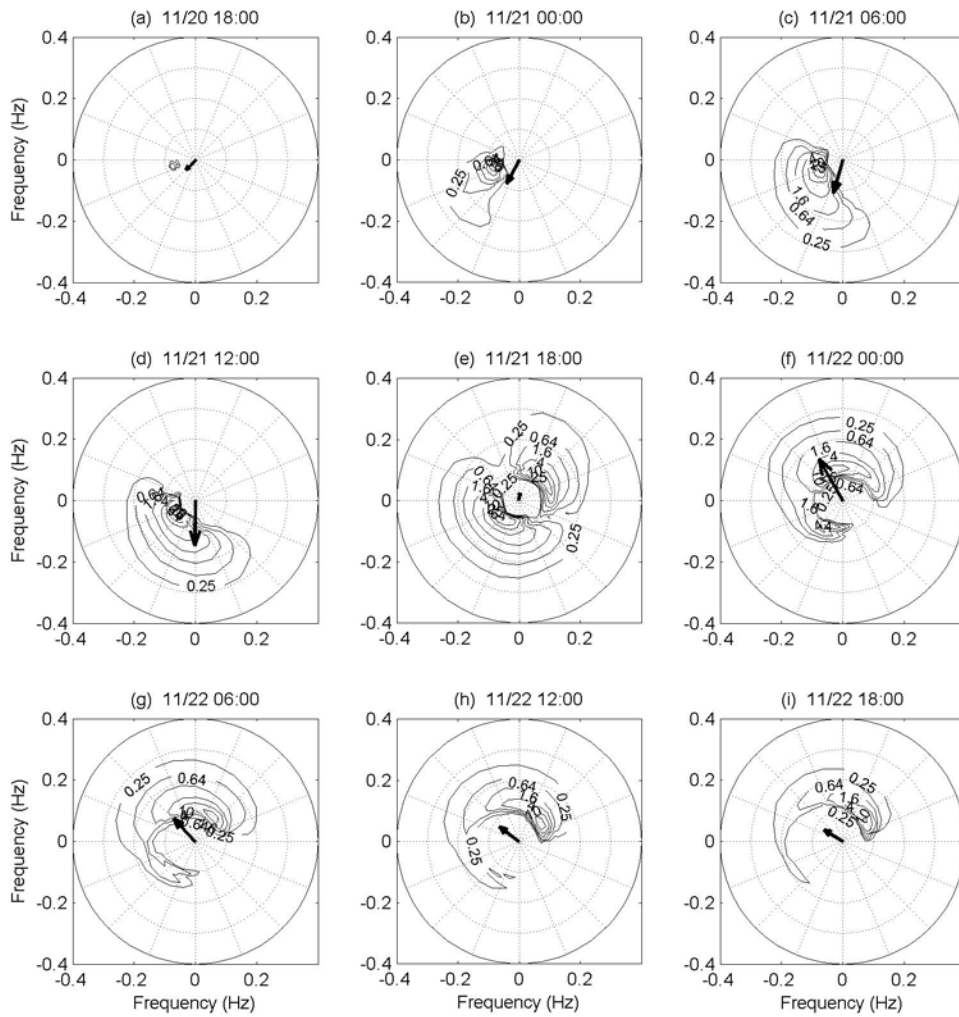
Figure 43   Detail evolution of Figure 42 with time step 6 hours from 1800UTC 20 November to 1800UTC 21 November.

Figure 44 H_s, and central (C) and four-way (F, R, L, and B) directional wave spectra from ideal typhoon winds of Center-IV (0600UTC 24 November, $8.8°N$ and $108.8°E$). Similar format as Figure 35.
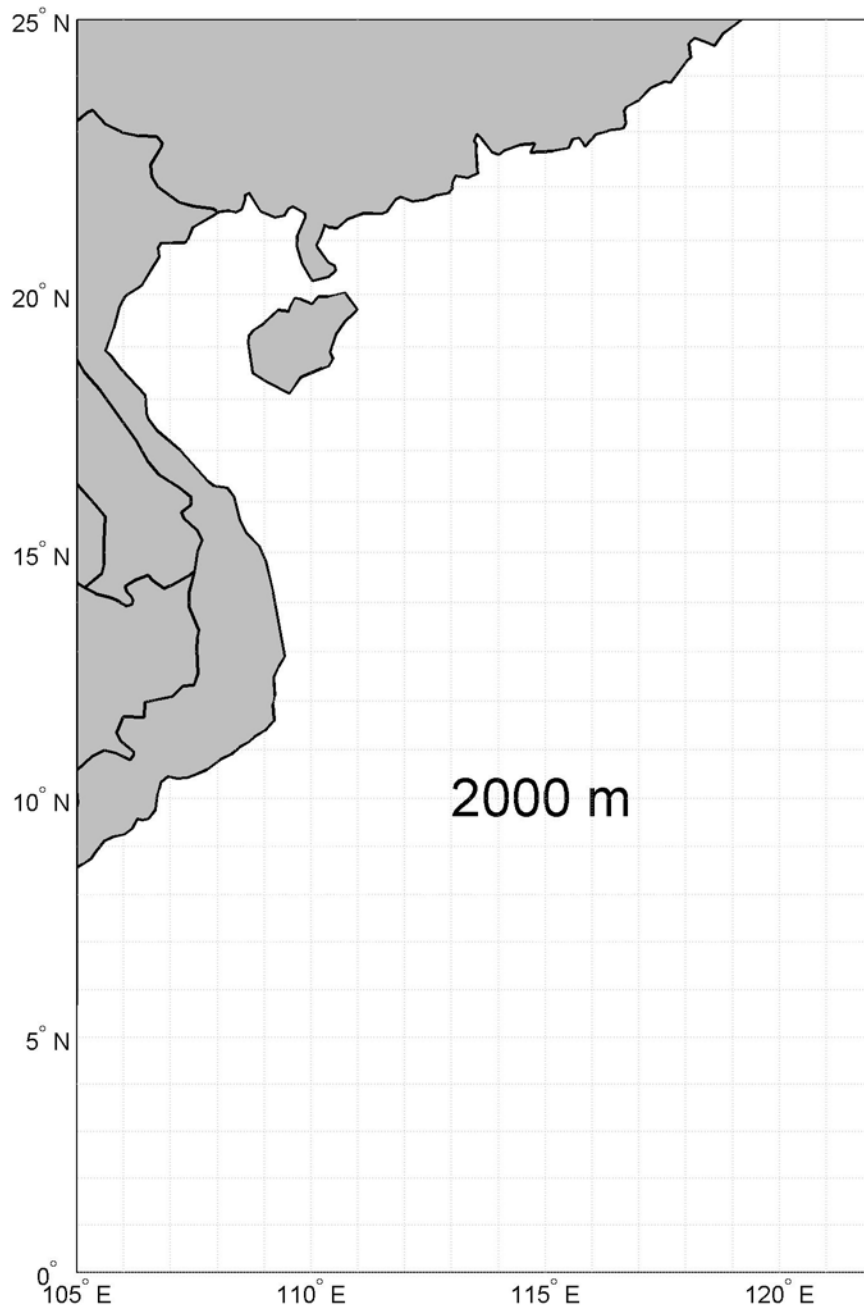
Figure 45   The uniform depth 2000 m of the SCS. The surrounding islands are removed,
only the Asian landmass is reserved.
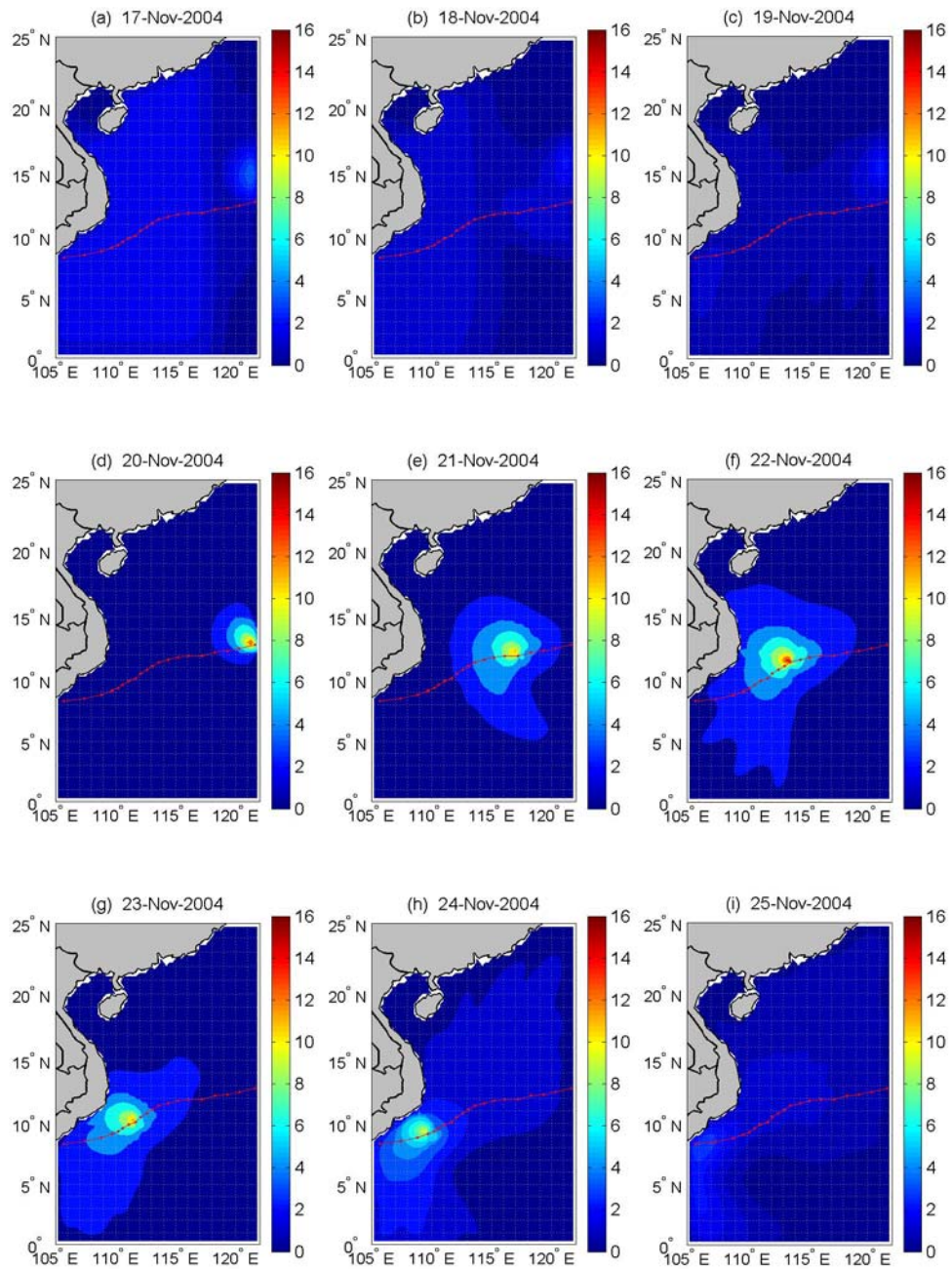
Figure 46   Daily evolution of H_s from ideal typhoon winds with uniform depth in the SCS during the period of TY Muifa (2004).

(a)   **(b)**
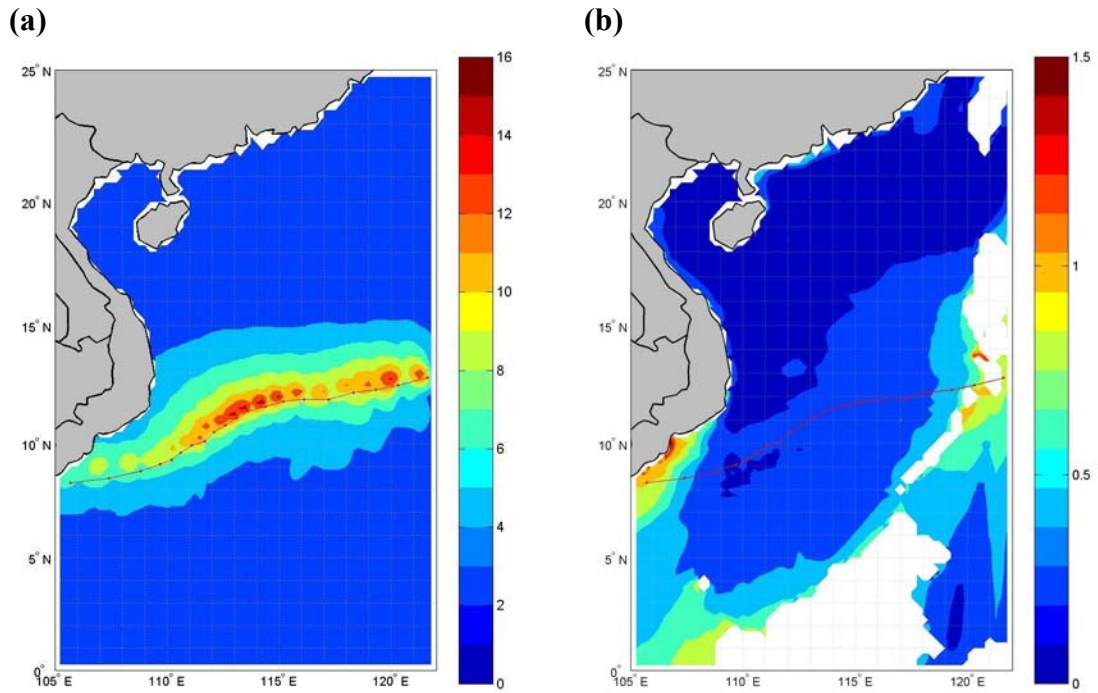
Figure 47   (a) The total distribution of the maximum H_s from ideal typhoon winds with
uniform water depth. Similar format as Figure 40a. (b) The mean difference of
H_s between Figure 39 and Figure 46. Similar format as Figure 41a.
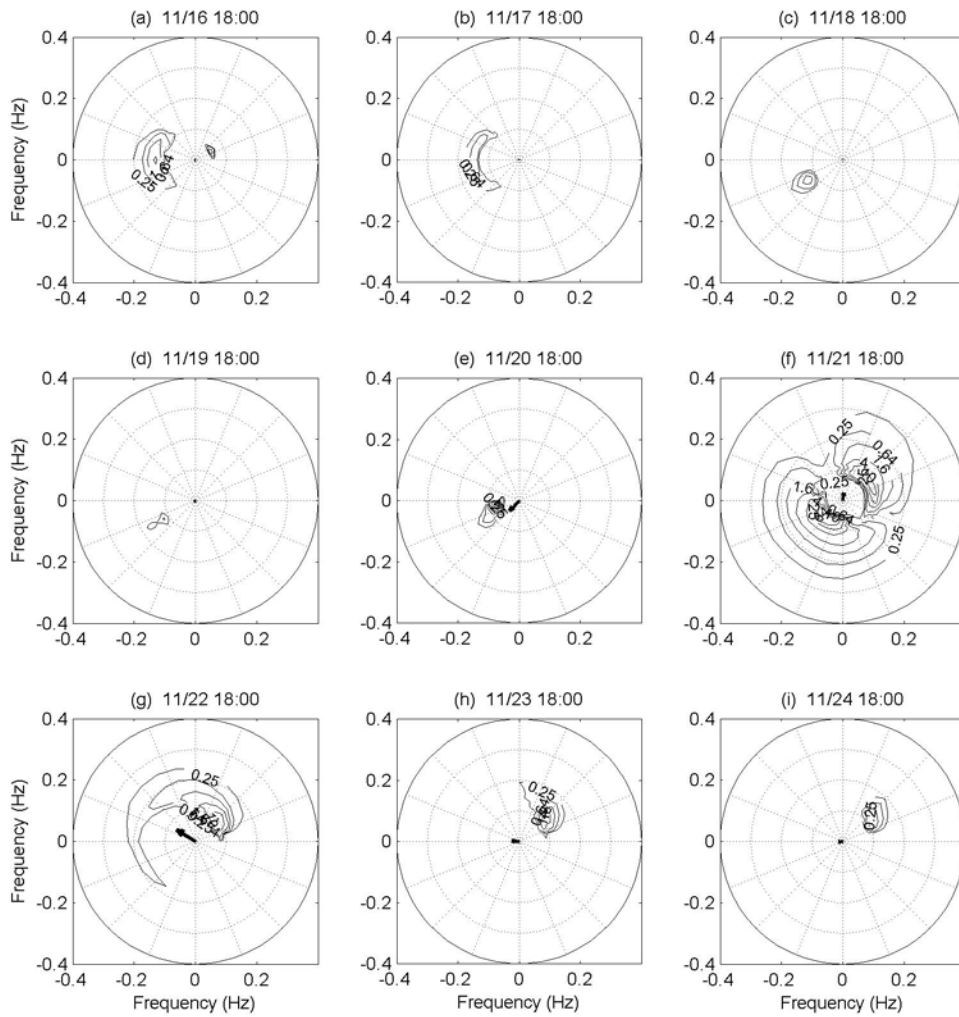
Figure 48   Similar format as Figure 32 on the same location ($11.6°N$ and $114.4°E$) with ideal typhoon winds and uniform water depth. The time step is 24 hours from 1800UTC 16 November to 1800UTC 24 November.
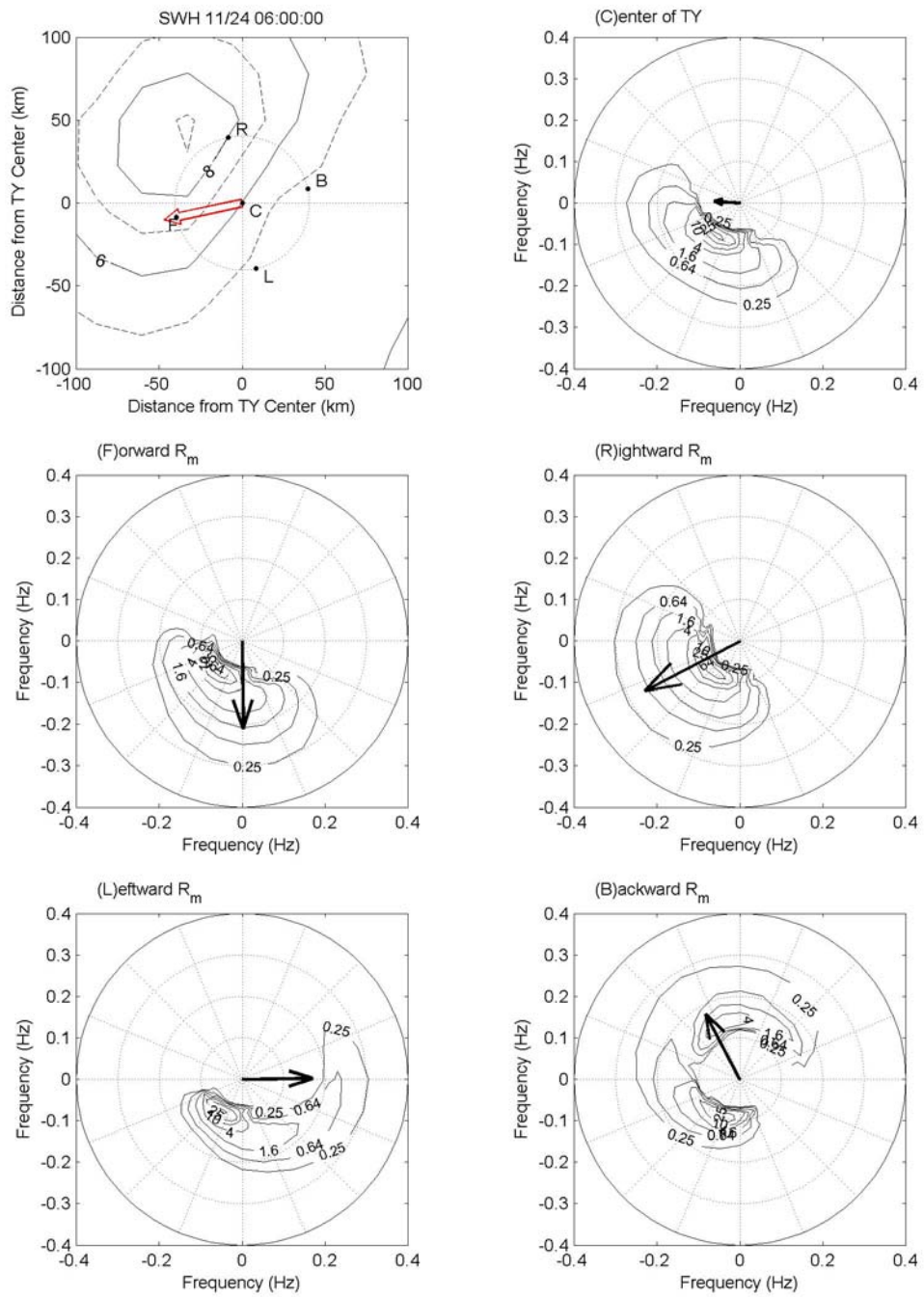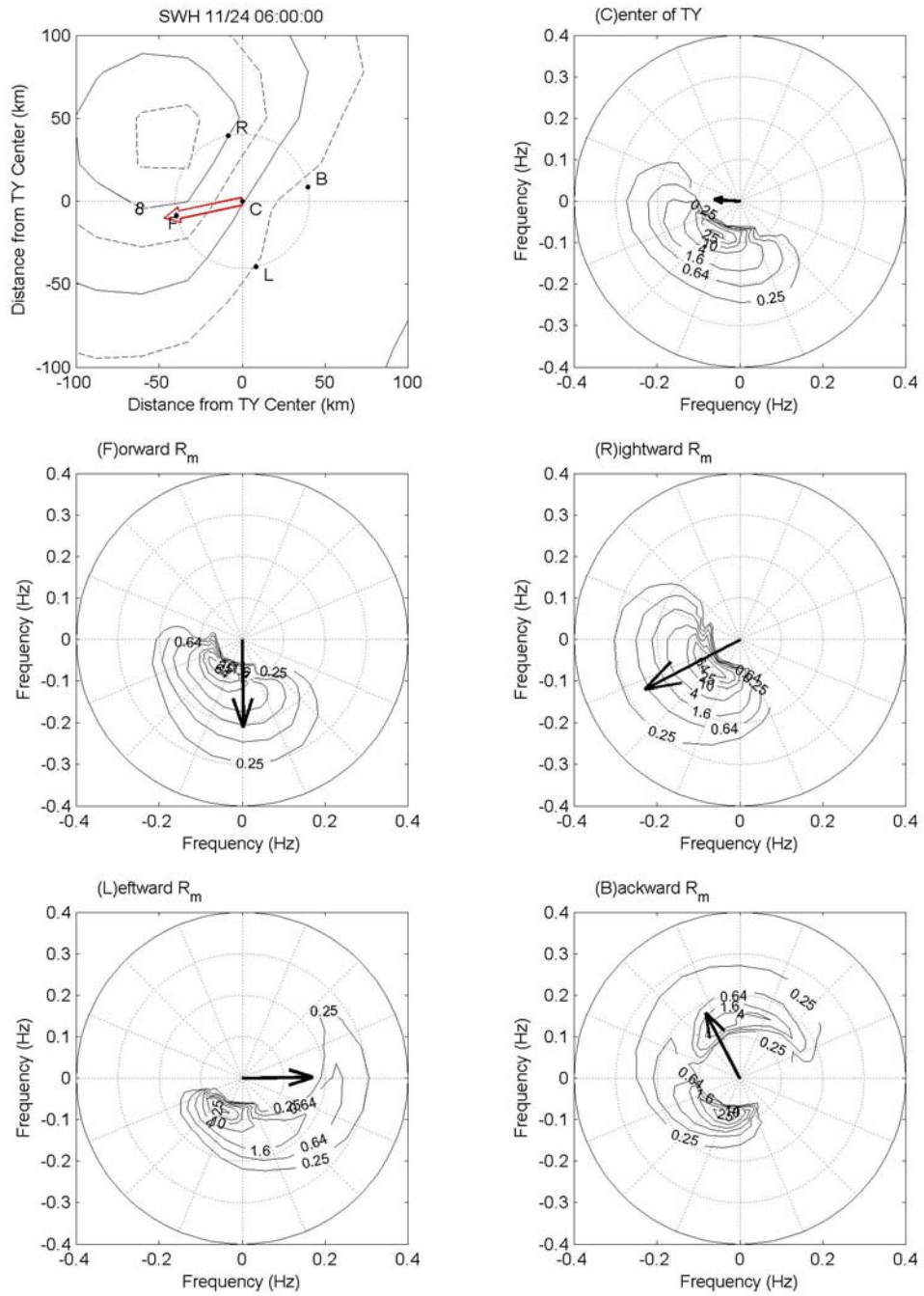
Figure 49 H_s, and central (C) and four-way (F, R, L, and B) directional wave spectra of Center-IV (0600UTC 24 November, $8.8°N$ and $108.8°E$) from ideal typhoon winds with uniform water depth. Similar format as Figure 35.

86

Switch Parameters	Characteristics
DUM	Dummy to be used if WW3 is to be installed on previously untried hardware
LRB8	8 byte words
SHRD	Shared memory model, no message passing
SEED	Seeding of high-frequency energy
GRD1	Settings directly hardwired to user-defined spatial grids (spherical coordinate with $1/4°$ grids)
SP1	User-defined spectral grids.
PR2	QUICKEST ULTIMATE propagation scheme with Booij and Holthuijsen (1987) dispersion correction
ST2	Tolman and Chalikov (1996) source term package
STAB2	Enable stability correction for Tolman and Chalikov (1996) source term package
NL1	Nonlinear interaction (DIA)
BT1	JONSWAP bottom friction formulation
WIND2	Approximately quadratic interpolation
CUR2	Approximately quadratic interpolation
o1	Output of boundary points in grid preprocessor
o2	Output of the grid point status map in grid preprocessor
o2a	Generation of land-sea mask file mask.WW3 in grid preprocessor
o3	Additional output in loop over fields in field preprocessor
o4	Print plot of normalized 1-D energy spectrum in initial conditions program
o5	2-D energy spectrum
o6	Spatial distribution of wave heights (not adapted for distributed memory)
o7	Echo input data for homogeneous fields in generic shell

Table 4   The WW3 model switch parameters setting.

THIS PAGE INTENTIONALLY LEFT BLANK

VIII. CONCLUSIONS AND RECOMMENDATIONS

This thesis investigated the SCS wave characteristics using WW3 with winter typhoon forcing. The model was forced by high resolution wind field, which was obtained from the QuikSCAT observation combined with the Tropical Cyclone Wind Profile Model (TCWPM). The WW3 model was evaluated using the TOPEX/Poseidon altimetry observation during the period of Typhoon Muifa (2004).

The effects of typhoon and monsoon on the wave characteristics were analyzed with three scenarios using: (1) realistic winds and bottom topography, (2) ideal typhoon winds and realistic bottom topography, and (3) ideal typhoon winds and uniform bottom topography. The typhoon effect was simulated using the ideal typhoon wind (Scenario-2). The monsoon effect was simulated using the difference between Scenario-1 and Scenario-2. Use of the uniform bottom topography represented the open ocean case. The topographic effect was examined by the difference between Scenario-2 and Scnario-3.

Along the typhoon translation track, the core of the maximum significant wave height (H_s) was asymmetric with higher H_s and wider core in the right side than the left side. The maximum H_s was about 16 m located at minimum typhoon lowest pressure center. At a single position, the maximum H_s was always in the right-front quadrant of the typhoon center and located slightly outside the maximum wind radius (R_m). Before typhoon arrival, the monsoon-generated swell dominated and maximum significant wave height was about 4 m; after typhoon departure, the monsoon swell remained dominant and the typhoon-introduced waves decayed gradually and lasted for three days.

The waves were generated in both frontward and backward directions for higher typhoon intensity, but only in the frontward direction for lower typhoon intensity. When the typhoon intensity was reduced (from Center-II to Center-IV), the directional wave spectra were very different at the frontward, rightward, and leftward locations. Two wave packets were generated in both upwind and downwind directions for high typhoon intensity, but only one wave packet was generated in downwind direction for low typhoon intensity. However, the directional wave spectra were less different at the

89

backward location. For the typhoon-generated waves in the SCS, the factors affecting the SCS wave characteristics with their importance from large to small are listed as follows: typhoon intensity, distance and direction from typhoon center, the typhoon translation speed, monsoon, and topography.

The typhoon intensity had a greater effect on the SCS waves than the typhoon translation speed. As the typhoon passed by, wind speed and direction changed rapidly. Stronger intensity with slower translation speed usually generated a pair of wave packets. On the contrary, typhoon forcing had greater effect on the SCS waves than monsoon forcing. Low-frequency swell was generated by monsoon forcing. When the typhoon was present, the typhoon-introduced waves dominated and were much greater than monsoon-generated swell.

In wave propagation, the typhoon-generated wave transformed across the SCS to farther than 1000 km but only in the forward, the left-frontward, and the right-rearward directions of the typhoon center. The wave energy did not propagate to the left-rearward direction of the typhoon center. Along the wave propagation direction, the obstructions of coastline and small islands generated the wave shadow zones. This feature implies that the SCS, a semi-close marginal sea, can be considered as an independent wave system from nearby oceans except the energy transform through the Luzon Strait, which is deep to 1800 m. The Sulu Sea, which separated by the Palawan Island, can be seen as a different wave system from the SCS.

The bathymetric effect was important only for water depth shallower than 100 m. For depth deeper than 100 m, the bathymetry may have an effect on H_s, but almost no effect on the wave propagation direction and decay frequency.

The field observation in tropical cyclones of Powell et al. (2003) reports that the drag coefficient (C_d) is much less than previously thought in extreme high wind speed, i.e., above 40 m/s. At high wind speed, the overestimate of the drag coefficient (C_d) in WW3 has also been reported (Moon et al. 2004a). One possible improvement is to use a new scheme to compute the drag coefficient. Furthermore, this high wind speed

overestimate may be examined by comparing wave simulation with field wave observation, if detail wave measurements (e.g., motion buoys) are available during the typhoon passage in the future.

THIS PAGE INTENTIONALLY LEFT BLANK

LIST OF REFERENCES

Allender, J. H., J. Albrecht, and G. Hamilton, 1983: Observations of directional relaxation of wind sea spectra. *J. Phys. Oceanogr., 13*, 1519-1525.

Barber, N. F., and F. Ursell, 1948: The generation and propagation of ocean waves and swell. I. Wave periods and velocities. *Philosophical Transactions of the Royal Society of London. Series A. Mathematical and Physical Sciences, 240*, 527-560.

Bouws, E., and G. J. Komen, 1983: On the balance between growth and dissipation in an extreme depth-limited wind-sea in the southern North Sea. *J. Phys. Oceanogr., 13*, 1653-1658.

Carr, L. E., III, and R. L. Elsberry, 1997: Models of tropical cyclone wind distribution and beta-effect propagation for application to tropical cyclone track forecasting. *Mon. Weather Rev., 125*, 3190-3209.

Cheang, B., 1987: Short- and long-range monsoon prediction in Southeast Asia. *Monsoons,* J. S. Fein and P. L. Stephens, Eds., Wiley, 579-606.

Chu, P. C., Y. Q. Qi, Y. C. Chen, P. Shi, and Q. W. Mao, 2004: South China Sea wind-wave characteristics. Part I: Validation of Wavewatch-III using TOPEX/Poseidon data. *J. Atmos. Ocean. Technol., 21*, 1718-1733.

____, J. M. Veneziano, C. W. Fan, M. J. Carron, and W. T. Liu, 2000: Response of the South China Sea to Tropical Cyclone Ernie 1996. *J. Geophys. Res. (C Oceans), 105*, 13991-14009.

Geernaert, G. L., 1988: Measurements of the angle between the wind vector and wind stress vector in the surface layer over the North Sea. *J. Geophys. Res. (C Oceans), 93*, 8215-8220.

Gray, W. M., 1968: Global view of the origin of tropical disturbances and storms. *Mon. Weather Rev., 96*, 669-700.

Hasselmann, D. E., M. Dunckel, and J. A. Ewing, 1980: Directional wave spectra observed during JONSWAP 1973. *J. Phys. Oceanogr., 10*, 1264-1280.

Hasselmann, K., T. P. Barnett, E. Bouws, H. Carlson, D. E. Cartwright, K. Enke, J. A. Ewing, H. Gienapp, D. E. Hasselmann, P. Kruseman, A. Meerburg, P. Mueller, D. J. Olbers, K. Richter, W. Sell, and H. Walden, 1973: Measurements of wind-wave growth and swell decay during the Joint North Sea Wave Project (JONSWAP). *Dtsch. Hydrogr. Z. Ergaenzungsh. (A.), 12*, 8-95.

Hasselmann, S., and K. Hasselmann, 1985: Computations and parameterizations of the nonlinear energy transfer in a gravity-wave spectrum. Part I: A new method for efficient computations of the exact nonlinear transfer integral. *J. Phys. Oceanogr.,* **15**, 1369-1377.

____, ____, J. H. Allender, and T. P. Barnett, 1985: Computations and parameterizations of the nonlinear energy transfer in a gravity-wave spectrum. Part II: Parameterizations of the nonlinear energy transfer for application in wave models. *J. Phys. Oceanogr.,* **15**, 1378-1391.

Holt, B., A. K. Liu, D. W. Wang, A. Gnanadesikan, and H. S. Chen, 1998: Tracking storm-generated waves in the northeast Pacific Ocean with ERS-1 synthetic aperture radar imagery and buoys. *J. Geophys. Res. (C Oceans),* **103**, 7917-7929.

Janssen, P. A. E. M., 1989: Wave-induced stress and the drag of air flow over sea waves. *J. Phys. Oceanogr.,* **19**, 745-754.

Jones, I., and Y. Toba, 2001: *Wind Stress over the Ocean.* Cambridge University Press, 307 pp.

JTWC, cited 2005: 2004 annual tropical cyclone report. [Available online at http://www.npmoc.navy.mil/jtwc/atcr/2004atcr/].

Kawai, S., K. Okada, and Y. Toba, 1977: Field data support of three-seconds power law and $gu_*\sigma^{-4}$-spectral form for growing wind waves. *J. Oceanogr.,* **33**, 137-150.

Li, C., 1994: A numerical simulation of seasonal circulation in the South China Sea. M.S. Thesis. Dept. of Oceanogr., Naval Postgraduate School, 74 pp. [AD-A283701.]

Liu, W. T., 2002: Progress in scatterometer application. *J. Oceanogr.,* **58**, 121-136.

Long, S. R., N. E. Huang, E. Mollo-Christensen, F. C. Jackson, and G. L. Geernaert, 1994: Directional wind wave development. *Geophys. Res. Lett.,* **21**, 2503-2506.

Martin, S., 2004: *An Introduction to Ocean Remote Sensing.* Cambridge, 426 pp.

Masson, D., 1990: Observations of the response of sea waves to veering winds. *J. Phys. Oceanogr.,* **20**, 1876-1885.

McGride, J. L., 1995: Tropical cyclone formation. *Global Perspectives on Tropical Cyclones,* R. L. Elsberry, Ed., World Meteorological Organization, 63-105.

Moon, I., I. Ginis, T. Hara, H. L. Tolman, C. W. Wright, and E. J. Walsh, 2003: Numerical simulation of sea surface directional wave spectra under hurricane wind forcing. *J. Phys. Oceanogr.,* **33**, 1680-1706, doi:10.1175/1520-0485(2003)033(1680:NSOSSD)2.0.CO;2.

____, ____, and ____, 2004a: Effect of surface waves on air-sea momentum exchange. Part II: Behavior of drag coefficient under tropical cyclones. *J. Atmos. Sci.,* **61**, 2334-2348.

____, T. Hara, and I. Ginis, 2004b: Effect of surface waves on Charnock coefficient under tropical cyclones. *Geophys. Res. Lett.,* **31**, L20302.

____, ____, ____, S. E. Belcher, and H. L. Tolman, 2004c: Effect of surface waves on air-sea momentum exchange. Part I: Effect of mature and growing seas. *J. Atmos. Sci.,* **61**, 2321-2333.

Neumann, C. J., 1993: Global overview. *Global Guide to Tropical Cyclone Forecasting,* World Meteorological Organization, Ed., World Meteorological Organization, 1-51.

Phillips, O. M., 1957: On the generation of waves by turbulent wind. *J. Fluid Mech.,* **2**, 417-445.

Powell, M. D., P. J. Vickery, and T. A. Reinhold, 2003: Reduced drag coefficient for high wind speeds in tropical cyclones. *Nature,* **422**, 279-283, doi:10.1038/nature01481.

Ramage, C. S., 1971: *Monsoon Meteorology.* International geophysics series, Vol. 15, Academic Press, 296 pp.

Schwerdt, R. W., F. P. Ho, and R. R. Watkins, 1979: Meteorological criteria for standard project hurricane and probable maximum hurricane wind fields, gulf and east coasts of the United States., NOAA Tech. Rep. NWS-23, 347pp. [PB80-117997; NOAA-TR-NWS-23; NOAA-79101101.]

Smith, S. D., 1980: Wind stress and heat flux over the ocean in gale force winds. *J. Phys. Oceanogr.,* **10**, 709-726.

Spencer, M. W., C. Wu, and D. G. Long, 1997: Tradeoffs in the design of a spaceborne scanning pencil beam scatterometer - Application to SeaWinds. *IEEE Trans. Geosci. Remote Sens.,* **35**, 115-126.

____, ____, and ____, 2000: Improved resolution backscatter measurements with the SeaWinds pencil-beam scatterometer. *IEEE Trans. Geosci. Remote Sens.,* **38**, 89-104.

Su, J., 1998: Circulation dynamics of the China Seas north of 18° N. *The Global Coastal Ocean: Multiscale Interdisciplinary Processes,* A. R. Robinson and K. H. Brink, Eds., The sea, ideas and observations on progress in the study of the seas ed. Interscience Publishers, 483-522.

Toba, Y., 1972: Local balance in the air-sea boundary processes. *J. Oceanogr.,* **28**, 109-120.

_____, K. Okada, and I. S. F. Jones, 1988: The response of wind-wave spectra to changing winds. Part I: Increasing winds. *J. Phys. Oceanogr.,* **18**, 1231-1240.

Tolman, H. L., 1999: *User Manual and System Documentation of WAVEWATCH-III version 1.18.* NOAA/NCEP Tech. Note 166, 110 pp.

_____, B. Balasubramaniyan, L. D. Burroughs, D. V. Chalikov, Y. Y. Chao, H. S. Chen, and V. M. Gerald, 2002: Development and implementation of wind-generated ocean surface wave models at NCEP. *Wea. Forecast,* **17**, 311-333.

_____, and D. Chalikov, 1996: Source terms in a third-generation wind wave model. *J. Phys. Oceanogr.,* **26**, 2497-2518.

Walsh, E. J., D. W. Hancock III, D. E. Hines, R. N. Swift, and J. F. Scott, 1989: An observation of the directional wave spectrum evolution from shoreline to fully developed. *J. Phys. Oceanogr.,* **19**, 670-690.

Waseda, T., Y. Toba, and M. P. Tulin, 2001: Adjustment of wind waves to sudden changes of wind speed. *J. Oceanogr.,* **57**, 519-533.

Wittmann, P. A., 2001: Implementation of WAVEWATCH III at Fleet Numerical Meteorology and Oceanography Center*, Oceans,* **3**, 1474-1479.

Wright, C. W., E. J. Walsh, D. Vandemark, W. B. Krabill, A. W. Garcia, S. H. Houston, M. D. Powell, P. G. Black, and F. D. Marks, 2001: Hurricane directional wave spectrum spatial variation in the open ocean. *J. Phys. Oceanogr.,* **31**, 2472-2488.

Wyatt, L. R., 1995: The effect of fetch on the directional spectrum of Celtic Sea storm waves. *J. Phys. Oceanogr.,* **25**, 1550-1559.

INITIAL DISTRIBUTION LIST

1.　　Defense Technical Information Center
　　　Ft. Belvoir, Virginia

2.　　Dudley Knox Library
　　　Naval Postgraduate School
　　　Monterey, California

3.　　Professor Peter C. Chu
　　　Department of Oceanography
　　　Naval Postgraduate School
　　　Monterey, California

4.　　Assistant Professor Timour Radko
　　　Department of Oceanography
　　　Naval Postgraduate School
　　　Monterey, California

5.　　Professor Mary L. Batteen
　　　Chairperson, Department of Oceanography
　　　Naval Postgraduate School
　　　Monterey, California

6.　　Associate Professor Donald P. Brutzman
　　　Chair, Undersea Warfare Academic Committee
　　　Naval Postgraduate School
　　　Monterey, California

7.　　Library
　　　Chinese Naval Meteorological and Oceanographic Office
　　　Kaohsiung, Taiwan (R.O.C.)

8.　　CDR Ming-Jer Huang
　　　Department of Marine Science
　　　Chinese Naval Academy
　　　Kaohsiung, Taiwan (R.O.C.)